Sensing and timekeeping using a light-trapping diamond waveguide

by

Hannah Clevenson

B.E., Cooper Union for the Advancement of Science and Art (2011)
M.S., Columbia University (2013)

Submitted to the Department of Electrical Engineering and Computer Science
in partial fulfillment of the requirements for the degree of

Doctor of Philosophy in Electrical Engineering and Computer Science

at the

MASSACHUSETTS INSTITUTE OF TECHNOLOGY

June 2017

© Massachusetts Institute of Technology 2017. All rights reserved.

Signature redacted
Author ....
Department of Electrical Engineering and Computer Science
April 20, 2017

Signature redacted
Certified by...... ....
Dirk Englund
Assistant Professor
Thesis Supervisor

Signature redacted
Accepted by ....
Leslie Kolodziejski
Chairman, Department Committee on Graduate Theses

MASSACHUSETTS INSTITUTE OF TECHNOLOGY
JUN 23 2017
LIBRARIES
ARCHIVES

MIT Libraries

77 Massachusetts Avenue
Cambridge, MA 02139
http://libraries.mit.edu/ask

DISCLAIMER NOTICE

Due to the condition of the original material, there are unavoidable flaws in this reproduction. We have made every effort possible to provide you with the best copy available.

Thank you.

The images contained in this document are of the best quality available.

Sensing and timekeeping using a light-trapping diamond waveguide

by

Hannah Clevenson

Submitted to the Department of Electrical Engineering and Computer Science
on April 20, 2017, in partial fulfillment of the
requirements for the degree of
Doctor of Philosophy in Electrical Engineering and Computer Science

Abstract

Solid-state quantum systems have emerged as promising sensing platforms. In particular, the spin properties of nitrogen vacancy (NV) color centers in diamond make them outstanding sensors of magnetic fields, electric fields, and temperature under ambient conditions. This thesis focuses on spin-based sensing using multimode diamond waveguide structures to efficiently use large ensembles of NV centers ($> 10^{10}$). Temperature-stabilized precision magnetometry, thermometry, and electrometry are discussed. In addition, the precision characterization of the NV ground state structure under a transverse magnetic field and the use of NV-diamond for spin-based clocks are reported.

Thesis Supervisor: Dirk Englund
Title: Assistant Professor

Citations to Previously Published Work

A portion of Chapters 2 and 3 has been published in the following paper:

> "Broadband magnetometry and temperature-sensing in a light-trapping diamond waveguide," H. Clevenson, M. E. Trusheim, C. Teale, T. Schroder, D. Braje, and D. Englund. Nat. Phys. **11**, 393-397 (2015).

A portion of the following paper appears in Chapter 3:

> "High-Dynamic-Range, Vector Magnetometry with Nitrogen-Vacancy Centers in Diamond," C. Teale,* H. Clevenson*, L. M. Pham*, K. Johnson, D. Englund, and D. Braje. *In preparation.*

A portion of the following paper appears in Chapter 3:

> "High-sensitivity, spin-based electrometry with an ensemble of nitrogen-vacancy centers in diamond," E. H. Chen, H. Clevenson, K. Johnson, L. M. Pham, D. Englund, P. Hemmer, and D. Braje. *To Appear in Phys. Rev. A.*

Chapter 4 has been published with minor changes as:

> "Diamond-nitrogen-vacancy electronic and nuclear-spin-state anti crossings under weak transverse magnetic fields," H. Clevenson, E. H. Chen, F. Dolde, C. Teale, D. Englund, and D. Braje. Phys. Rev. A. 94, 021401(R).

Appendix A has appeared in print as:

> "Nanophotonic Filters and Integrated Networks in Flexible 2D Polymer Photonic Crystals," X. Gan, H. Clevenson, C.-C. Tsai, L. Li, and D. Englund. Sci. Rep. **3**, 2145 (2013).
>
> "High sensitivity gas sensor based on high-Q suspended polymer photonic crystal nanocavity," H. Clevenson, P. Desjardins, X. Gan, and D. Englund. Appl. Phys. Lett. **104**, 241108 (2014).
>
> "A Polymer Photonic Crystal Nanocavity for Precision Strain Sensing," X. Gan, H. Clevenson, and D. Englund. *Under review.*

Acknowledgments

I have had the fortune to share the past six years with many talented and generous friends, colleagues, and mentors. First, my thesis committee: Dirk Englund and Terry Orlando at MIT and Danielle Braje at MIT Lincoln Laboratory. As my advisor throughout this program, Dirk's focus has been a source of inspiration, and his guidance has made me the scientist that I am today. I'm very grateful to Terry for taking the time to serve on my RQE and thesis committees and for his calm and reasonable support and advice. As my mentor at Lincoln, Danielle provided the most genuine and uplifting support, both personal and professional. It's been wonderful to watch the Quantum Sensing Lab grow and thrive.

My collaboration with MIT Lincoln Laboratory has been supported by the Integrated Quantum Initiative (IQI), which has been organized by Eric Dauler and more recently by Ben Dixon and John Chiaverini. I have enjoyed being a part of this community and have appreciated connecting with others who share the commute back and forth to campus.

I had the opportunity to spend a summer at NASA JPL working with the Quantum Sciences and Technology group and learn about clocks and stability (both frequency and temperature). My mentor at JPL and throughout my term as a NASA Space Technology Research Fellow (NSTRF), Robert Thompson, helped me shape my thesis from clocks to magnetometers and provided invaluable professional guidance. Claudia Meyer and the NSTRF team provided tireless support throughout the term of the fellowship.

Graduate school has given me an increased appreciation for strong women and strong friendships. I'm so lucky to have been able to work and study with Sara Mouradian, Niv Chandrasekaran, Catherine Lee, Jane Heyes, Linh Pham, Fabiola Hernandez, Jelena Marasevic, Gouri Dongaonkar, Olivia Lenz, Bridget O'Meara, and Nicole Lesperance.

A large portion of the work in this dissertation has been published with coauthors, to whom I owe many thanks: Carson Teale, Ed Chen, Florian Dolde, Matt Trusheim,

Tim Schröder, Linh Pham, Kerry Johnson, Pierre Desjardins, Xuetao Gan, and Ren-Jye Shiue. These are all people with whom I've spent long hours in the lab and even longer hours sending paper revisions back and forth. Many thanks to each of you for your patience and effort.

Leslie Kolodziejski has been my academic advisor at MIT and has helped me navigate the numerous administrative and logistical complexities of graduate school, along with Janet Fisher and Kathy McCoy in the graduate office. In the same vein, Janice Balzer holds the Englund group together — her tireless behind-the-scenes work keeps everything running smoothly.

I must thank the kind folks who gave me comments on my dissertation manuscript: Terry Orlando, Linh Pham, Patti Clevenson, Sara Mouradian, Eric Bersin, Erik Eisenach, Greg Steinbrecher, Chris McNally, Daniel Rich, Danielle Braje, and Dirk Englund.

My parents, David and Patti Clevenson, have supported my academic pursuits since day one. Their love and support, as well as advice and guidance through the most difficult days, has made all the difference in the world. Daniel Rich Clevenson has been my partner through the easy times and the harder ones; his patience and hard work (and his expertise in chemical process control) have been invaluable. Thanks for holding all the pieces together. Last but not least, Asher Clevenson has been the best thesis-writing helper anyone could ask for.

This thesis is dedicated to the memory of Sherman Clevenson, whose 50 year career as an engineer at NASA has been an inspiration to me since I was little, and who would have loved to have a copy of this thesis for his coffee table.

The Lincoln Laboratory portion of this work is sponsored by the Assistant Secretary of Defense for Research & Engineering under Air Force Contract #FA8721-05-C-0002 and the Office of Naval Research Section 321MS. Opinions, interpretations, conclusions and recommendations are those of the authors and are not necessarily endorsed by the United States Government.

Contents

1 Introduction **23**

1.1 Diamond nitrogen vacancy defect centers 24
  1.1.1 Description of the system 24
  1.1.2 ODMR in diamond 25
1.2 Brief overview of previous work in diamond-based magnetometry and temperature sensing 28
  1.2.1 Magnetometry 28
  1.2.2 Temperature sensing 29
1.3 Scaling to ensembles of NVs 29
  1.3.1 Motivation 29
  1.3.2 Challenges 30

2 Light-trapping diamond waveguide design **33**

2.1 Introduction 33
2.2 Device Design 34
  2.2.1 Description of the LTDW 34
  2.2.2 MATLAB and Zemax simulation 36
2.3 Theory and Relevant Calculations 39
  2.3.1 Estimation of number of NVs addressed 39
  2.3.2 Path length of a Gaussian beam in the LTDW 39
  2.3.3 Effective numerical aperture of the LTDW 41
  2.3.4 Fraction of emission from an emitter deep within a parallelepiped 41
2.4 Sample preparation 42
2.5 Device characterization 43

2.5.1 Conversion efficiency 43
2.5.2 Surface roughness of the polished diamond 44
2.5.3 Absorption-limit on path length 44
2.6 Outlook 45

3 Sensing using a LTDW 47
3.1 Introduction 47
3.2 Sensitivity measurements 49
3.2.1 Noise floor 49
3.2.2 Separation of magnetic field and temperature data 49
3.3 Experimental details 51
3.3.1 Apparatus 51
3.3.2 Advantages of using lock-in amplification 51
3.3.3 Static magnetic field alignment 52
3.4 Conclusions and Outlook 52
3.4.1 Comparison with other magnetometers 52
3.4.2 Fundamental spin projection limit 53
3.4.3 Next steps and future applications 54
3.4.4 Simultaneous measurement of Zeeman-split resonances for high-dynamic-range vector magnetometry 55
3.4.5 Electrometry 56

4 Diamond NV electronic and nuclear spin-state anti-crossings under weak transverse fields 59
4.1 Introduction 59
4.2 Energy levels of the diamond NV in the weak transverse magnetic field regime 60
4.2.1 Previous work in the transverse magnetic field regime and with level anti-crossings 60
4.2.2 Detailed Hamiltonian 61
4.2.3 Double electron spin flip anti-crossing 62

4.2.4 Electron-nuclear spin flip anti-crossing 63

4.3 Experimental apparatus 65

4.4 Experimental verification 66

4.4.1 Double electron spin flip anti-crossing 66

4.4.2 Electron-nuclear spin flip anti-crossing 66

4.5 Conclusions and outlook 68

4.5.1 Utility for sensing 68

4.5.2 Implementation with ^{15}N 69

4.5.3 Adiabatic passage protocol for nuclear spin polarization 70

4.5.4 Next steps and future applications 71

5 Toward a diamond-based frequency standard **73**

5.1 Introduction 73

5.2 Clock protocol 74

5.3 Demonstration 76

5.3.1 Single-NV clock 76

5.3.2 Small-ensemble clock 77

5.4 Pulsed protocols using a LTDW 78

5.4.1 RF Uniformity & Antenna development 78

5.4.2 Demonstration of Rabi oscillations, Hahn Echo 80

5.5 Decoupling from temperature effects 81

5.5.1 Theoretical improvement 81

5.5.2 Changing dD_{gs}/dT using transverse magnetic fields 82

5.5.3 Changing dD_{gs}/dT using strain 83

5.6 Conclusions and outlook 84

5.6.1 Feasibility of a competitive diamond-based frequency standard 84

6 Summary and outlook **87**

A Polymer Photonics **91**

A.1 Nanophotonic Filters and Integrated Networks in Flexible 2D Polymer Photonic Crystals 91

A.2 High sensitivity gas sensor based on high-Q suspended polymer photonic crystal nanocavity 92

A.2.1 Introduction 93

A.2.2 Device design 93

A.2.3 Theory 95

A.2.4 Device fabrication 97

A.2.5 Experimental setup 97

A.2.6 Discussion 98

A.3 High-Q suspended polymer nanocavities for precision force and displacement sensing 101

List of Figures

1-1 **NV structure** (a) shows the defect-free carbon-carbon (C-C) tetrahedral covalent bond structure. (b) shows the carbon-nitrogen (C-N) bond with the vacancy. An electron (shown in purple) is captured from the lattice, giving the NV a negative charge. (c) shows the NV geometry, indicating the the direction of applied magnetic field, where the axial component $B_{||} = B_z$ and the transverse component $B_\perp = \sqrt{B_x^2 + B_y^2}$. (d) outlines the relevant energy levels for performing ODMR. 25

1-2 **ODMR** (a) shows an idealized spectra of a single NV resonance with no applied magnetic field and at room temperature (T_0). The resonance linewidth (δf) and normalized fluorescence difference, sometimes referred to as "contrast", between the bright and dark states (C) are indicated. Magnetic field aligned to the NV axis causes the resonance to split (b) while a change in temperature causes a global shift (c). This behavior can be generalized to the four sub-ensembles: the splitting of each set of resonances is proportional to the projection of the applied magnetic field onto that sub-ensemble's axis. Applied transverse magnetic field (not shown) results in a global shift, similar to temperature changes. 27

2-1 **Light-trapping diamond waveguide** (a) Standard single-pass laser excitation exhibiting a short path length of interaction with NV centers as compared to the LTDW. (b) For an equivalent excitation power, the LTDW increases the path length of the excitation beam by up to several orders of magnitude. (c) The colour CCD image of the LTDW, excited by a green pump laser of 70 mW, shows bright fluorescence without any spectral filtering. (d) Simulation of the beam path in the LTDW with $a = 500$ µm input facet, 3 mm side length, 100 µm diameter Gaussian profile input incident at 11.6°, and an absorption constant of $\alpha = 0.45\ \mathrm{cm}^{-1}$. 35

2-2 **Optical properties of the LTDW** (a) Pump photon flux is plotted against detected photon flux for the LTDW (blue) and for a single pass through the long side of the device (red). Error bars are contained within the data points. (b) Maximum optical path length (unconstrained by absorption) is plotted as a function of input angle into the LTDW structure with a 150 µm input facet and standard beam divergence in blue. The excitation laser intersects the input facet 50 µm from the center, resulting in asymmetry in the plot. For comparison, the maximum optical path length achievable in a single-pass configuration through the top of the sample is also plotted in black, and through the side of the sample is plotted in red. In samples with sufficiently high NV density, the excitation beam would be absorbed before achieving the maximum path length allowed by the LTDW structure. 36

2-3 **Simulation** (a) A MATLAB simulation example of a pattern where, after 32 reflections, the beam exits the sample at an angle adequately separated from the input path to enable transmission measurements. (b) An example of a path that spatially covers the majority of the diamond sample. (c) A three-dimensional rendering of the LTDW from the Zemax simulation featuring a diverging Gaussian beam. Beam divergence is artificially exaggerated by two orders of magnitude for clarity. 37

2-4 **Surface study** Atomic force microscopy characterization of surface polishing. 44

3-1 **ODMR spectra and level structure** (a) CW electron spin resonance with external magnetic field aligned along a single ⟨111⟩ crystal axis. The inset depicts the diamond lattice, where the blue circle represents the nitrogen atom and the green circles show the four possible orientations for the vacancy in the tetrahedral crystal lattice, constituting the four sub-ensembles of NVs. (b) Lock-in output corresponding to signal in (a). The scale factor (V/Hz) is provided by a linear fit around each of the two red points. Temperature and magnetic field shifts are measured independently by tracking both $m_s = \pm 1$. (c) Energy-level diagram of diamond NV center showing radiative (solid lines) and non-radiative (dotted lines) transitions. 48

3-2 **Sensitivity measurements** (a) Noise density of the in-phase lock-in amplifier signal at the ω_+ resonance (see inset) converted to units of magnetic field for a time constant of 100 ms; low frequency noise is attributed to thermal effects. (b) Separation of magnetic field and temperature effects. Green and blue lines show the sum and difference of the intensity signals from lower and higher frequency resonances of the $\langle 111 \rangle$ orientation with a time constant of 10 ms, decoupling the temperature and magnetic field drifts over 100 s, respectively. A 20-s-period square wave of amplitude 190 nT is applied with external coils and is clearly visible in the blue trace. The noise on a single 10 s step (0.93 nT) extrapolates to $\sim$ 290 pT $\text{Hz}^{-1/2}$ when accounting for the 10 Hz equivalent noise bandwidth of the lock-in amplifier. The green trace shows drift attributed to environmental effects; aliasing effects have been removed (less than 200 ms). 50

3-3 **Comparison of the LTDW (dark blue overlay) with other magnetometry technologies** Particularly with regard to target applications such as geomagnetics [1] shown in green (corresponding to the right axis), the LTDW achieves improved sensitivity with respect to other diamond-based sensors, shown in blue (corresponding to the left axis), in the important low-frequency band [2]. The LTDW's performance is competitive with other magnetometer platforms [3], shown in light blue. 53

3-4 **Frequency-locking magnetometer** (a) Magnetic field step response of Zeeman splitting at different laser powers. Upper inset: ODMR spectra of a single NV resonance. Lower inset: ODMR spectra at the output of the lock-in amplifier. Dashed lines indicate the locked hyperfine transition. Note that changes in the laser power affect the contrast as well as the slope of the lock-in signal, degrading the accuracy of an open-loop measurement. In comparison, the steady-state frequency determined by the closed-loop measurement is consistent across the wide range of laser powers. (b) Dynamic range demonstration of the magnetic field produced by a free-moving permanent magnet varying projection by 4 mT during a continuous acquisition. Simultaneous measurements of the upper and lower resonance frequency of a single NV orientation class are shown in the insets. 56

3-5 **Removing fluctuations from temperature from electric field measurements** (a) Time trace of the difference (electric field) and sum (temperature) of the lock-in-amplifier channels. Noise spectral density on the sum of the two channels, which corresponds to any common-mode fluctuations and is dominated by temperature instability in the diamond. (b) Noise spectral density on the time-trace difference (sum) of the two channels, which corresponds to the NSD of the transverse electric field (temperature) fluctuations. The shot-noise limit is given by the black line ($\frac{10}{\sqrt{2}} \frac{\text{Hz}}{\sqrt{\text{Hz}}}/\langle k_\perp \rangle_{225\text{V}} = 1.01 \frac{\text{V/cm}}{\sqrt{\text{Hz}}}$). 57

4-1 **NV energy levels with applied transverse magnetic field** (a) Axial and transverse magnetic field directions with respect to NV axis. As $B_\perp$ is increased from 35 G (b) to 45 G (c), the $m_I = 0$ energy levels are separated from the $m_I = \pm 1$ energy levels, removing the degeneracy which results in an electron-nuclear spin flip anti-crossing, which is detailed in the inset of (b). Non-dressed states are indicated with colored lines and dressed states are indicated with black lines. . 61

4-2 **Anti-crossing strengths and locations** (a) Anti-crossing coupling strength with increasing $B_{\perp}$. (b) Magnitude of small axial B fields at which the centers of these anti-crossings are observed. In both plots, the double-electron spin flip anti-crossing is marked E and the electron-nuclear spin flip anti-crossing is marked N. At fields greater than $B_{\perp} \simeq 40$ G, anti-crossing E continues to increase quadratically and anti-crossing N goes to zero as the energy levels no longer overlap. . . 64

4-3 **Apparatus and NV orientations with applied magnetic field** (a) Experimental setup. (b) The four orientation sub-ensembles of NV centers are shown with an applied magnetic field. (c) An anti-crossing strength of $\sim$ 2.6 MHz is seen in sub-ensemble 1 when the perpendicular component of the B field ($B_{1,\perp}$) is equal to 30 G and the axial component of the B field ($B_{1,\|}$) is varied around zero field. Inset shows a high resolution spectra of resonance 1 and 1′. 65

4-4 **Plots of transition energies as a function of axial magnetic field under fixed transverse magnetic field** Transitions for $B_{\perp} =$ 35 G and $B_{\perp} = 45$ G are shown, which correspond to the energy levels in Fig. 4-1. Greyscale indicates normalized fluorescence. Double-electron spin flip anti-crossings of coupling strength E_g are seen at $E_p = 0, \pm A_{\|} h / g_e \mu_B \simeq \pm 0.75$ G. ESR in diamond with a natural abundance of carbon isotopes has additional resonances due to hyperfine interactions with the $\sim$ 1% (I=1/2) ^{13}C nuclear spins; these features are visible at correspondingly lower contrast in both (a) and (b). . . . 67

4-5 **Double-electron and electron-nuclear spin flip anticrossings** Detail of double-electron and electron-nuclear spin flip anti-crossings at $B_\perp = 30$ G, where greyscale represents normalized fluorescence. The RF excitation power was reduced by 10 dB to mitigate power broadening. This allows the higher-resolution features to be observed, however, it is at the expense of signal-to-noise ratio. Electron-nuclear spin flip anti-crossings of coupling strength $N_g \simeq 250$ kHz are seen centered around $N_p \simeq \pm 0.35$ G, separated in frequency by P_{gs} at 2.877 GHz and 2.872 GHz. Numerical solutions to $\mathcal{H}_{gs}$ are plotted over the data, with the diameter of the circles correspond to the probability of the transition. 68

4-6 **Simulation with ^{15}N** Comparison of ^{15}N (a) and ^{14}N (b) samples at $B_\perp = 30$ G. 70

5-1 **Characterization of single NV** (a) Raster scan of the fluorescence of the diamond sample when pumped with 532 nm green light. The NV used is noted in red. (b) $g^{(2)}$ plot for this NV, verifying that it is a single defect. (c) CW ESR plot for this defect center, indicating that the resonance frequency is at 2.87 GHz as is typical. (d) Diagram of setup used to perform measurements on this defect center. 76

5-2 **Rabi oscillations of single NV center** Signal from a single NV center is measured as RF pulses of varying duration are applied. A slight beat frequency is visible, due to a small environmental magnetic field and/or strain splitting. A $\pi/4 pulse is determined to be \sim$ 22 ns and a $\pi pulse is determined to be \sim$ 88 ns. 77

5-3 **Single-NV clock** Sinusoidal fits to the data are found to have R-squared values of 0.73 and 0.8 for $\tau = 8$ µs (blue) and $\tau = 10$ µs (red) respectively. 78

5-4 **Small-ensemble NV clock** (a) Demonstration of Rabi oscillations. (b) Demonstration of the clock protocol on a small ensemble of NV centers, with the y-axis shows normalized fluorescence and x-axis shows detuning from resonance in Hz 79

5-5 **LTDW Rabi oscillation** Rabi sequence performed on the LTDW platform shows slow, attenuated oscillation with low contrast. 80

5-6 **LTDW Hahn echo** Hahn echo sequence performed on LTDW platform is characterized by low contrast and poor SNR. Revivals are noted out to $\tau \sim 200$ μs. 81

5-7 **Change in temperature dependence with the application of transverse magnetic field** With an applied field of $\sim$ 80 G,the temperature dependence of the zero field splitting frequency is reduced by approximately 1%. This is increased to approximately 2% at $\sim$120 G and continues to fall off quadratically. 82

A-1 (a) Photograph of the cm^2-sized PMMA film with SPPC devices mounted on a flexible polyester carrier. (b,c) Optical microscope images of the SPPC devices transferred onto fiber tissue and photoresist polymer (MICROPOSIT S1811) substrate after wet undercutting. (d) Optical microscope image of the tested SPPC devices, where from top to bottom show SPPC drop-filter, bent waveguide, and band-edge filters along ΓX and ΓJ directions. (e,f) Scanning electron microscope images of the SPPC drop-filter and band-edge filter. 92

A-2 The measurement setup and a conceptual schematic of the operation of this gas sensor. As the polymer photonic crystal cavity swells, its resonance peak shifts. Various surface treatments will enhance sensitivity to particular reagents. 94

A-3 (a) Band diagram showing four distinct modes of a one-dimensional infinite periodic waveguide comprised of a unit cell with a period of a. The width of the polymer beam is w and the air hole has dimension $h_x \times h_y$. (b) The electric field intensity ($|E|^2$) of the fundamental mode in the 1D nanobeam cavity in the $z = 0$ and $y = 0$ planes. A cross section of the Gaussian intensity profile is also shown. (c) Detail of the lattice constant taper used to create a high Q cavity. 96

A-4 (a) PMMA film on spun tissue paper (10× mag.) (b) Detail of structure in PMMA film on spun tissue paper (100× mag.) (c) Test structure using two pieces of silicon to form air gap. (d) SEM micrograph of fabricated structure. 98

A-5 (a) Photoluminescence spectrum of a high-Q cavity. The resonance is at 627 nm and the quality factor is around $13,000$. (b) Resonance shifts plotted against gas concentration. The point with the highest concentration seems to show saturation behavior. (c) After the stimulant gas is removed from the system, the resonance returns to it's original position. The baseline signal decreases as time progresses as a result of bleaching of the dye in the PMMA. 99

A-6 (a) Energy field distributions of the simulated resonant modes of the designed SPPC cavity in air (top) and water (bottom) environments, respectively. (b) Scanning electron microscope image of the suspended ladder nanocavity. (c) Optical microscope image of the nanocavity-based displacement sensor. The PMMA film with ladder cavities is suspended on a mechanical carrier, which is connected to a piezo-actuated stage to stretch the flexible cavities. 101

List of Tables

5.1 Required temperature stability 84
5.2 Comparison with atom-based frequency standards 84
5.3 Factor away from ideal fractional frequency deviation 85

Chapter 1

Introduction

Because of their excellent sensitivity at room temperature, solid-state quantum sensors are attracting wide interest. In particular, the spin properties of individual nitrogen vacancy (NV) color centers in diamond [4, 5, 6] make them outstanding sensors of magnetic fields [7, 8, 9, 10, 11, 12, 13, 14, 15], electric fields [16], strain [17], and temperature [18, 19, 20] under ambient conditions. By employing an ensemble of N unentangled NVs, a factor of up to $\sqrt{N}$ improvement in sensitivity is available [14, 21].

This thesis work began as a NASA Space Technology Research Fellowship in pursuit of a diamond electron-spin clock for space navigation and communication, implementing a proposal for diamond-based timekeeping that is insensitive to magnetic field fluctuations [22]. Two obstacles were identified in the early phase of this work. For the clock stability to be competitive with modern compact atomic clocks ($\sim 10^{-11}\tau^{-1/2}$)[23], an extremely large ensemble of NVs ($> 10^{10}$) is required. Furthermore, the sensitivity of the diamond energy level transitions to temperature fluctuations presents a limitation on the stability of the diamond-based clock.

New techniques were required to efficiently excite a large NV ensemble, to collect the optical signal, and to overcome the temperature sensitivity of the clock transition. In this thesis, after a brief introduction (Chapter 1), a light-trapping diamond waveguide (LTDW) geometry is introduced (Chapter 2), whose exceptional excitation efficiency and good signal collection enables in excess of 5% conversion efficiency of pump photons into optically detected magnetic resonance (ODMR) [24] fluorescence, a three orders of magnitude improvement over previous single-pass geometries. This dramatic enhancement of ODMR signal enables precision broadband *separable* measurements of magnetic field and temperature in the low-frequency range inaccessible by dynamical decoupling techniques (Chapter 3). The LTDW device enables the description of a newfound level anti-crossing in the diamond energy level structure (Chapter 4). Preliminary work using this device for pulsed operation and progress towards a diamond-based clock is detailed in Chapter 5. This includes a discussion of the continued limitations and several methods for overcoming the always-present ambient temperature fluctuations. Finally, an outlook for the field of ensemble-based diamond sensing and timekeeping is discussed in Chapter 6.

1.1 Diamond nitrogen vacancy defect centers

1.1.1 Description of the system

Diamond is composed of a tetrahedral lattice of covalently-bonded carbon atoms (Fig. 1-1a). Defects in diamond materials, both those mined from the earth and those created in labs, have been studied for decades [25] and dozens of known defects have been characterized [26] in the context of gemology. Defect centers in diamond are often called color centers, since they can give a normally transparent, colorless material a visible hue, depending on the composition of the defect. Diamond is typically comprised of almost 99% spin-neutral ^{12}C which creates a stable environment surrounding the defects. The remaining 1% is largely ^{13}C, which acts as a dephasing mechanism or parasitic spin bath. Engineered diamond growth with isotopically pure ^{12}C can further minimize spin-bath noise in the environment surrounding the NV. The NV, which is the quantum defect of interest in this thesis, consists of a carbon atom replaced by a nitrogen atom, adjacent to a missing carbon atom (Fig. 1-1b), and can be regarded as a "trapped ion" in the crystal lattice. There are two optically active charge states: NV^0 and NV$^-$, but for the purpose of this work the term NV refers to the NV$^-$ defect. Additionally, in diamond's tetrahedral lattice, there are four possible distinguishable orientations in which NV defects can occupy, creating four sub-ensembles of defects. These four stable sub-ensembles, each 109.5^o separated from the next, enable vector measurements of applied fields (Fig. 1-1c).

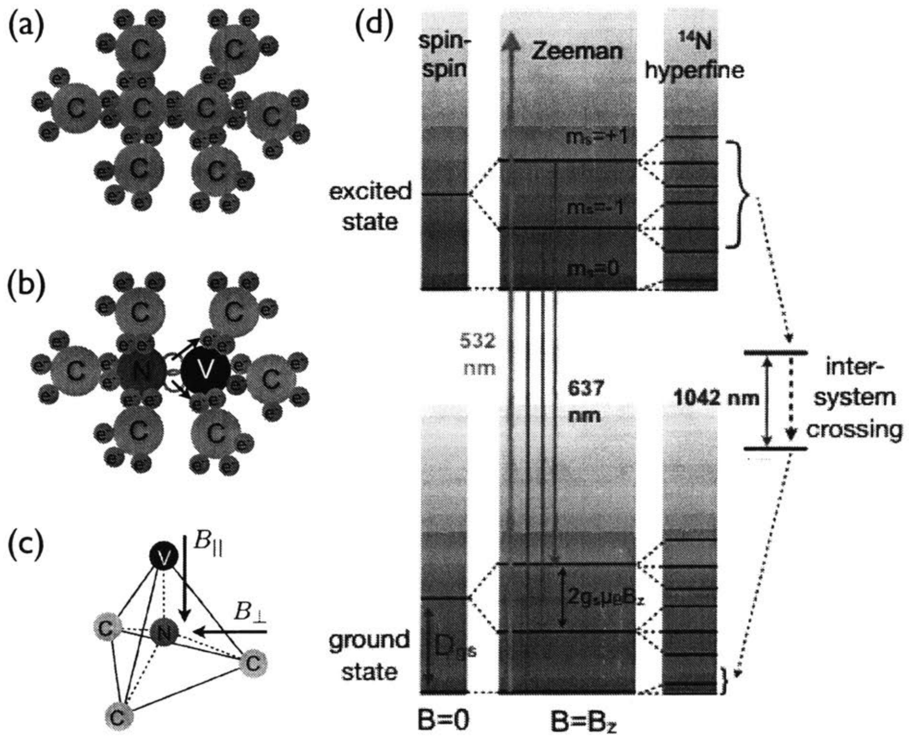
(a)
C
e⁻
(b)
N
V
(c)
V
C
N
$B_{||}$
$B_{\perp}$
(d)
spin-spin
Zeeman
¹⁴N hyperfine
$m_s=+1$
$m_s=-1$
$m_s=0$
excited state
532 nm
637 nm
1042 nm
inter-system crossing
$2g_s\mu_B B_z$
D_{gs}
ground state
B=0
B=B$_z$

Figure 1-1: **NV structure** (a) shows the defect-free carbon-carbon (C-C) tetrahedral covalent bond structure. (b) shows the carbon-nitrogen (C-N) bond with the vacancy. An electron (shown in purple) is captured from the lattice, giving the NV a negative charge. (c) shows the NV geometry, indicating the the direction of applied magnetic field, where the axial component $B_{||} = B_z$ and the transverse component $B_\perp = \sqrt{B_x^2 + B_y^2}$. (d) outlines the relevant energy levels for performing ODMR.

1.1.2 ODMR in diamond

The electronic spin state of the NV can be optically polarized using a green laser, while the energy levels are read out by monitoring the NV fluorescence while sweeping an applied RF source. Laser state preparation and optical readout are attractive properties for an optical sensor. When driven on resonance, the fluorescence level decreases. The exact frequencies of these resonances are set by the sensor's environment, and recording the shifts in these resonance frequencies maps into magnetic field and temperature experienced by the sensor.

The following Hamiltonian models the observed frequency shifts of the NV ground state triplet sub-levels (Figure 1-1d) in the zero-transverse-field, weak-axial-field, low-strain approximation with:

$$\mathcal{H}_{gs} = D_{gs}S_z^2 + g_s\mu_B B_{||}S_z + A_{||}S_z, \tag{1.1}$$

where D_{gs} is the ground state crystal field splitting, g_s is the Landé g-factor, μ_B is the Bohr magneton, $B_{||}$ is the component of the magnetic field along the NV axis (Fig. 1-1c), $A_{||}$ is the hyperfine tensor describing interactions with local nuclear spins, and S_z is the spin projection onto the NV symmetry axis with eigenvalues 0, $\pm\hbar$, corresponding to $m_s = 0, \pm 1$ [27].

At zero applied field, the triplet ground state consists of degenerate $m_s = \pm 1$ states separated from the $m_s = 0$ state by D_{gs}. Quantities such as temperature, crystal strain, and external electric fields cause shifts in D_{gs}. We assume that the intrinsic strain across the sample does not change over the course of the measurement, indicating that observed shifts in the zero field splitting (ZFS) are caused by temperature changes.

Green light (532 nm) is used to excite the NV from the ground state to the excited state, which emits broadband red fluorescence with a zero phonon line at 637 nm as it returns to the ground state. NVs in the $m_s = \pm 1$ state can follow a non-spin conserving path to a shelving state where an IR photon is emitted and the NV returns to the $m_s = 0$ state. In this way, green light can be used to polarize the NV into the higher fluorescence, $m_s = 0$ "bright" state. Microwave excitation on resonance at D_{gs} drives NVs from the $m_s = 0$ state into the $m_s = \pm 1$ state, resulting in a decrease in observed fluorescence (Fig. 1-2a). An axial magnetic field $B_{||}$, which appears in the S_z term, lifts the $m_s = \pm 1$ degeneracy, allowing the effects of magnetic fields and temperature to be separated to first order when monitoring both halves of the resonance. The difference between the two resonances is proportional to the applied axial magnetic field (Fig. 1-2b) and the global shift of the two resonances is proportional to the

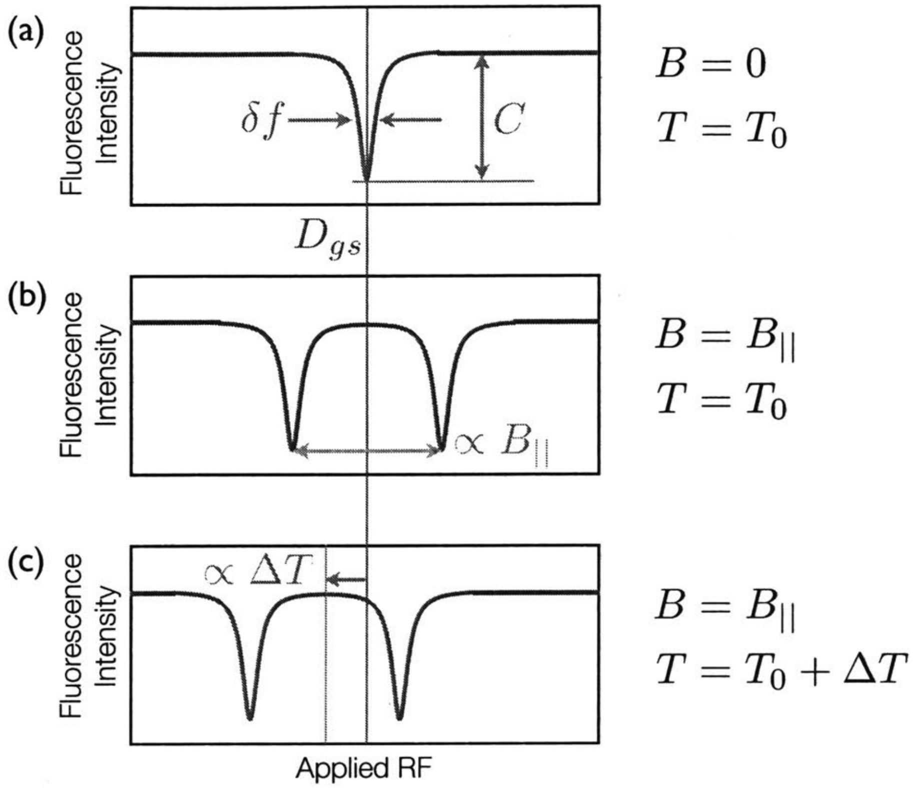
(a)
Fluorescence Intensity
δf
C
$B = 0$
$T = T_0$
D_{gs}
(b)
Fluorescence Intensity
$\propto B_{||}$
$B = B_{||}$
$T = T_0$
(c)
Fluorescence Intensity
$\propto \Delta T$
$B = B_{||}$
$T = T_0 + \Delta T$
Applied RF

Figure 1-2: **ODMR** (a) shows an idealized spectra of a single NV resonance with no applied magnetic field and at room temperature (T_0). The resonance linewidth (δf) and normalized fluorescence difference, sometimes referred to as "contrast", between the bright and dark states (C) are indicated. Magnetic field aligned to the NV axis causes the resonance to split (b) while a change in temperature causes a global shift (c). This behavior can be generalized to the four sub-ensembles: the splitting of each set of resonances is proportional to the projection of the applied magnetic field onto that sub-ensemble's axis. Applied transverse magnetic field (not shown) results in a global shift, similar to temperature changes.

change in temperature (Fig. 1-2c). This spin-dependent fluorescence measurement, along with its sensitivity to its environment, is the basis for using the diamond NV as a sensor. When the device is continuously driven, it's referred to as continuous-wave (CW) ODMR. The laser and RF excitation can also be pulsed for improved contrast (C) and decreased linewidth (δf).

1.2 Brief overview of previous work in diamond-based magnetometry and temperature sensing

1.2.1 Magnetometry

Commonly used commercial technologies like fluxgate magnetometers and giant magnetoresistance (GMR)-based systems require careful periodic calibration, due to environmental and material changes in the sensors [28, 29]. This maintenance can be impractical for remote operation. Conversely, diamond-based, as well as conventional atomic magnetometry relies on a splitting between resonances that is entirely dependent on fundamental physical quantities, which eliminates the need for calibration. Furthermore, in diamond, this splitting can be separated from the global resonance shift caused by temperature changes, making a diamond-based sensor much more reliable. A diamond-based solid-state magnetometer also has the potential to be a much more compact, robust system than similar atomic magnetometers as no vacuum system is required.

Existing diamond-based magnetometry systems can be broken into two main categories: low and high frequency operation, where the border is loosely defined by coherence time and method of operation. To date, sensitivity records in diamond-based magnetometry have been set in the high frequency regime [30], using dynamical decoupling (pulsed) techniques to get away from low frequency environmental noise. However, many magnetometry applications, such as geomagnetics [1] and medical applications [31, 2, 3], exist in the lower frequency regime. Unlike high-frequency magnetometers, which are exclusively based on pulsed operation, low-frequency magnetometers can employ CW ODMR, as described in Section 1.1.2 or pulsed laser and RF excitation measurement techniques. Pulsed operation adds complexity but has the potential to result in increased sensitivity by taking advantage of the NVs' long coherence time. However, the use of lock-in amplification to increase signal to noise in CW ODMR measurements results in competitive sensitivity as compared with pulsed operation.

Recently, defects in silicon carbide are also emerging as a promising material for solid-state magnetometry [32, 33, 34]. Results described in this thesis could potentially be extended to work in bulk SiC devices. However, currently, spin coherence times at room temperature do not yet rival those found in defects in diamond.

1.2.2 Temperature sensing

Unlike diamond-based magnetometry, which is fully based on fundamental constants, diamond-based temperature sensing relies on the phenomenological temperature dependence $\frac{dD_{gs}}{dT}$. Around room temperature, this is found to be ~ -75 kHz/K [35]. Previous work has included characterizing a polynomial describing how this quantity changes with respect to temperature [36], as well as investigations into the physical mechanism behind this shift, which is believed to be a combination of the thermal expansion of the diamond and electron-phonon interactions [37]. Pulsed protocols designed to be insensitive to magnetic fields [22] have also been used to measure temperature [18, 19, 20].

While there are applications for stand-alone temperature sensing, the main motivation for studying the temperature dependence in NVs is to remove the effects of ambient temperature changes from room-temperature, ambient-pressure NV magnetometers.

1.3 Scaling to ensembles of NVs

1.3.1 Motivation

While single-NV measurements can boast high spatial resolution, scaling up to an ensemble of NVs can offer higher sensitivity and full vector magnetic field reconstruction. The sensitivity of a measurement of a CW ODMR line shift, in an NV magnetometer limited by shot noise, is limited by a factor

$$\eta_{ODMR}^{shot} \propto \frac{\delta f}{C\sqrt{R}} \tag{1.2}$$

where δf is the resonance linewidth, C is the normalized fluorescence difference between the bright and dark states, sometimes referred to as contrast, and R is the photon collection rate. By operating at lower temperatures and using better-isolated NVs, δf can be improved by up to several orders of magnitude, at the expense of NV density. Normalized fluorescence difference, C, can be improved by roughly an order of magnitude by optimizing the driving RF and laser power applied. However, by increasing the number of NVs probed in a measurement, the R value, and subsequently the measurement sensitivity, can be increased substantially. An ensemble of 10^{10} NVs leads to a sensitivity enhancement of up to five orders of magnitude, assuming no change in contrast or linewidth. This ensemble measurement advantage, combined with the benefits of diamond-based magnetometry described in Section 1.2.1 are appealing for work towards a mass-produced, deployable sensor that could be used in remote and isolated environments without the need for periodic recalibration.

In addition, the increased sensitivity achievable through ensemble-based magnetic field sensing lends itself to many existing, mature applications, while single-NV magnetic field sensing remains limited to the lab setting. In particular, geoscience is an application space where ensemble-based sensing shows great potential. Others include biomagnetism, bioassays, condensed matter physics, material science, biothermometry, bulk magnetometry for surveying, and hyper-polarized media for NMR.

1.3.2 Challenges

The challenges facing ensemble-based NV sensing can be broken into two categories: material properties and experimental design. The material properties of the diamond around each NV play a role in sensitivity. As more NVs are introduced into a diamond sample, either during the growth process or through implantation later, there is a corresponding increase in lattice damage and unwanted defects. This damage leads to a decrease in the coherence time of the NV, which is inversely proportional to δf, and as such, negatively affects the potential sensitivity. Unlike a single NV, which provides atomic-scale resolution, the resolution provided by an ensemble of NVs is limited by the longest linear dimension of the volume of diamond encompassing the ensemble. For increased resolution, the NV ensemble volume can be minimized by increasing the NV density, which comes at the expense of decreased NV quality. The devices described later in this thesis use a 3 mm x 3 mm x 0.3 mm diamond with ~ 0.1 ppm NV density. Work done in characterizing this sample will be discussed in Chapter 2.

The second challenge concerns experimental design, including spin protocols. A basic NV ODMR experimental setup requires an excitation laser and RF magnetic field input, as well as a way to collect the signal-containing fluorescence. For a single NV, a common configuration is to focus the excitation laser onto the NV with a nearby wire or antenna providing the RF excitation, uniformity of the laser and RF excitation is not a concern. However, as the volume of diamond that the NV ensemble occupies increases, uniform laser and RF excitation becomes important, as both affect the contrast of the signal, particularly when working below optical saturation [38]. For pulsed measurements, excitation uniformity becomes even more important, as the Rabi frequencies will vary due to spatially inhomogeneous applied RF magnetic field. The light-trapping diamond waveguide (LTDW) geometry that is described in Chapter 2 and used in Chapters 3, 4, and 5 is a step towards more uniform laser excitation. Similarly, imperfect uniformity in an applied bias magnetic field leads to an increase in resonance linewidth and a subsequent loss of sensitivity. Later chapters will discuss the use of Halbach arrays and Helmholtz coils to address bias field uniformity. Spin protocols can also be tailored to be less sensitive to inhomogeneities in laser and RF excitation.

Another challenge in working with NV-based sensors in general is the signal collection efficiency. Diamond's high index of refraction traps the majority of the fluorescence via total internal reflection. Collection through the same path as excitation, with the addition of a dichroic filter to separate the excitation and signal beams based on wavelength, has a notoriously low collection efficiency, often less than 1%. Work towards this goal with single and small ensembles of NVs includes efforts using solid immersion lenses [39] and fiber-coupled designs [40]. In ensemble-based systems, efforts include early work with diamond waveguides, placing detectors directly adjacent to the diamond [14] and the use of compound parabolic concentrators [30].

Chapter 2

Light-trapping diamond waveguide design

Portions of this chapter have appeared in print in the following publication:

> "Broadband magnetometry and temperature-sensing in a light-trapping diamond waveguide," H. Clevenson, M. E. Trusheim, C. Teale, T. Schroder, D. Braje, and D. Englund. Nat. Phys **11**, 393-397 (2015).

2.1 Introduction

As noted in Chapter 1, nitrogen vacancy (NV) defects in diamond have been shown to have excellent properties as single-defect sensors, and shown promise as ensemble-based sensors. In particular, recent work on NV ensemble-based magnetometers [13, 14, 15], inertial sensors [41], and clocks [22] has employed N unentangled color centers to realize a factor of up to $\sqrt{N}$ improvement in sensitivity [14, 21]. However, to achieve this potential sensitivity enhancement, new techniques are required to excite efficiently and to collect the optical signal from large NV ensembles. Here, we introduce a light-trapping diamond waveguide (LTDW) geometry whose exceptional excitation efficiency and good signal collection enables in excess of 5% conversion efficiency of pump photons into optically detected magnetic resonance (ODMR) [24] fluorescence, a three orders of magnitude improvement over previous single-pass geometries. This dramatic enhancement of ODMR signal enables precision broadband measurements of magnetic field and temperature in the low-frequency range inaccessible by dynamical decoupling techniques.

The NV's low absorption cross section [42] has thus far prevented high conversion efficiency from excitation power to NV ODMR signal in bulk diamond samples using the typical single-pass excitation geometry illustrated in Fig. 2-1a. For NV densities around 10^{15} cm^{-3} [8, 43], for which the NV spacing in the diamond lattice is sufficiently sparse to maintain long spin coherence times [9], up to meter-long path length would be necessary for significant excitation absorption (see Section 2.2.2). Efficient collection has been demonstrated from NVs in single-pass excitation geometries [13, 14], but absorption is less than 1% for a typical 300 μm thick, electron-irradiated, chemical vapor deposition grown, type IIa ($<$ 1 ppm nitrogen) diamond sample. Wide-field microscopy implemented with charge-coupled device (CCD) cameras can collect fluorescence from ensembles of up to 10^3 NV centers [44] in the focal volume of the objective, but suffers from low collection efficiency with the majority of fluorescence emission trapped within the diamond due to total internal reflection (TIR) at the diamond-air interface. External Fabry-Perot cavities could increase the optical depth [15] for green excitation, but would introduce bandwidth restrictions as well as the additional complexity of stabilized, narrow-linewidth excitation lasers.

2.2 Device Design

2.2.1 Description of the LTDW

We have designed and realized a new ensemble measurement scheme that overcomes these limitations. The LTDW consists of a rectangular diamond slab with a small angled facet at one corner for input-coupling of the pump beam, as illustrated in Fig. 2-1b. The input facet has a length a at an angle 45° relative to the square sample sides, allowing pump light to couple into the structure while being confined by TIR ($\theta > \theta_c = 24.6°$) on the other surfaces. Fig. 2-1c shows an optical image of a pump beam coupled at an 11.6° angle into the LTDW (3 mm x 3 mm x 300 μm).

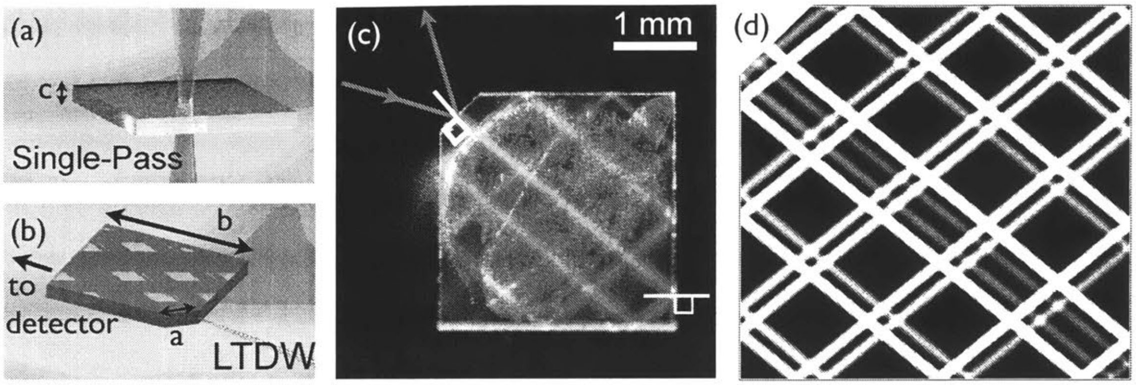

Figure 2-1: **Light-trapping diamond waveguide** (a) Standard single-pass laser excitation exhibiting a short path length of interaction with NV centers as compared to the LTDW. (b) For an equivalent excitation power, the LTDW increases the path length of the excitation beam by up to several orders of magnitude. (c) The colour CCD image of the LTDW, excited by a green pump laser of 70 mW, shows bright fluorescence without any spectral filtering. (d) Simulation of the beam path in the LTDW with $a = 500$ μm input facet, 3 mm side length, 100 μm diameter Gaussian profile input incident at 11.6°, and an absorption constant of $\alpha = 0.45$ cm^{-1}.

Red fluorescence is recorded with a colour CCD camera without spectral filtering. Figure 2-1d shows the corresponding numerical simulation of a Gaussian pump laser incident on an LTDW structure with the same dimensions. For clarity in visualizing light propagation, a non-optimal length pump path of only 6 cm is depicted.

Simulations of path length versus incident angle in Fig. 2-2b indicate that the LTDW structure enables path lengths of over a meter. These numerical simulations (see Section 2.2.2) account for beam divergence and assume losses due to absorption only. Scattering losses are neglected due to the low surface roughness of the polished sample (see Section 2.5.2).

In this ensemble sensor, the available pump power is limited by practical constraints, making efficient conversion of pump light into detected ODMR signal essential. We quantify this "pump-to-signal photon conversion" as $\eta_{ODMR} = \phi_{det}/\phi_p$, where ϕ_{det} (ϕ_p) is the photon flux detected (in the pump beam). Figure 2-2a depicts ϕ_{det} vs. ϕ_p when the LTDW input facet is pumped with a 532 nm Gaussian beam ($1/e^2$ diameter = 300 μm). Here, ϕ_p is obtained from the power of the pump beam; the linear relationship indicates that the saturation is not reached even at

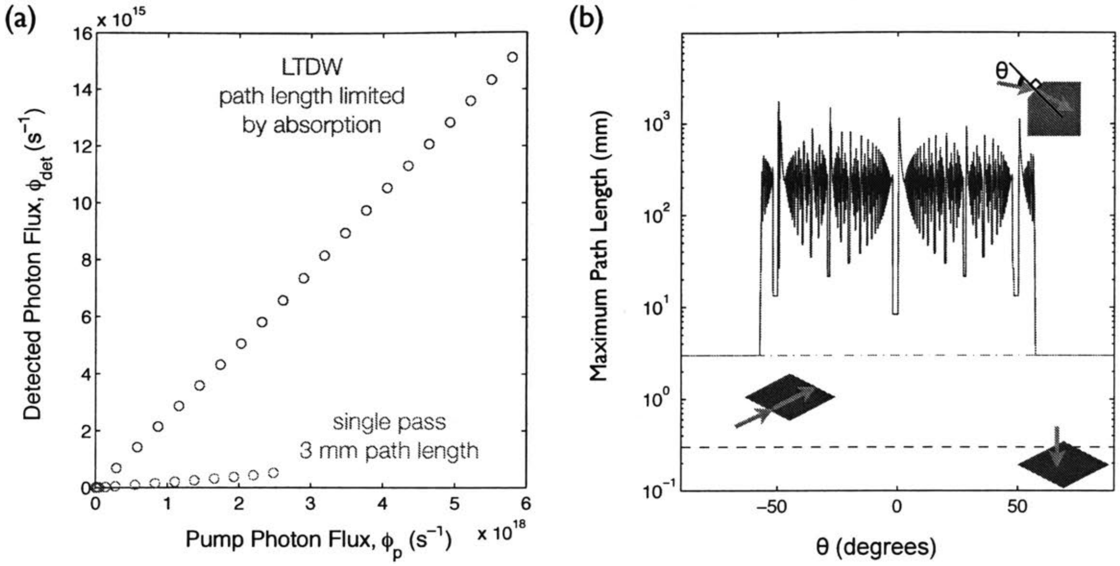

Figure 2-2: **Optical properties of the LTDW** (a) Pump photon flux is plotted against detected photon flux for the LTDW (blue) and for a single pass through the long side of the device (red). Error bars are contained within the data points. (b) Maximum optical path length (unconstrained by absorption) is plotted as a function of input angle into the LTDW structure with a 150 μm input facet and standard beam divergence in blue. The excitation laser intersects the input facet 50 μm from the center, resulting in asymmetry in the plot. For comparison, the maximum optical path length achievable in a single-pass configuration through the top of the sample is also plotted in black, and through the side of the sample is plotted in red. In samples with sufficiently high NV density, the excitation beam would be absorbed before achieving the maximum path length allowed by the LTDW structure.

relatively high pump power (~ 2W). The slope provides a conversion efficiency of $\eta_{ODMR} = 2.6 \times 10^{-3}$, *i.e.*, approximately one red photon is detected for every 385 green pump photons. This efficiency is two or three orders of magnitude greater than when the diamond is pumped in a single pass configuration along the long or short axis respectively. From our measurements, the fraction of pump photons converted into NV fluorescence (both collected and not collected) is $\eta_f \sim 0.055$ (see Section 2.5.1).

2.2.2 MATLAB and Zemax simulation

Several key factors that affect the path of the input beam in the diamond sample include the length of the input facet, the angle the beam couples into the sample, the

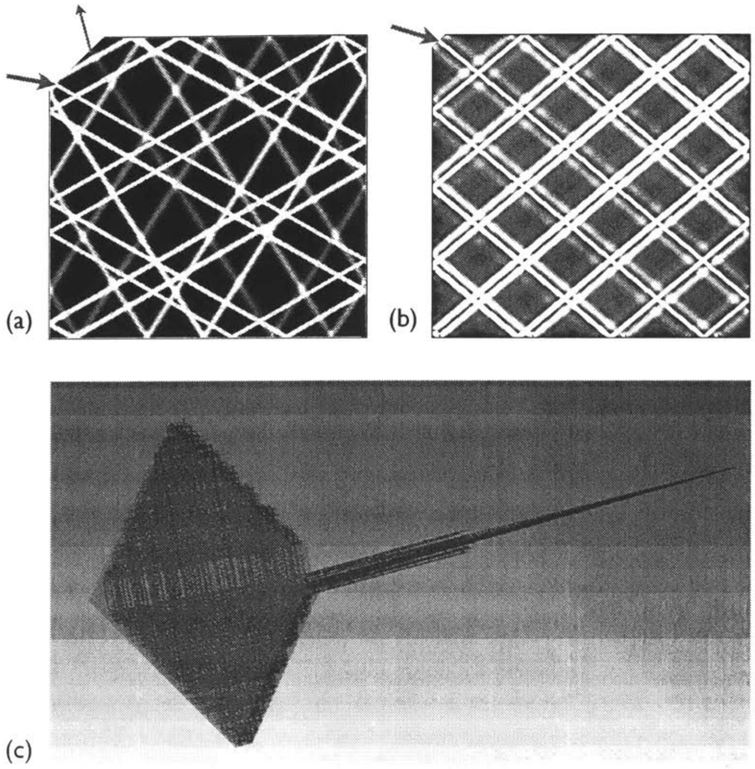

Figure 2-3: **Simulation** (a) A MATLAB simulation example of a pattern where, after 32 reflections, the beam exits the sample at an angle adequately separated from the input path to enable transmission measurements. (b) An example of a path that spatially covers the majority of the diamond sample. (c) A three-dimensional rendering of the LTDW from the Zemax simulation featuring a diverging Gaussian beam. Beam divergence is artificially exaggerated by two orders of magnitude for clarity.

placement of the beam on the input facet as it enters the sample, and the absorption constant, α, of the sample. For the purpose of simulation, we assume that polishing imperfections at the edges and corners of the sample do not result in scattering loss. Ray-tracing models are expanded to illustrate the excitation of the sample by a Gaussian beam shape in two dimensions. Zemax simulations consider paraxial Gaussian beams and assume perfect total internal reflection and losses only due to material absorption in a three-dimensional structure. For the beam diameter in our experimental setup, most beam paths are not longer than the Rayleigh range. To confirm that the beam continues to be confined even when the Rayleigh range is much shorter and to confirm that interactions with the top and bottom face of the

LTDW would not result in beam paths exiting the device, we artificially increased the beam divergence by two orders of magnitude to exaggerate the possible effect. Even at this extreme, all beam paths were confined until interacting with the input facet at an angle not meeting the TIR condition. Paths that continue after partial reflections were not considered.

The following parameters affect path length in the LTDW:

- Input Facet Length: For maximizing the absorption of the input beam, a shorter input facet provides fewer opportunities for the beam to out-couple from the structure. A longer input facet is preferable for transmission-type experiments, as it allows for more beam path configurations where the beam leaves the sample at a separate angle from which it entered – practically this allows room for a detector to be placed away from the input beam path for transmission experiments.

- Input Beam Angle: The minimum requirement for the input beam angle is that it must satisfy the TIR condition on both its first and second reflection in the sample, since the rectangular cut of the diamond preserves these angles. As seen in Figure 2-2b, incident angles that are more than $\sim 60°$ from incident do not satisfy this requirement and result in a path length of only several millimeters.

- Input Beam Placement: If the input beam diameter is smaller than the length of the input facet, placing the beam away from the center of the input facet breaks the symmetry of the system and yields a wider range of patterns.

- Rayleigh Range: The high index of diamond ($n = 2.4$) aids in the confinement of the beam, however, the dispersion of the input beam can increase the interaction of the beam with edges and corners that are more likely to have polishing imperfections, resulting in scattering losses. A more tightly focused beam can fit into a smaller input facet, but will have a shorter Rayleigh range.

- Absorption Constant: The path length at which 99% of the beam is fully absorbed by the sample can be calculated from the α value for a given wavelength for the sample.

2.3 Theory and Relevant Calculations

2.3.1 Estimation of number of NVs addressed

The LTDW sample used in the present apparatus has a volume of 2.7×10^{-3} cm^3. A pure carbon lattice of this volume with no defects corresponds to $\sim 5 \times 10^{20}$ carbon atoms (Eq. 2.1).

$$2.7 \times 10^{-3}\ \text{cm}^3 \times \frac{3.515\ \text{g}}{\text{cm}^3} \times \frac{1\ \text{mol}}{12.01\ \text{g}} \times \frac{6.02 \times 10^{23}\ \text{atoms}}{1\ \text{mol}} = 4.76 \times 10^{20}\ \text{atoms} \quad (2.1)$$

The absorption constant of the sample ($\alpha \approx 0.45$ cm^{-1}) is measured by single pass beam transmission while accounting for front and back surface reflections. Assuming a single NV absorption cross section of $\sim 2 \times 10^{-17}$ cm^2 [42], this yields an NV density upper bound of 2.3×10^{16} cm^{-3} for this sample, neglecting absorption from unpaired nitrogen atoms and other defects. From these parameters, the maximum possible NV center density is estimated at 0.1 ppm, or $\sim 10^{13}$ NV centers in each orientation. This is the maximum number of NV centers that can be addressed. Conservatively, the minimum number of NV centers addressed is estimated to be two orders of magnitude smaller, yielding more than five orders of magnitude improvement over a single NV center with the same excitation and collection efficiency parameters.

2.3.2 Path length of a Gaussian beam in the LTDW

The path length of the excitation beam in the sample is calculated geometrically via ray-tracing for rays of incident angle θ with respect to the prism facet, in the plane of the diamond waveguide. For a given incidence location on the input facet, this ray gives the maximum path length ($L_{max}(\theta)$) with respect to the input angle. We then consider a Gaussian beam as approximated by a sum of rays. In particular, we consider a Gaussian beam as a sum of rays at angles θ with weight $F_G(\theta, \theta_0, \sigma)$, where σ is the FWHM of a small (NA$\ll$ 1) Gaussian distribution of angles around θ_0. We define the mean path length of this Gaussian beam as $L_G(\theta_0)$ in the relation $P_{out,G} = P_{in,G}e^{-\alpha L_G(\theta_0)}$, where P_{in} is the incident beam power, $P_{out,G}$ is the beam power exiting the diamond after some pathlength within it, and α is the absorption constant of diamond at 532 nm for a given NV density. We assume that the beam is spatially centered at the middle of the prism facet. Solving for $L_G(\theta_0)$ gives

$$\begin{aligned} L_G(\theta_0) &= -\alpha^{-1}\ln\left(\frac{P_{out,G}}{P_{in,G}}\right) \\ &= -\alpha^{-1}\ln\left(\frac{\int F_G(\theta,\theta_0,\sigma)e^{-\alpha L_{max}(\theta)}d\theta}{\int F_G(\theta,\theta_0,\sigma)d\theta}\right) \end{aligned} \tag{2.2}$$

If the NV density is low and α is much less than $1/L_{max}(\theta)$ — i.e., the losses are dominated by scattering rather than material losses — we approximate $e^{-\alpha L_{max}(\theta)}$ as $1-\alpha L_{max}(\theta)$ and $\ln(1+\zeta)$ as ζ, so that Eqn. 2.2 becomes

$$\begin{aligned} L_G(\theta_0) &= -\alpha^{-1}\ln\left(1-\frac{\alpha\int F_G(\theta,\theta_0,\sigma)L_{max}(\theta)d\theta}{\int F_G(\theta,\theta_0,\sigma)d\theta}\right) \\ &= -\alpha^{-1}\left(\frac{-\alpha\int F_G(\theta,\theta_0,\sigma)L_{max}(\theta)d\theta}{\int F_G(\theta,\theta_0,\sigma)d\theta}\right) \\ &= \frac{\int F_G(\theta,\theta_0,\sigma)L_{max}(\theta)d\theta}{\int F_G(\theta,\theta_0,\sigma)d\theta} \end{aligned} \tag{2.3}$$

Equation 2.3 states that the path length for a Gaussian beam in the LTDW whose loss is dominated by scattering (not material losses inside the diamond) is a normalized, Gaussian-weighted average of the path lengths calculated in the ray-tracing approximation, over a spread of angles characterized by the beam divergence and the spatial entry of the beam. In other words, $L_G(\theta_0)$ approximates the longest path that a Gaussian beam of angular spread σ and central angle θ_0 propagates in the LTDW.

2.3.3 Effective numerical aperture of the LTDW

To achieve the highest number of reflections, the ideal dimension of the input facet depends on the coupling method. Since beam paths that refract into the diamond through the input facet may subsequently couple out on that facet, a smaller input facet can increase the confinement of light inside the LTDW. A larger input facet allows multiple overlapping TIR patterns to occur for entrance angles which reflect off the facet and satisfy the TIR condition ($\theta > \theta_c = 24.6°$), which can can result in more uniform excitation. If the laser is focused with a confocal parameter several times the diamond width, one can perform transmission measurements using a photodiode on the beam exiting the structure through the coupling facet. The minimum requirement for focusing the beam is that the beam divergence does not exceed the effective numerical aperture of the structure, i.e., the range of angles that satisfy the TIR condition when the laser is incident on the input facet. The effective NA of the symmetric structure used here is 0.84.

2.3.4 Fraction of emission from an emitter deep within a parallelepiped

A disadvantage to the high refractive index of diamond is that a significant fraction of the NV emission is trapped in the diamond and won't exit the LTDW. Asymmetry or intentional scattering in a light-trapping device might be used to overcome this limitation. This is also an issue for more standard confocal collection schemes. We approximate the overlapping dipole emission from the NV axes here as isotropic emission. For simplicity, we also neglect absorption in this calculation. For an emitter deep within a parallelepiped of refractive index n, there is a cone defined by the critical angle where the emission can escape each facet of the solid. For the diamond-air interface, this critical angle is: $\theta_c = 24.6°$. The ratio of the solid angle where the emission can escape (defined by the critical angle cone) to the solid angle of the facet can be described by: $\frac{2\pi(1-\cos\theta_c)}{\frac{2}{3}\pi} = 3(1-\cos(\sin^{-1}(\frac{1}{n}))) \approx 3(1-\sqrt{1-\frac{1}{n^2}}) = 0.272$. In other words, 27.2% of the emission from an emitter deep within a parallelepiped escapes the device and can be detected [45]. Taking the orientation of the NV dipole with respect to the cut diamond face into account, there may be an advantage to side-collection; we point to the supplementary material of ref. [14], which states: "The photon collection efficiency of the side-collection method is therefore expected to be in the range of $29\% < \eta_c < 91\%$ if many diffuse reflections between the edge of the diamond are allowed" and goes through the full derivation taking into account the four orientations of the NV centers.

2.4 Sample preparation

Sample preparation begins with a ⟨100⟩-oriented, type IIa CVD diamond produced by chemical vapor deposition (Element 6) with dimensions of ($3 \times 3 \times 0.3$ mm^3). To increase NV ensemble density, the diamond was electron-irradiated at 4.5 MeV with a beam current of 20 mA over ~ 0.15 m^2 and annealed for 2 hours at 850° C, yielding $\lesssim 0.1$ ppm NV centers. Characterized via absorption measurements ($\alpha \simeq 0.45$ cm^{-1}), this concentration has adequate brightness to illuminate the pattern of the pump laser in the sample and allow for almost complete absorption of the pump while being low enough to preserve spin coherence properties. This was done for ease of path determination for initial samples, but is not required in general for the LTDW platform. In fact, the LTDW is well-suited for diamond samples with a low-density of defects. At low pump and microwave power levels, the ODMR linewidth is limited by the T_2^* coherence of the diamond, which is ~ 1 µs as characterized by free-induction decay measurements. All six surfaces of the diamond are polished to a mean surface roughness of ~ 2 nm RMS (characterized via atomic force microscopy, see Section 2.5.2) with a 500 µm input facet on one corner at 45° creating an entrance window for the laser (see Fig. 2-1b). The diamond sample is thermally coupled to a brass sample holder with indium, which may cause additional absorption through evanescent coupling of the confined radiation. The thermal coupling also ensures that the device is temperature stabilized throughout the experiments, avoiding broadening in the ODMR linewidths. The sample holder is temperature-stabilized to 21.6 ± 0.1

C using a water-chiller.

2.5 Device characterization

2.5.1 Conversion efficiency

We quantify the "pump-to-signal photon conversion" as $\eta_{ODMR} = \phi_{det}/\phi_p$, where ϕ_{det} (ϕ_p) is the photon flux detected (in the pump beam). Here, ϕ_p is obtained from the power of the pump beam, accounting for the 17% intensity reflection due to the air/diamond interface. The slope from figure 2-2a provides the conversion efficiency $\eta_{ODMR} = 2.6 \times 10^{-3}$, i.e., approximately one red photon is detected for every 385 pump photons. This efficiency is two (three) orders of magnitude greater than when the diamond is pumped in a single pass configuration along the long (short) axis. We can also deduce from our measurements the fraction of pump photons converted into NV fluorescence, i.e., $\eta_f = \phi_f/\phi_p$, where the total emitted photon flux ϕ_f is obtained from the fluorescence detection efficiency η_{det} as $\phi_f = \phi_{det}/\eta_{det}$. We estimate $\eta_{det} \sim 0.048$ from the fraction of photons emitted into angles that are not confined by TIR (27.2% of total fluorescence) and the fraction of these photons that are imaged onto the detector ($\sim$ 17%). This provides $\eta_f \sim 0.055$. In principle, one may expect η_f as high as the NV internal quantum efficiency, which has been approximated to be near 0.7 [46] for NVs in bulk diamond due to the charge state transfer to NV^0. Because we were not able to accurately measure the green pump scattered out of the diamond, it was not possible to independently estimate the NV quantum efficiency in this experiment. However, by improving diamond polishing to reduce scattering loss, the pump beam confinement could be improved to increase η_f further. The detection efficiency could also be increased by a factor of 2.5 by directly positioning detectors on the four diamond facets, as was done in Ref. [14].

2.5.2 Surface roughness of the polished diamond

The surface roughness of the polished diamond was characterized using a Digital Instruments NanoScope atomic force microscope (AFM). Figure 2-4 shows a 3×3 μm square, representative of the surface features present across the sample. The mean surface roughness was found to be 0.78 nm and the rms surface roughness was found to be 2.01 nm. This surface roughness is skewed by sparse pits in the surface, which could be ameliorated with improved polishing techniques.

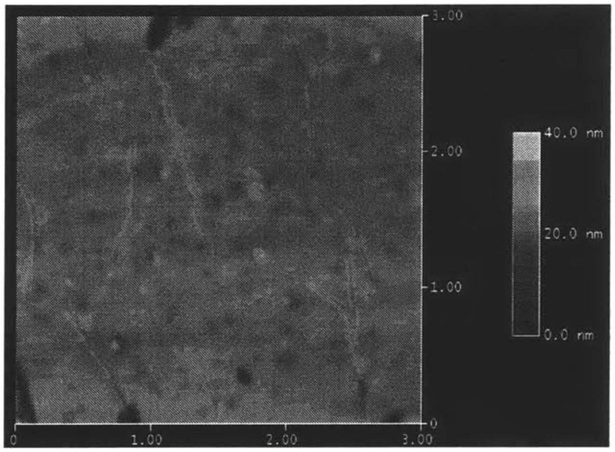

Figure 2-4: **Surface study** Atomic force microscopy characterization of surface polishing.

2.5.3 Absorption-limit on path length

In the case of the diamond shown in Fig. 2-1, the path length is largely limited by the absorption of the beam. Using a carefully aligned single-pass beam, we calculate the absorption constant of this sample to be $\alpha = 0.45$ cm^{-1}. With increased NV density we would expect this to increase, limiting the utility of the LTDW geometry for high defect density samples. Optimized magnetometry will balance coherence and NV density with improved diamond samples, and as such will likely not require the LTDW platform.

2.6 Outlook

To improve on the LTDW design presented here, TIR geometries utilizing quasi-chaotic excitation paths could also be used for NV excitation and may result in more uniform coverage of the bulk sample [47]. While the facets of the LTDW are highly polished to a surface roughness of ~ 2 nm root-mean-square (RMS) (see Section 2.5.2), scattering loss occurs at the edges and corners of the structure. Lower surface roughness would improve the TIR and reduce scattering losses. Additionally, increasing ODMR contrast also would result in improved sensitivity. Another promising geometry is the whispering gallery mode resonator, which has previously been demonstrated in diamond at IR frequencies [48].

Chapter 3

Sensing using a LTDW

Portions of this chapter have appeared in print in the following publications:

> "Broadband magnetometry and temperature-sensing in a light-trapping diamond waveguide," H. Clevenson, M. E. Trusheim, C. Teale, T. Schroder, D. Braje, and D. Englund. Nat. Phys **11**, 393-397 (2015).
>
> "High-Dynamic-Range, Vector Magnetometry with Nitrogen-Vacancy Centers in Diamond," C. Teale,* H. Clevenson*, L. M. Pham*, K. Johnson, D. Englund, and D. Braje. *In preparation.*
>
> "High-sensitivity, spin-based electrometry with an ensemble of nitrogen-vacancy centers in diamond," E. H. Chen, H. Clevenson, K. Johnson, L. M. Pham, D. Englund, P. Hemmer, and D. Braje. *To Appear in Phys. Rev. A.*

3.1 Introduction

The light-trapping diamond waveguide's increased optical path length and the consequently large ODMR signal photon flux allows for high precision measurements of quantities that affect the NV's magnetic sub-levels. Figure 3-1a plots ODMR spectra obtained under continuous-wave (CW) microwave field excitation when a 3 mm diameter loop of 200 μm-diameter wire is placed 5 mm above the LTDW. An additional 2.5 mT static magnetic field applied along the $\langle 111 \rangle$ diamond crystal axis splits the degeneracy of the NV sub-level transitions $m_s = 0 \rightarrow \pm 1$. Of the four NV orientations supported in the diamond lattice, the $\langle 111 \rangle$ sub-ensemble shows the greatest

Zeeman shift, as seen in the splitting between frequencies ω_+ and ω_- (Fig. 3-1a), as its quantization axis is aligned with the magnetic field. The equal magnetic field projection onto each of the three remaining NV orientations results in their degenerate transition energies with three times the ODMR contrast compared to the $\langle 111 \rangle$ sub-ensemble. Hyperfine coupling of the NVs to the ^{14}N nuclear spin splits each of the electronic sub-level transitions into Lorentzian triplets (Fig. 3c), which exhibit a full-width at half-maximum linewidth of 1.2 MHz spaced by ~ 2.1 MHz.

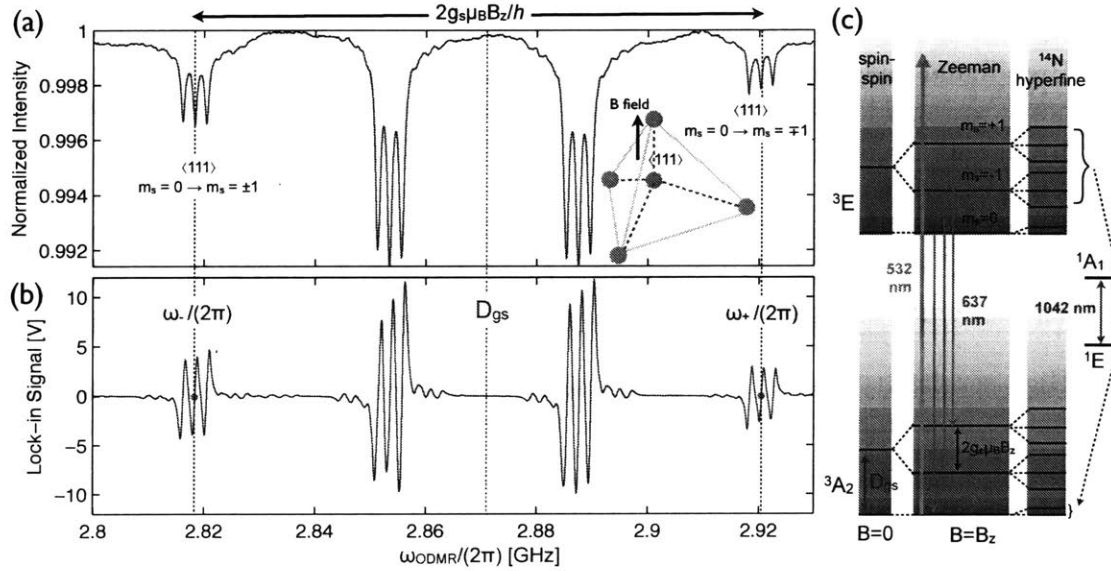

Figure 3-1: **ODMR spectra and level structure** (a) CW electron spin resonance with external magnetic field aligned along a single $\langle 111 \rangle$ crystal axis. The inset depicts the diamond lattice, where the blue circle represents the nitrogen atom and the green circles show the four possible orientations for the vacancy in the tetrahedral crystal lattice, constituting the four sub-ensembles of NVs. (b) Lock-in output corresponding to signal in (a). The scale factor (V/Hz) is provided by a linear fit around each of the two red points. Temperature and magnetic field shifts are measured independently by tracking both $m_s = \pm 1$. (c) Energy-level diagram of diamond NV center showing radiative (solid lines) and non-radiative (dotted lines) transitions.

3.2 Sensitivity measurements

3.2.1 Noise floor

Frequency analysis of the noise in the LTDW system (Fig. 3-2a) indicates that at 1 Hz, the lower frequency resonance of the $\langle 111 \rangle$ orientation sub-ensemble resonance is sensitive to less than $\sim$ 1 nT/$\sqrt{\text{Hz}}$ (Fig. 3-2a). However, as both halves of the resonance are not being monitored and thermal noise can't be separated, the bulk of the noise in this measurement can be attributed to thermal fluctuations in the environment. With careful attention to electronic noise, the next most prominent noise contribution to be electronic noise is environmental magnetic field noise and geomagnetics in an unshielded laboratory environment.

3.2.2 Separation of magnetic field and temperature data

We measure magnetic field and temperature shifts by monitoring the fluorescence signal of the LTDW at the $m_s = 0 \rightarrow -1$ and the $m_s = 0 \rightarrow +1$ transitions. The microwave excitation frequency, ω_{ODMR}, is alternately tuned to the frequencies ω_+ and ω_-, where the derivative of the ODMR signal with respect to frequency crosses zero. Around these frequencies, we modulate ω_{ODMR} at 1.5 kHz with a modulation depth of 1 MHz and use a lock-in amplifier to monitor the NV fluorescence. Figure 3-1b depicts the lock-in signal for a time constant of 10 ms.

From the ground-state, axial, hyperfine Hamiltonian (see section 1.1.2), it follows that the $m_s = 0 \rightarrow \pm 1$ resonance frequencies are given by $\omega_{\pm} \approx (D_{gs} + \beta_T \Delta T) \pm \gamma B_z$, where $\beta_T \approx -74$ kHz/K is the phenomenological temperature dependence of the NV center's zero field splitting (ZFS) at room temperature [35] and the Zeeman shift in response to an axially applied magnetic field in the $\langle 111 \rangle$ crystal direction is $\gamma = \mu_B g_s / h \approx 28$ GHz/T, where $\mu_B = (e\hbar)/(2m_e)$ is the Bohr magneton, and $g_s \approx 2$ is the Landé g-factor. By sequentially monitoring both transitions, $\omega_{\pm}$, we obtain the mean value of $\omega_{\pm}$, which yields the temperature shift ΔT, and the difference, $\omega_+ - \omega_-$, which provides the magnetic field shift [49].

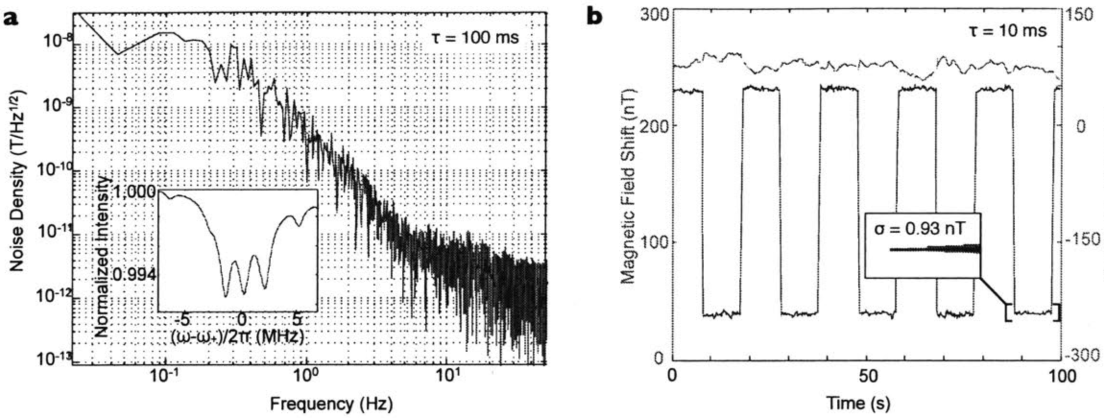

Figure 3-2: **Sensitivity measurements** (a) Noise density of the in-phase lock-in amplifier signal at the ω_+ resonance (see inset) converted to units of magnetic field for a time constant of 100 ms; low frequency noise is attributed to thermal effects. (b) Separation of magnetic field and temperature effects. Green and blue lines show the sum and difference of the intensity signals from lower and higher frequency resonances of the $\langle 111 \rangle$ orientation with a time constant of 10 ms, decoupling the temperature and magnetic field drifts over 100 s, respectively. A 20-s-period square wave of amplitude 190 nT is applied with external coils and is clearly visible in the blue trace. The noise on a single 10 s step (0.93 nT) extrapolates to ~ 290 pT Hz$^{-1/2}$ when accounting for the 10 Hz equivalent noise bandwidth of the lock-in amplifier. The green trace shows drift attributed to environmental effects; aliasing effects have been removed (less than 200 ms).

Figure 3-2b plots independent measurements of temperature and magnetic field over a time period of 100 seconds. Each point represents an integration time of 10 ms. We resolve sub-nT-level noise on a 190 nT magnetic field applied as a 0.05 Hz square-wave and expect a decrease in noise for integration times of one second. The noise on a single 10 s step (0.93 nT) extrapolates to ~ 290 pT $^{-1/2}$ when accounting for the 10 Hz equivalent noise bandwidth of the lock-in amplifier. We separately resolve a gradual temperature shift during this measurement (green curve), within the expected range of temperature stabilization. Note that for this method of temperature and magnetic field shift separation, signal errors add in quadrature.

3.3 Experimental details

3.3.1 Apparatus

A spatially filtered, 532 nm single-mode longitudinal excitation beam from a Verdi V5 or a homebuilt 50 mW direct green laser diode (OSRAM) is focused into the input facet of the diamond sample. Both frequency and spatial multi-mode excitation is feasible as long as the beam shape can be focused to the size of the input facet *i.e.*, below 300 μm diameter. Three sets of perpendicular Helmholtz coils, with diameters ranging from 8 to 12 inches, provide a uniform static or slowly varying magnetic field. Noise floor measurements were taken with a Halbach ring to provide a static magnetic field. Using ODMR spectra recorded with the application of three different control fields, the rotation matrix from the cartesian frame of the coils to the NV axis is determined. An impedance-matched loop antenna located ~ 5 mm above the sample delivers microwave excitation, with 40 dBm on the transmission line. The microwave excitation is frequency modulated at 1.5 kHz with a modulation depth of 1 MHz. Fluorescence emission is collected with an aspheric condenser lens (NA=0.79), followed by a $662 - 800$ nm bandpass filter to minimize NV^0 contribution to the fluorescence and a 532 nm notch filter to remove scattered pump excitation. A second condenser lens images the fluorescence onto a balanced large-area photoreceiver (New Focus 2307), which minimizes the effect of low frequency laser noise by balancing green input laser power. The system collection efficiency is $\sim 17\%$ of the total fluorescence signal, which is demodulated using a lock-in amplifier.

3.3.2 Advantages of using lock-in amplification

The use of lock-in amplifications has several advantages over direct readout of the ODMR curve. First, by modulating and demodulating the signal, low frequency electronics noise can be reduced. This is analogous to the advantage gained by using dynamical decoupling techniques to filter measurements of specific target frequencies. These pulsed techniques are also able to provide further improvement in sensitivity by taking advantage of the NV coherence. Secondly, the lock-in amplifier produces a derivative signal which can be approximated to be linear as it crosses zero. This vastly simplifies the curve fitting necessary for measurements, as the slope of the line can be measured as a scale factor and checked periodically in contrast to fitting Lorentzians to every acquired curve. To perform real-time sensing, extensive curve-fitting steps need to be minimized. For simultaneous measurement techniques utilizing frequency-locking, curve-fitting is eliminated.

3.3.3 Static magnetic field alignment

The magnetic fields were aligned to the NV axis using the iterative application of incremental test fields using low-noise current sources and a three-axis Helmholtz coil. This enabled the magnetic field to be applied axially to the NV, which in turn allows temperature separation along a single axis. Matlab was used to generate a rotation matrix from the lab frame to the NV frame. For the work presented in this chapter, we confirmed the alignment by minimizing the linewidth of the other three sub-ensembles – when the total magnetic field is aligned with one orientation, the other three orientations experience a degenerate field projection.

3.4 Conclusions and Outlook

3.4.1 Comparison with other magnetometers

Figure 3-3 shows the performance of the LTDW sensor compared to recently demonstrated NV magnetometers and other magnetometer platforms. The system noise limit from Figure 3-2a is superimposed over the frequency range. Also indicated are the sensitivity requirements for three key magnetometer applications: magnetocardiography, magnetoencelephography, and the monitoring of geomagnetics. The unique position of the LTDW in the low-frequency limit makes it suited for a variety of magnetic field sensing applications including medical monitoring, object detection, and the study of geomagnetics which occur in the 10^{-4} Hz to 10 Hz range. While

SQUID and atom-based magnetometry achieve better sensitivity at low frequencies, these technologies require cryogenics and vacuum systems that inhibit portability and versatility.

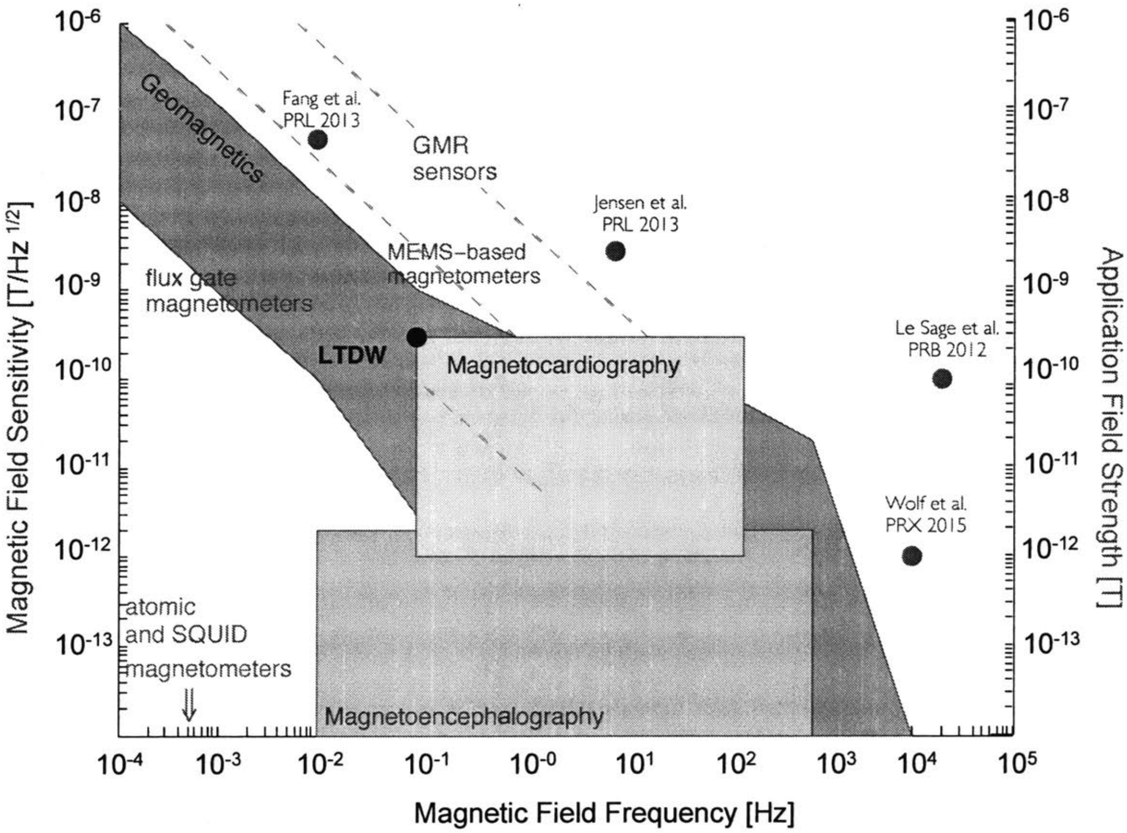

Figure 3-3: **Comparison of the LTDW (dark blue overlay) with other magnetometry technologies** Particularly with regard to target applications such as geomagnetics [1] shown in green (corresponding to the right axis), the LTDW achieves improved sensitivity with respect to other diamond-based sensors, shown in blue (corresponding to the left axis), in the important low-frequency band [2]. The LTDW's performance is competitive with other magnetometer platforms [3], shown in light blue.

3.4.2 Fundamental spin projection limit

For high-frequency magnetic field measurements, echo-type magnetometry could be employed with dynamic decoupling pulses to extend the NV electron spin coherence time [8]. In this regime, the sensitivity could approach the fundamental spin projection limit,

$$S = \delta B_{\mathrm{min}} \sqrt{T} \simeq \frac{1}{\gamma} \frac{1}{\sqrt{N\tau}}, \tag{3.1}$$

where δB_{min} is the minimum detectable magnetic field, T is the measurement time, $N = 10^{13}$ is the estimated total number of NV centers in our sample (see section 2.3.1), and $\tau \sim 1$ ms is the electron spin dephasing time measured with dynamical decoupling in comparable samples and expected to be feasible for NV densities on the order of 1 ppm [8]. Neglecting contrast and collection efficiency, these parameters predict a spin-projection limit of $S = 0.36$ fT/$\sqrt{\mathrm{Hz}}$.

3.4.3 Next steps and future applications

We have introduced a dual magnetic field and temperature sensor based on a light-trapping diamond waveguide geometry that enables nearly complete green pump absorption and efficient spin-dependent fluorescence collection. With more than two orders of magnitude improvement in pump power conversion over previous single-pass schemes, the LTDW achieves high signal to noise sensing and sub-nT/$\sqrt{\mathrm{Hz}}$ sensitivity in the low-frequency regime, which is not currently accessible by dynamical decoupling techniques. The power-efficiency of the LTDW allows it to be implemented with a compact, inexpensive laser diode excitation source. We measure a noise floor of less than 300 pT/$\sqrt{\mathrm{Hz}}$ in the sub-Hz regime. In this low-frequency domain, such high-sensitivity magnetometers promise new applications for solid-state sensors in a range of fields including biomedical sensing and object detection. The light trapping technique could be extended to transmission measurements and direct IR absorption techniques [15]. The device is not limited to sensing; it could be used for any application requiring a long optical path length within the sample such as electromagnetically-induced transparency-based experiments or optical quantum memories [50]. The LTDW provides a compact, portable precision sensor platform for measuring magnetic fields, temperature, pressure, rotation, or time. Via multiplexing, combinations of these sensing applications could be performed in a single compact device.

3.4.4 Simultaneous measurement of Zeeman-split resonances for high-dynamic-range vector magnetometry

Unlike the work described above, which utilizes sequential measurement of Zeeman-split resonances, a frequency-locking technique was also developed to monitor both resonances simultaneously. A closed-loop system that locks to the center frequency of an NV resonance allows for the steady-state operation of an NV magnetometer to be isolated from the phenomenological variables that determine the scale factor of previous lock-in-based approaches [51, 52, 53] (Fig. 3-4a). Furthermore, by virtue of locking to the NV resonance frequency, measurement is always performed in the approximately linear regime of the lock-in signal, and the full dynamic range of the NV center can again be accessed (Fig. 3-4b). The design has similar benefits and drawbacks as an atomic M_z magnetometer [54]; in particular, the bandwidth of an M_z configuration is limited by the modulation frequency which must be less than $1/T_1$ where T_1 is the longitudinal spin relaxation rate. The NV T_1 under optical excitation limits the modulation frequency to ≤ 20 kHz [51, 53]. Via frequency-generation and lock-in implementation on a custom built FPGA board, all four sub-ensembles can be addressed for vector measurements of magnetic fields.

The combination of atom-like long-term stability and vector capability in a compact, solid-state package makes NV-based magnetometers a prime candidate for use in a wide variety of field applications, from all magnetic navigation [55, 56] to prospecting for oil wells [57] to magnetic mapping of archaeological sites [58] to locating unexploded ordinance [59, 60, 61]. For practical operation in an unshielded field environment, however, a vector magnetic sensor also requires high dynamic range (~ 4 mT demonstrated in Fig. 3-4b) to be robust against rotation within the Earth's magnetic field, which may sweep measured magnetic field projections over a range up to ~ 130 μT. Using a frequency locking, multi-axis technique, scale-factor free, temperature-independent, vector magnetometry is demonstrated over a high dynamic range. This is a vital step forwards in taking the NV magnetometer from a laboratory demonstration to a functional device for detecting fields in an unshielded environment.

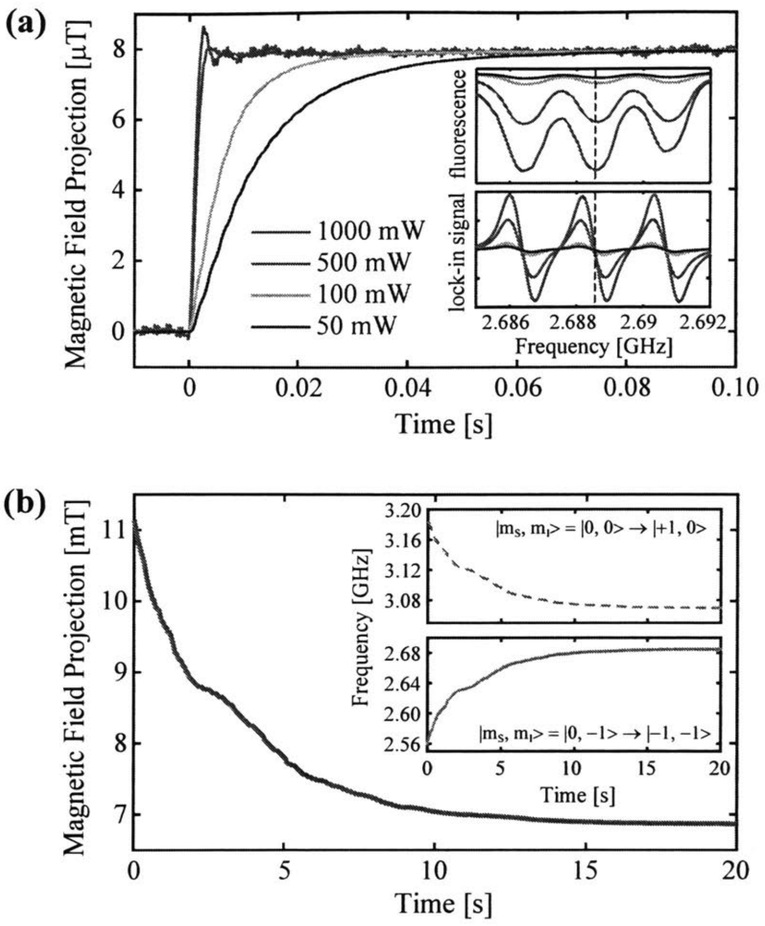

Figure 3-4: **Frequency-locking magnetometer** (a) Magnetic field step response of Zeeman splitting at different laser powers. Upper inset: ODMR spectra of a single NV resonance. Lower inset: ODMR spectra at the output of the lock-in amplifier. Dashed lines indicate the locked hyperfine transition. Note that changes in the laser power affect the contrast as well as the slope of the lock-in signal, degrading the accuracy of an open-loop measurement. In comparison, the steady-state frequency determined by the closed-loop measurement is consistent across the wide range of laser powers. (b) Dynamic range demonstration of the magnetic field produced by a free-moving permanent magnet varying projection by 4 mT during a continuous acquisition. Simultaneous measurements of the upper and lower resonance frequency of a single NV orientation class are shown in the insets.

3.4.5 Electrometry

Relying on a technique equivalent to that described for broadband magnetometry earlier in this chapter, a spin-based, all-dielectric sensor that uses an ensemble of NVs for electrometry is demonstrated. An applied electric field causes energy level shifts symmetrically away from the NV's degenerate triplet states via the Stark effect, and the symmetrical nature allows for robustness against temperature fluctuations (Fig. 3-5a). The use of the ensemble allows for a sensitivity to electric fields of more than two orders of magnitude improved over previous demonstrations. This electrometer operates under ambient conditions, at low frequencies (<10 Hz), over a large dynamic range (20 dB), and with nearly shot-noise limited sensitivities (≤ 5 V/cm/$\sqrt{\text{Hz}}$) as seen in Fig. 3-5b.

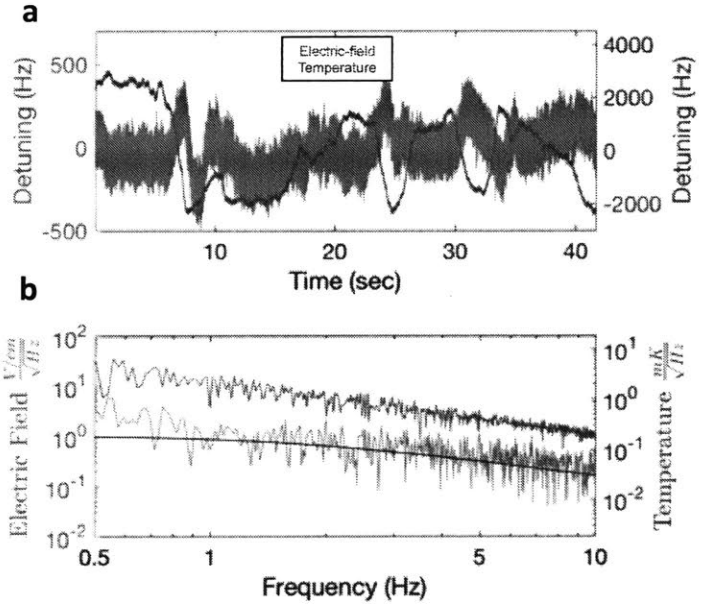

Figure 3-5: **Removing fluctuations from temperature from electric field measurements** (a) Time trace of the difference (electric field) and sum (temperature) of the lock-in-amplifier channels. Noise spectral density on the sum of the two channels, which corresponds to any common-mode fluctuations and is dominated by temperature instability in the diamond. (b) Noise spectral density on the time-trace difference (sum) of the two channels, which corresponds to the NSD of the transverse electric field (temperature) fluctuations. The shot-noise limit is given by the black line ($\frac{10}{\sqrt{2}}\,\frac{\text{Hz}}{\sqrt{\text{Hz}}}/\langle k_{\perp}\rangle_{225\text{V}} = 1.01\,\frac{\text{V/cm}}{\sqrt{\text{Hz}}}$).

The detection of weak signals in extremely low-frequency regimes with high spatial resolution is important for areas of research such as particle physics [62], atmospheric sciences [63, 64, 65], and neuroscience [31]. Commonly available electrometers that rely on electrostatic induction, like field mills [66] and dipole antennas [67], are physically limited in size to several tens of centimeters by the wavelength of the electric field of interest. This hinders miniaturization at frequencies below several

Hertz [68, 67, 69, 70]. Fully dielectric sensors allow sensing of electric fields without fundamental constraints on the size of the sensor and do not distort the incident field [71, 72]. Recent work towards the development of high spatial resolution electrometers include utilizing the electro-optic effect within solid-state crystals [73], and the electric field induced shifts of atom-based sensors such as trapped ions [74] or Rydberg atoms [75, 76]. However, such centimeter-scale sensors typically suffer from narrow detection bandwidths, require large peripheral equipment, and are highly susceptible to temperature instabilities. Compared with atom-based approaches, optically-addressable electron spins confined within solid-state materials allow for a higher density of spins with a reduced experimental footprint. This work brings diamond-based electrometry into a regime where it has a competitive sensitivity with a clear path towards miniaturization.

Chapter 4

Diamond NV electronic and nuclear spin-state anti-crossings under weak transverse fields

This chapter is adapted from:

> "Diamond-nitrogen-vacancy electronic and nuclear-spin-state anti crossings under weak transverse magnetic fields," H. Clevenson, E. H. Chen, F. Dolde, C. Teale, D. Englund, and D. Braje. Phys. Rev. A. 94, 021401(R).

4.1 Introduction

We report on detailed studies of electronic and nuclear spin states in the diamond nitrogen vacancy (NV) center under weak transverse magnetic fields. We numerically predict and experimentally verify a previously unobserved NV hyperfine level anti-crossing (LAC) occurring at bias fields of tens of gauss – two orders of magnitude lower than previously reported LACs at $\sim$ 500 G and $\sim$ 1000 G axial magnetic fields. We then discuss how the NV ground state Hamiltonian can be manipulated in this regime to tailor the NV's sensitivity to environmental factors and to polarize the nuclear spin state.

4.2 Energy levels of the diamond NV in the weak transverse magnetic field regime

4.2.1 Previous work in the transverse magnetic field regime and with level anti-crossings

NV defect centers in diamond are optically polarizable quantum systems with spin-dependent fluorescence. Using electron spin resonance (ESR) under ambient conditions, sensitivity to electric fields [16, 77, 78, 79], transverse and axial magnetic fields [7, 8, 9, 10, 11, 80], temperature [18, 19, 20, 37], strain [81], and pressure [82] have been observed via resonance frequency shifts of the NV ground-state manifold. Non-separable sensitivity to multiple environmental factors is problematic for to using the NV as a sensor. However, the Hamiltonian governing the measurable frequency shifts can be tailored to enhance (or to suppress) sensitivity to different physical phenomena. A magnetic bias field applied parallel or perpendicular ($B_{\|}$ or $B_{\perp}$ as shown in Fig. 4-1a) to the NV's axis in the diamond crystal lattice energetically separates the spin states and increases sensitivity to magnetic or electric fields, respectively.

Here, we investigate an unexplored weak-field regime in which electronic spin ground state energy level splittings are on par with the Zeeman shift induced by an applied magnetic field. We account for both the electron and the nuclear spin of the NV, which reveals complex dynamics of nuclear spin state degeneracy and previously unobserved hyperfine level anti-crossings. These features occur at low magnetic field ($B_{\perp} \lesssim 40\,\mathrm{G}$) as compared to the $B_{\|} \simeq 500$ G and $B_{\|} \simeq 1000$ G excited and ground state crossings [83, 84, 85, 86], which have been used for nuclear spin polarization, providing increased sensitivity to resonance shifts through narrower effective linewidth and increased contrast [87, 38, 88, 89]. We find excellent agreement between experiment and theory and discuss the utility of the nuclear spin degeneracy regime toward NV sensing applications and solid-state atomic memories based on nuclear spin polarization. While the results described here are specific to the NV, similar anti-crossings are expected in any spin-1 (or higher) defect center that shows hyperfine level splitting on the same order of magnitude as double-electron spin flip anti-crossings.

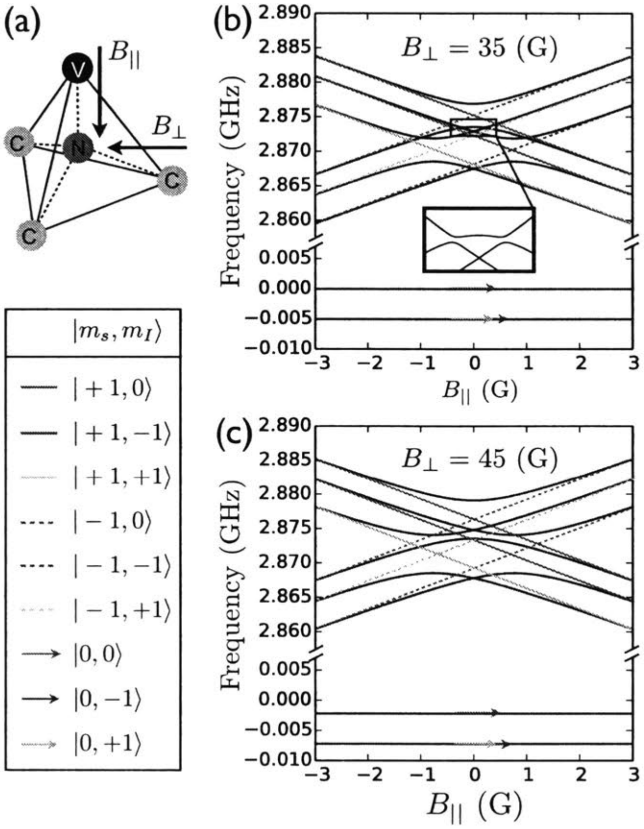

Figure 4-1: **NV energy levels with applied transverse magnetic field** (a) Axial and transverse magnetic field directions with respect to NV axis. As $B_\perp$ is increased from 35 G (b) to 45 G (c), the $m_I = 0$ energy levels are separated from the $m_I = \pm 1$ energy levels, removing the degeneracy which results in an electron-nuclear spin flip anti-crossing, which is detailed in the inset of (b). Non-dressed states are indicated with colored lines and dressed states are indicated with black lines.

4.2.2 Detailed Hamiltonian

The NV is a two-site defect with a spin-1 electronic ground state, which is magnetically coupled to nearby nuclear spins. For a single NV orientation, energy level shifts are described by the following spin Hamiltonian of the ground triplet state in the presence of magnetic, electric, and strain fields [27], taking into account the zero-field splitting, nuclear and electronic Zeeman shifts, Stark shifts, hyperfine splitting, and nuclear quadrupole effects:

$$\begin{aligned}\mathcal{H}_{gs} =&(hD_{gs} + d_{\|}\Pi_z)({S_z}^2 - \frac{1}{3}S(S+1)) \\ &- d_{\perp}[\Pi_x({S_x}^2 - {S_y}^2) + \Pi_y(S_xS_y + S_yS_x)] \\ &+ \mu_B g_e(\vec{S}\cdot\vec{B}) - \mu_n g_n(\vec{B}\cdot\vec{I}) \\ &+ A_{\|}S_zI_z + A_{\perp}(S_xI_x + S_yI_y) + P_{gs}({I_z}^2 - \frac{I^2}{3})\end{aligned} \tag{4.1}$$

where hD_{gs} is the NV ground state zero field splitting energy (which is temperature-dependent [37]), $d_{\perp}$ and $d_{\|}$ are the components of the ground state electric dipole moment, the total effective electric field $\vec{\Pi} = \vec{E} + \vec{\sigma}$ encompasses both static electric fields ($\vec{E}$) and strain ($\vec{\sigma}$), g_e and g_n are the electric and nuclear Landé g-factors, μ_B and μ_n are the Bohr and nuclear magneton constants, $\vec{B}$ is the applied magnetic field, $A_{\|}$ and $A_{\perp}$ describe the axial and transverse magnetic hyperfine interactions with the ^{14}N nucleus, P_{gs} is the nuclear electric quadrupole parameter, $\vec{S}$ is the electron spin operator, and $\vec{I}$ is the spin operator of the ^{14}N nucleus.

4.2.3 Double electron spin flip anti-crossing

Figure 4-1 shows the numerically calculated electronic ground state triplet and ^{14}N hyperfine energy levels, $|m_s, m_I\rangle$, where m_s is the electronic spin state and m_I is the nuclear spin state, as a function of axial magnetic field for a fixed transverse magnetic field. State-mixing-induced anti-crossings are seen when the dressed states (black lines) do not follow high-axial-field eigenstates (solid and dashed colored lines).

With the addition of a weak (< 3 G) axial magnetic field, we see mixing and crossing of the energy levels, resulting from off-diagonal terms in $\mathcal{H}_{gs}$ in the $|m_s, m_I\rangle$ basis. The double-electron spin flip anti-crossings occur as the non-dressed $m_s = 1$ states cross $m_s = -1$ states with identical nuclear spin, for example, as $|1, 0\rangle$ crosses $|-1, 0\rangle$. The transverse magnetic field leads to second-order mixing of the $m_s = \pm 1$ states, therefore the coupling strength E_g of these electronic Zeeman interaction driven level anti-crossings scales quadratically with the applied transverse magnetic field as described in [27].

4.2.4 Electron-nuclear spin flip anti-crossing

For transverse magnetic fields under $\sim$ 40 G, as shown in Fig. 4-1b, an additional level anti-crossing arises. As this phenomenon has not to our knowledge been previously described, we investigate it here in detail. The dressed $m_I = 0$ levels (black lines roughly following the red dashed and solid lines) cross the dressed $m_I = \pm 1$ levels (black lines roughly following the blue and yellow dashed and solid lines), resulting in further state mixing and an electron-nuclear spin flip anti-crossing. Solving for the eigenstates of $\mathcal{H}_{gs}$ indicates that transverse magnetic fields induce state mixing in the low axial magnetic field regime by bringing the nuclear spin states into resonance via the electronic Zeeman interaction $[\mu_B g_e(\vec{S} \cdot \vec{B})]$ in the presence of the transverse hyperfine interaction $[A_\perp(S_x I_x + S_y I_y)]$. This state mixing results in dressed states and affects which transitions are allowed by optical transition selection rules. As only electron spin flips (S_x and S_y operators) are considered in our calculation, the nuclear spin flip results from driving the electron spin flip. This is a spin-conserving process. For transverse magnetic fields larger than $\sim$ 40 G, the energy separation added by the transverse magnetic field removes the $m_I = 0$, $m_I = \pm 1$ level degeneracy; therefore, this additional anti-crossing is no longer present, leaving only the double-electron spin flip anti-crossing, which is not mediated by the hyperfine interaction.

Figure 4-2 depicts the double-electron spin flip and electron-nuclear spin flip anti-crossing coupling strengths (E_g, N_g) and the axial magnetic field positions (E_p, N_p) of these anti-crossings as a function of transverse magnetic field. As predicted in Ref. [27], the coupling strength of the double-electron spin flip anti-crossing is proportional to the applied transverse magnetic field squared: $E_g \simeq (\mu_B g_e B_\perp)^2/(D_{gs}+d_\parallel \Pi_z)$ in the weak electric field, weak axial magnetic field regime. These electron-spin flip anti-crossings are centered around $E_p = 0, \pm A_\parallel h/g_e \mu_B$. While E_g continues to increase as $B_\perp$ increases, N_g vanishes at $B_\perp \simeq 40$ G when the energy levels no longer overlap. The axial magnetic field position about which this anti-crossing is centered (N_p) goes to zero with increasing $B_\perp$ (see App. B).

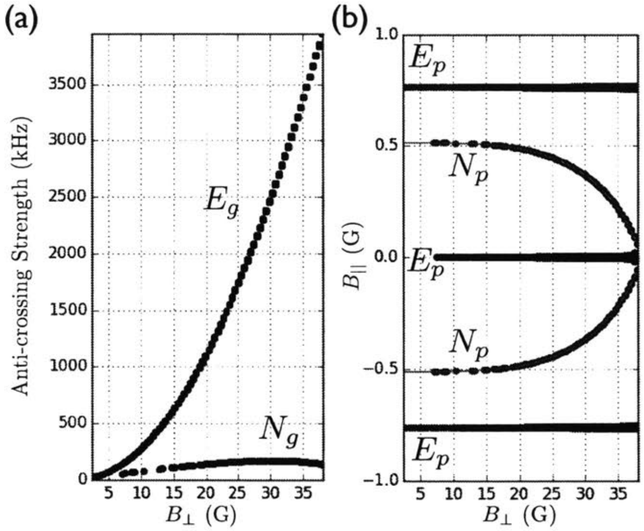

Figure 4-2: **Anti-crossing strengths and locations** (a) Anti-crossing coupling strength with increasing $B_\perp$. (b) Magnitude of small axial B fields at which the centers of these anti-crossings are observed. In both plots, the double-electron spin flip anti-crossing is marked E and the electron-nuclear spin flip anti-crossing is marked N. At fields greater than $B_\perp \simeq 40$ G, anti-crossing E continues to increase quadratically and anti-crossing N goes to zero as the energy levels no longer overlap.

Using second order degenerate perturbation theory, we calculate the change in energy as a function of applied magnetic and electric/strain fields. By solving for the axial magnetic field ($B_{||}$) at which the intersection of the $|m_I = 0\rangle$ and the $|m_I = 1\rangle$ energy levels occur, we obtain a closed-form solution for the location of the electron-nuclear spin flip level anti-crossing. This is in good agreement with our numerical results as seen in Fig. 4-2.

$$N_p = \frac{-A_{||} D_{gs} \xi + |P_{gs}| \sqrt{\xi ({D_{gs}}^2 \xi + B_\perp^4)}}{2 D_{gs} \xi} \tag{4.2}$$

where $\xi = {A_{||}}^2 - {P_{gs}}^2$, $A_{||}$ is the axial hyperfine interaction, D_{gs} is the zero field splitting, P_{gs} is the quadrupole energy, and $B_\perp$ transverse component of the magnetic field in the NV frame of reference. Figure 4-5 depicts this transverse field regime. Numerical solutions to $\mathcal{H}_{gs}$ accounting for selection rules are shown in conjunction with experimental data.

4.3 Experimental apparatus

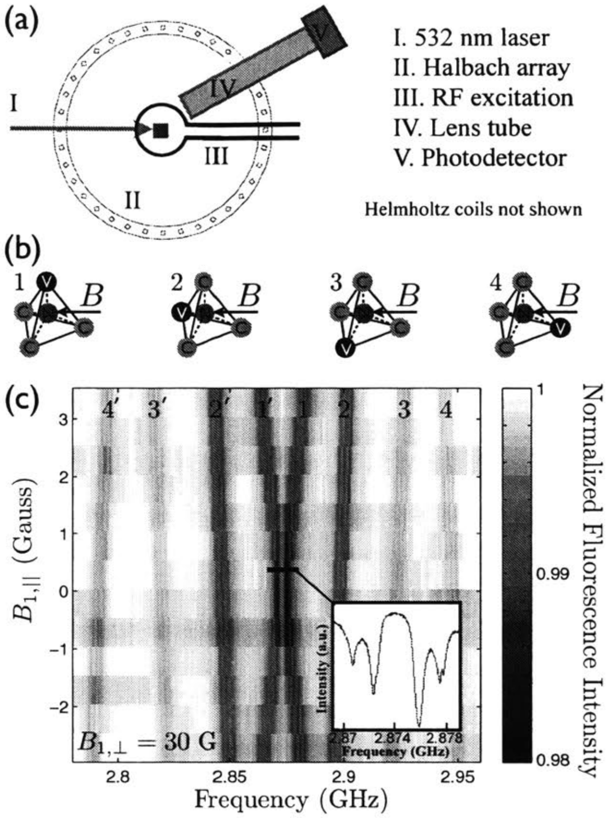

Figure 4-3: **Apparatus and NV orientations with applied magnetic field** (a) Experimental setup. (b) The four orientation sub-ensembles of NV centers are shown with an applied magnetic field. (c) An anti-crossing strength of ~ 2.6 MHz is seen in sub-ensemble 1 when the perpendicular component of the B field ($B_{1,\perp}$) is equal to 30 G and the axial component of the B field ($B_{1,\parallel}$) is varied around zero field. Inset shows a high resolution spectra of resonance 1 and 1′.

We experimentally validate this anti-crossing by performing ESR measurements on an NV ensemble. The epitaxially-grown diamond is polished to trap the green pump light and guide the red spin-dependent fluorescence to a photodetector in a light-trapping diamond waveguide geometry [90]. We estimate the intrinsic strain in this sample to be $\sim 3 \times 10^{-5}$ from the ~ 600 kHz strain splitting of the central hyperfine resonance at zero applied field, given values of $d_\perp$ from the literature [17]. We expect this to be the average strain experienced across the sample. The NV has four orientations in the diamond lattice, labeled as $k = 1, 2, 3, 4$ as seen in Fig. 4-3b. We lift the $m_s = \pm 1$ degeneracy and the orientation degeneracy by applying a static magnetic field at an angle resulting in non-equivalent projections onto each orientation. A 60 G Halbach array (magnitude uniformity $>$ 99% over a 2 cm^3 volume at the center) is positioned around the sample (Fig. 4-3a) to provide this static magnetic field. In addition, up to ±30 G can be applied in $\hat{x}$, $\hat{y}$, or $\hat{z}$ (lab frame) using Helmholtz coils. The total magnetic field is aligned to be perpendicular to the $k = 1$ orientation. A weak axial magnetic field sweep ($B_{1,\parallel}$) in addition to this transverse field confirms the anti-crossings in the ESR spectra (Fig. 4-3c). Each NV orientation produces two Zeeman-split ^{14}N nuclear hyperfine triplets. These pairs are located symmetrically around $\omega_c = D_{gs} + \frac{3{\mu_B}^2 {g_e}^2}{2\hbar^2 D_{gs}} {B_\perp}^2$. In levels 1 and $1'$, for which the magnetic field is perpendicular, we observe both predicted anti-crossings around $B_{1,\parallel} = N_p$. This is highlighted in the inset to Fig. 4-3c.

4.4 Experimental verification

4.4.1 Double electron spin flip anti-crossing

While Fig. 4-1 gives insight to the origin of the level anti-crossings in the energy level diagram, Fig. 4-4 shows the corresponding energy level transitions at $B_\perp = 35$ G and 45 G. Numerical solutions to $\mathcal{H}_{gs}$ accounting for S_x and S_y operators in the selection rules are plotted in conjunction with the experimental data. For both values of transverse field, we clearly see double-electron spin flip anti-crossings centered at $B_\parallel = 0, \pm A_\parallel h / g_e \mu_B$ G (Fig. 4-2b) with anti-crossing coupling strengths corresponding to those expected from Fig. 4-2a. As expected, we also see the center frequency between the split resonances increase with increased applied transverse magnetic field.

4.4.2 Electron-nuclear spin flip anti-crossing

Figure 4-5 concentrates on the region of interest at $B_{1,\perp} = 30$ G around which the electron-nuclear spin flip anti-crossing is maximized. We observe the electron-nuclear spin flip anti-crossing at $\sim \pm 0.35$ G applied axial magnetic field as predicted by analytically solving $\mathcal{H}_{gs}$ (see App. B). Double-electron spin flip anti-crossings are

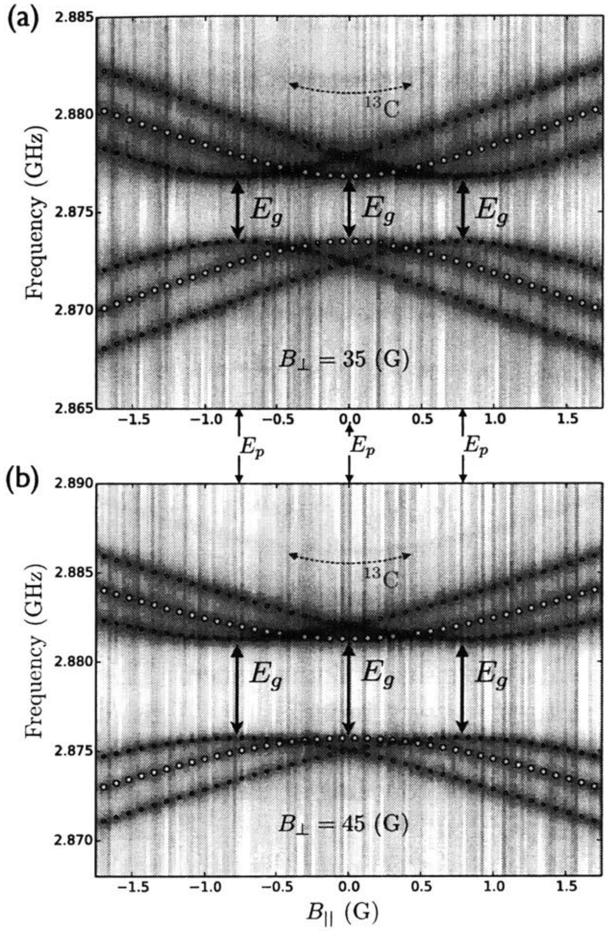

Figure 4-4: **Plots of transition energies as a function of axial magnetic field under fixed transverse magnetic field** Transitions for $B_\perp = 35$ G and $B_\perp = 45$ G are shown, which correspond to the energy levels in Fig. 4-1. Greyscale indicates normalized fluorescence. Double-electron spin flip anti-crossings of coupling strength E_g are seen at $E_p = 0, \pm A_\| h/g_e\mu_B \simeq \pm 0.75$ G. ESR in diamond with a natural abundance of carbon isotopes has additional resonances due to hyperfine interactions with the $\sim 1\%$ (I=1/2) ^{13}C nuclear spins; these features are visible at correspondingly lower contrast in both (a) and (b).

centered at $E_p = 0, \pm A_\| h/g_e\mu_B$ (Fig. 4-2b) with anti-crossing coupling strengths corresponding to those predicted by simulation and plotted in Fig. 4-2a. Note the excellent agreement between experiment and theoretical model.

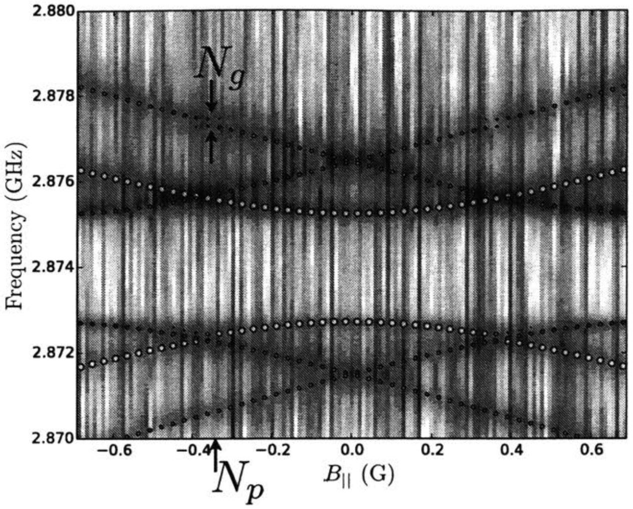

Figure 4-5: **Double-electron and electron-nuclear spin flip anticrossings** Detail of double-electron and electron-nuclear spin flip anti-crossings at $B_\perp = 30$ G, where greyscale represents normalized fluorescence. The RF excitation power was reduced by 10 dB to mitigate power broadening. This allows the higher-resolution features to be observed, however, it is at the expense of signal-to-noise ratio. Electron-nuclear spin flip anti-crossings of coupling strength $N_g \simeq 250$ kHz are seen centered around $N_p \simeq \pm 0.35$ G, separated in frequency by P_{gs} at 2.877 GHz and 2.872 GHz. Numerical solutions to $\mathcal{H}_{gs}$ are plotted over the data, with the diameter of the circles correspond to the probability of the transition.

4.5 Conclusions and outlook

4.5.1 Utility for sensing

The numerical simulation of $\mathcal{H}_{gs}$ in the $\lesssim 40$ G transverse-field regime gives insight into the level structure and the region where the crossings and anti-crossings can be seen; here we describe several useful applications in sensing and atomic memories. First, the double-electron spin flip anti-crossing addresses the ever-present challenge of isolating sensitivity to multiple fields by suppressing sensitivity to changes in axial magnetic fields. As the applied transverse magnetic field is increased, the strength of this anti-crossing increases quadratically, and the range of $B_{||}$ to which the NV ensemble is insensitive increases [77]. This is especially useful for electric field and temperature sensing, where the effects of magnetic fields can limit sensitivity.

Secondly, the double-electron spin flip anti-crossing causes two of the three hyperfine transition levels to cross. At these degeneracies, ESR spectra experience doubled signal contrast. In CW diamond-based sensing applications, where sensitivity is linearly proportional to the ESR resonance contrast, twice the sensitivity is expected in this regime. Furthermore, as this anti-crossing strength increases and the hyperfine transition levels are compressed in energy spacing, all three nuclear levels can be effectively degenerate, providing up to a factor of three increase in sensitivity to electric fields or temperature. Up until now, we have shown experimental-theory agreement for the six hyperfine transitions present in a ^{14}N sample, where the nuclear spin $I_{^{14}N} = 1$. Note that the four transitions present in ^{15}N allow for a complete nuclear spin degeneracy at zero applied axial magnetic field (see Section 4.5.2).

Next, we propose a transverse-field method to remove temperature sensitivity from diamond-based magnetometry measurements. Taking the derivative of ω_c with respect to temperature, the temperature-dependent D_{gs} term in the denominator of the second order term leads to a decrease in $d\omega_c/dT$ with increased transverse magnetic field [37]. We expect a 1% decrease in $d\omega_c/dT$ with 80 G applied transverse magnetic field. Combining this advantage with the aforementioned increase in contrast and insensitivity to changes in B_z in a high signal-to-noise ratio light-trapping diamond waveguide results in a regime that is well-suited for temperature-stabilized measurements, relying on the ability to probe multiple sub-ensembles with different crystallographic projections of the applied transverse magnetic field. Using these multiple sub-ensembles with known temperature dependences allows the temperature dependence to be stabilized, similar to the method proposed by Hodges *et al.* using strain engineering [22]. This method further decouples the diamond from its thermal environment, addressing an ongoing challenge in diamond-based electric and magnetic field sensing.

4.5.2 Implementation with ^{15}N

Unlike ^{14}N, which is a spin-1 system, ^{15}N is a spin-1/2 system. The hyperfine splitting of the NV center would therefore result in two resonances ($\pm 1/2$) instead of three resonances ($0, \pm 1$). This gives a 50% increase in contrast, which is linearly proportional to sensitivity. Furthermore, at zero applied axial magnetic field ($B_{\parallel} = 0$) full contrast is achieved, even at non-zero applied transverse magnetic fields. The electron-nuclear spin flip anti-crossing is not present in the ^{15}N case. Under a transverse magnetic field, the two nuclear spin states mix. Therefore the application of a linearly polarized microwave field induces transitions between all (2×2) possible states, giving rise to the doublets of the ODMR spectrum in Fig. 4-6a.

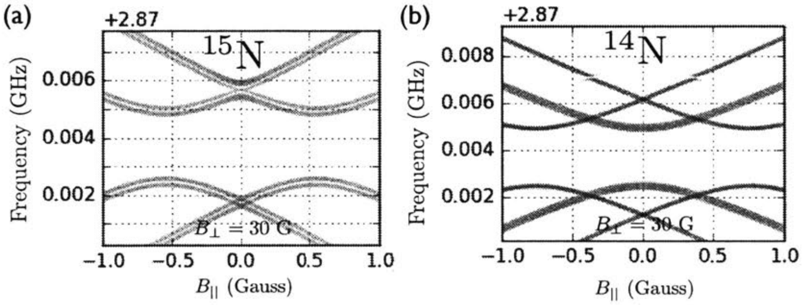

Figure 4-6: **Simulation with ^{15}N** Comparison of ^{15}N (a) and ^{14}N (b) samples at $B_{\perp} = 30$ G.

4.5.3 Adiabatic passage protocol for nuclear spin polarization

Using these low-transverse-field anti-crossings, we introduce an alternate route to polarize the nuclear spin host of the nitrogen vacancy center [87, 91, 92, 93, 94]. This method articulates successive shifting of the magnetic field and radio-frequency pulses iteratively to transfer the spin polarization into a single nuclear state, similar to methods explored for optical quantum dots [95, 96, 97]. Unlike existing schemes at $\sim$ 500 G and $\sim$ 1000 G axial magnetic fields for the excited state and ground state LACs, this approach relies on control of weak magnetic fields and state-selective RF pulses. It requires fewer pulses and a smaller range of RF excitation than other low-magnetic field recursively repeated protocols [98]. The heart of the scheme relies on adiabatic passage, which results in a change in nuclear spin state. Following Landau-Zener-Stueckelberg theory [99, 100, 101], the probability P of adiabatic passage through an anti-crossing with coupling strength Δ is $P = 1 - e^{(-\pi h \Delta^2 / 2 \frac{d\Lambda}{dt})}$ where $\frac{d\Lambda}{dt}$ is the rate of change of energy difference as the gap is approached. Under these conditions, sweeping a bias field through the $\pm B_{\parallel} = N_p$ electron-nuclear spin flip anti-crossing results in spin exchange from $|m_s = \mp 1, m_I = \pm 1\rangle$ to $|m_s = \pm 1, m_I = 0\rangle$. For a 99.99% probability of adiabatic passage, a rate of magnetic field change of $\frac{1\ \mathrm{G}}{225\ \mu\mathrm{S}}$ is required.

While many nuclear spin exchange sequences are possible, here we note a two-step example to polarize into $m_I = 0$. Assuming an initial ensemble of NVs in a superposition of eigenstates $|0, -1\rangle$, $|1, 1\rangle$, and $|1, 0\rangle$, which can be prepared through state-selective excitations, a single application of the protocol results in a superposition of eigenstates $|0, -1\rangle$, $|1, 0\rangle$, and $|-1, 0\rangle$. The population transferred through the electron-nuclear spin flip anti-crossing is then shelved in $m_s = 0$ and the remaining population in $|0, -1\rangle$ is transferred to $|-1, -1\rangle$ with a resonant RF pulse. The second application of the protocol then results in eigenstates $|-1, 0\rangle$, $|0, 0\rangle$, and $|1, 0\rangle$. Exploiting the robustness of the nuclear spin state against optical excitation of the NV, all m_s levels can be pumped into the $m_s = 0$ with green laser excitation [102]. This type of protocol would be useful both for environmental sensing applications, due to the increased contrast, but also for applications like diamond-based gyroscopes [41, 103] and atomic memories [104, 94, 105], which utilize the longer-lived nuclear spin state.

4.5.4 Next steps and future applications

The transverse magnetic fields may help overcome the influence of inhomogeneous strain present from diamond growth processes, a challenge in working with very large ensembles of NV centers. Combining this with insensitivity to small axial magnetic fields and potential insensitivity to temperature, the resultant system also presents itself as a strong candidate for a quantum memory. Transverse and axial magnetic fields could be used to read and write to the system, which is otherwise isolated from its environment.

In conclusion, in this work we present a study of the effect of weak transverse magnetic fields on the NV system. We predict and experimentally verify an electron-nuclear spin flip anti-crossing, with close agreement between theory and experiment.

We also experimentally measure the predicted double-electron spin flip anti-crossing under transverse magnetic fields. These anti-crossings show potential for a variety of sensing applications because of (i) increased signal contrast, (ii) insensitivity to axial magnetic fields near the anti-crossing points, (iii) potential for nuclear spin polarization schemes, and (iv) selective decoupling of the NV from its environment through the use of different orientations with varying transverse fields. With applied transverse magnetic fields on the order of tens of gauss, we can achieve increases in contrast on the order of those seen previously only at the much higher, axially-applied ~ 500 G and ~ 1000 G LACs.

Chapter 5

Toward a diamond-based frequency standard

5.1 Introduction

Precision clocks and oscillators are crucial for a range of applications including navigation, computing systems, and communications. Some of the most accurate time and frequency standards developed to date are atomic clocks, which derive their stability from electronic transitions in vapor-phase atoms. Most modern atomic clocks rely on precisely measured internal hyperfine level splitting of atoms. However, as the focus is optimizing the stability, such clocks often require a volumes of up to several tens of cubic meters, too large for many applications. At the other extreme, research has been directed toward miniaturizing atomic clocks for applications such as satellites and *in situ* scientific instruments. Much research has focused on miniaturizing such systems, resulting in chip-scale vapor cells [106], ultra-cold atomic traps [107], and vertical-cavity surface-emitting lasers [108]. Moreover, commercially available compact cesium clocks now achieve a fractional frequency deviation of $6 \times 10^{-10}/\sqrt{\text{Hz}}$ [109], representing roughly 100 times better timing stability than temperature-stabilized quartz oscillators in a package only 17 cm^3 in volume.

Concerted research efforts to miniaturize atomic clocks have resulted in on-chip devices employing small vapor cells that are integrated with detectors and laser sources [110, 111]. Solid-state alternatives could not only reduce the volume, but could also enable better performance in harsh environments. Smaller devices could enable high-performance clock generators for short-range next-generation wireless (millimeter-wave) communications, since existing quartz oscillators suffer from high phase noise at high frequencies [112]. In addition, mobile devices can derive an accurate time signal from GPS for maintaining communication standards [113], but are susceptible to obstruction or jamming of the external clock signal, whereas a portable high-performance clock that is small enough to be incorporated into mobile devices could maintain synchronization.

Ref. [22] suggests a pulsed protocol that, addressing a very large ensemble of NV centers, could realize a solid-state clock approaching the stability of chip-scale atomic clocks. This protocol for a stable oscillator is based on magnetic sublevel transitions in the diamond NV center. This protocol exploits the NV's long spin coherence time and relies on using a large number of NV centers. It is estimated that its frequency stability could rival the performance of the newest chip-scale Cs and Rb clocks in a package that is at least 2 orders of magnitude smaller and lighter. Developing an atom-like standard in a solid-state host could enable its integration into semi-conductor fabrication processes, which could lead to reductions in volume and power requirements. The light-trapping diamond waveguide (LTDW) is an excellent candidate for addressing large ensembles of NV centers. The proposed clock protocol is a spin-echo technique that eliminates magnetic field effects to first order, but is sensitive to fluctuations in temperature. In this chapter, several methods to combat these temperature fluctuations are described, including strain engineering and the application of a transverse magnetic field. The feasibility of practical diamond-based timekeeping is assessed, and the steps towards its implementation are outlined.

5.2 Clock protocol

The protocol relies on the manipulation of the spin-1 NV ground state [114], as illustrated in Figure 1-1. The NV center is first prepared into the spin-1 ground state $|0\rangle$. A pulsed technique is used to monitor the frequency drift. Similar to the Ramsey spectroscopy used in atomic clocks, this results in a fluorescence response that varies with respect to frequency drift, $\delta\omega$. The clock protocol modifies a traditional spin-echo protocol, changing the flip-angle of the first and last pulses from $\pi/2$ to $\pi/4$. After performing the clock protocol, the NV is in state $|\psi_f\rangle = U_{clock}|\psi_0\rangle = \frac{1}{\sqrt{2}}\sin(\delta\omega\tau)|0\rangle - \frac{1}{2}\cos(\delta\omega\tau)(|{+1}\rangle + |{-1}\rangle)$. This drift-dependent sinusoidal signal acts as a long-time-scale correction to a lower stability voltage controlled oscillator (VCO) used to drive the RF field at ~ 3 GHz.

The figure of merit for the stability of a frequency standard is fractional frequency deviation. This is a measure of frequency stability that indicates how much an oscillator drifts around its natural frequency. Equation 5.1 describes how the fractional frequency deviation is related to the observed fluorescence signal $\langle\hat{M}\rangle$.

$$\frac{\delta\omega}{\omega_0} = \frac{1}{\omega_0}\frac{\Delta\hat{M}}{|\partial\langle\hat{M}\rangle/\partial\omega|} \tag{5.1}$$

where $\Delta\hat{M} = \sqrt{\langle\hat{M}^2\rangle - \langle\hat{M}\rangle^2}$ is the standard deviation of the operator describing the spin expectation value for the fluorescence measurement and $|\partial\langle\hat{M}\rangle/\partial\omega|$ is the maximum slope of the the signal as it changes with frequency drift.

To facilitate comparison between systems and recognize that multiple measurements will improve the SNR term, we can simplify this to Equation 5.2, where τ is time separation between the pulses, $T = M\tau$ is the total interrogation time for M measurements, and N is the number of NVs in the ensemble. Similar to magnetic field sensitivity, maximizing the collection efficiency of the system as well as the contrast will improve this metric.

$$\left\langle\frac{\delta\omega}{\omega_0}\right\rangle_{M,N} \propto \frac{1}{D_{gs}\sqrt{\tau N T}} \tag{5.2}$$

5.3 Demonstration

5.3.1 Single-NV clock

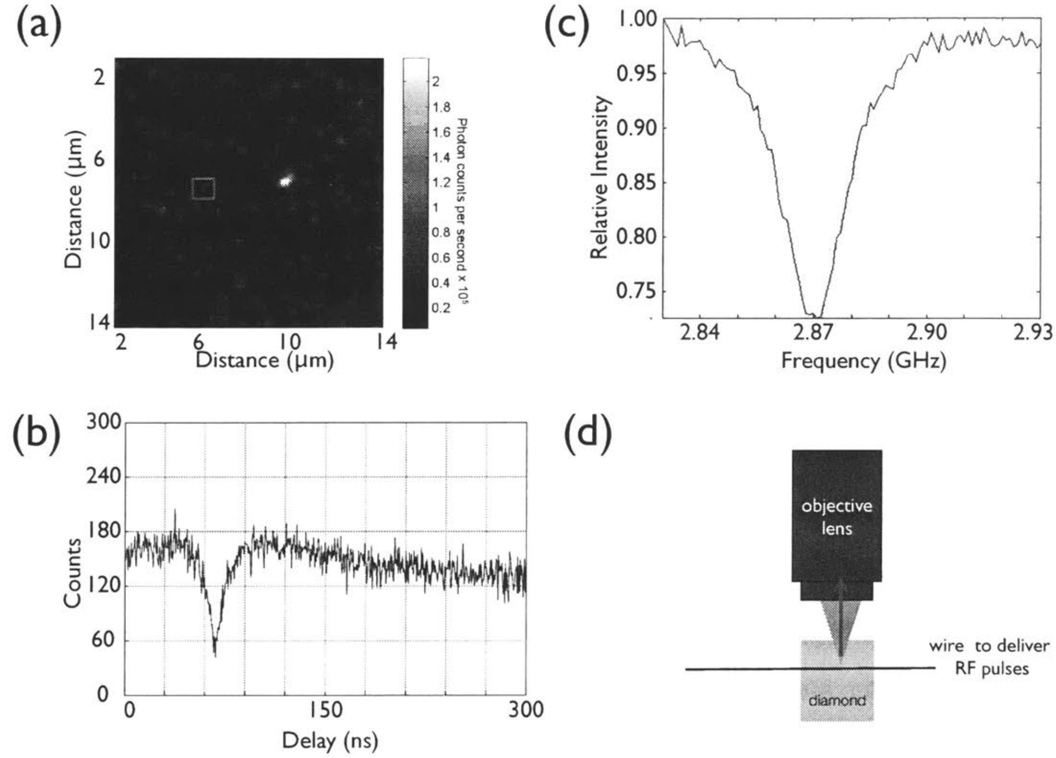

Figure 5-1: **Characterization of single NV** (a) Raster scan of the fluorescence of the diamond sample when pumped with 532 nm green light. The NV used is noted in red. (b) $g^{(2)}$ plot for this NV, verifying that it is a single defect. (c) CW ESR plot for this defect center, indicating that the resonance frequency is at 2.87 GHz as is typical. (d) Diagram of setup used to perform measurements on this defect center.

Here, we demonstrate the clock protocol on a single NV center, demonstrating a fractional frequency deviation of $2 \times 10^{-6}/\sqrt{\text{Hz}}$. To confirm that the NV being interrogated is a single emitter, a fluorescence image (Fig. 5-1a), a $g^{(2)}$ scan (Fig. 5-1b), and a CW ESR scan (Fig. 5-1c) are recorded. The experimental setup is shown in Fig. 5-1d. Using a confocal microscope, NV center is excited using a 532 nm green laser. Microwave pulses are applied using a 15 µm wire approximately 20 µm from the target NV. The photoluminescence signal is spectrally filtered from the input signal and sent to the detector. A slight splitting in the CW ESR signal for this NV center is observed, which may be caused by a small magnetic field or by intrinsic strain in the diamond. To first order, however, this field does not affect the operation of the clock protocol [22]. This slight magnetic field causes the visible beat frequencies in Fig. 5-2. From this plot, $\pi/4 \simeq 22$ ns and the $\pi \simeq 88$ ns.

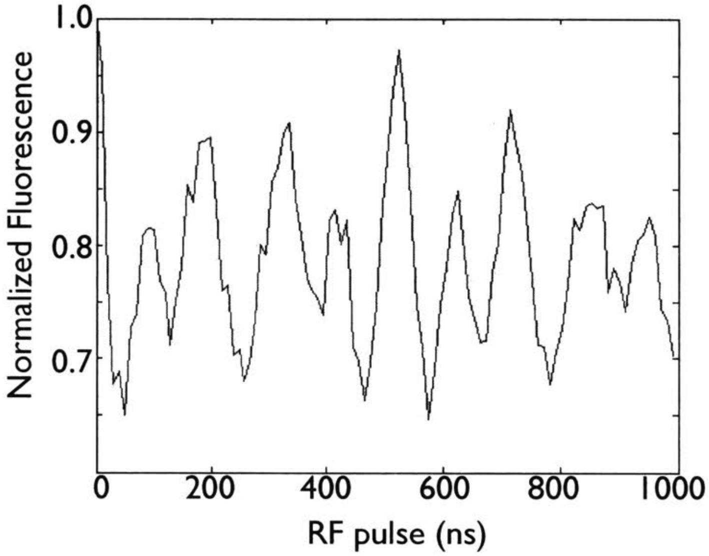

Figure 5-2: **Rabi oscillations of single NV center** Signal from a single NV center is measured as RF pulses of varying duration are applied. A slight beat frequency is visible, due to a small environmental magnetic field and/or strain splitting. A $\pi/4 pulse is determined to be \sim$ 22 ns and a $\pi pulse is determined to be \sim$ 88 ns.

Substituting directly into Equation 5.1, using the standard deviation of the $\pi/4$ point on the curve and the slope around it, we find a fractional frequency deviation of 2×10^{-6} for $\tau = 10$ μs. This corresponds to a thermal stability of ~ 80 mK, which might be expected for a diamond sample with no thermal management, and indicates that the single NV case is likely limited by thermal fluctuations.

5.3.2 Small-ensemble clock

The first step towards the demonstration of the clock protocol on an NV ensemble is the implementation of pulsed ESR and Rabi oscillations. Here, a small ensemble ($\sim 10^6$ NVs) is implemented in a non-LTDW geometry. Using a single-pass, confocal setup, clear Rabi oscillations are seen.

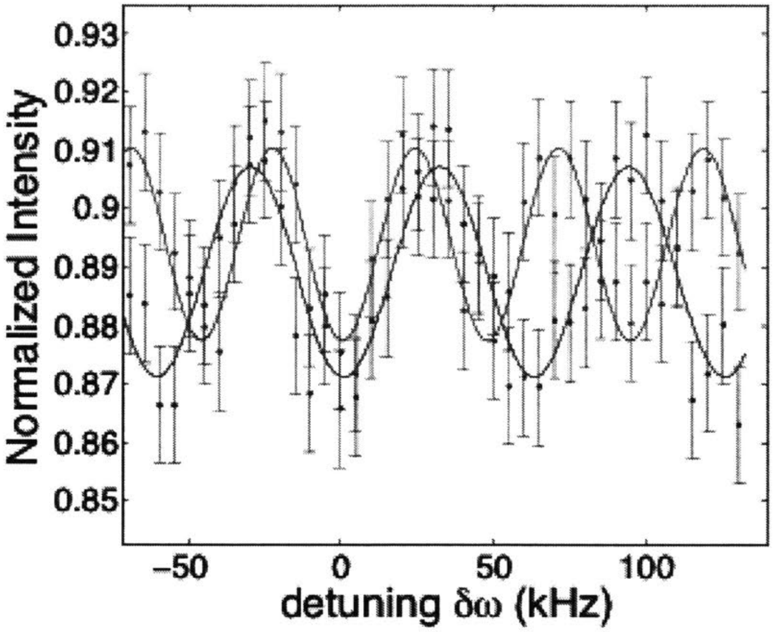

Figure 5-3: **Single-NV clock** Sinusoidal fits to the data are found to have R-squared values of 0.73 and 0.8 for $\tau = 8$ µs (blue) and $\tau = 10$ µs (red) respectively.

In Figure 5-4, Rabi oscillations are shown on the left and the clock protocol is shown on the right, for $\tau = 2$ µs (blue) and $\tau = 4$ µs (red). For the fits, the height, contrast, and location of zero detuning were adjusted, but the frequency of oscillation was not. The fractional frequency deviation is calculated to be $\sim 10^{-7}$, a minor improvement over the single-NV clock. This is consistent with both implementations being limited by ambient temperature fluctuations.

5.4 Pulsed protocols using a LTDW

5.4.1 RF Uniformity & Antenna development

Non-uniformity of the applied RF field in pulsed protocols results in a degradation of the signal, since RF field amplitude affects the π pulse time. This is particularly relevant in systems like the LTDW where the NVs are distributed over a large area. For ensembles on the order of 100 µm^2, a mm-scale loop of wire provides adequate improvement over the straight length of wire commonly used in single-NV experi-

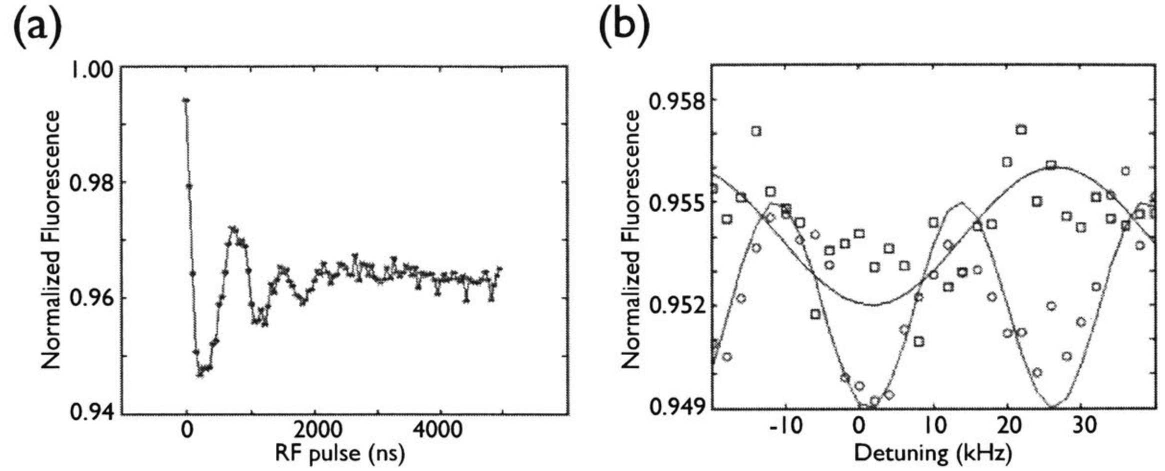

Figure 5-4: **Small-ensemble NV clock** (a) Demonstration of Rabi oscillations. (b) Demonstration of the clock protocol on a small ensemble of NV centers, with the y-axis shows normalized fluorescence and x-axis shows detuning from resonance in Hz

ments. However, this is inadequate for NVs spread out across several millimeters, as in the case of the LTDW. A more uniform field can be realized with a Helmholtz coil geometry. However, the inductance of the coils prevents GHz field switching. Recent work has shown spatial uniformity across millimeter-scale areas [115, 116] using split ring resonator antennas. These antennas are extremely narrow band and not suited for magnetometry experiments requiring an applied bias field. Other designs use more broadband "lollipop" geometries to accommodate high-dynamic-range measurements [117]. Adequate power delivery remains a challenge for large-ensemble-based NV sensing, possibly surmountable through extensive engineering. Additionally, alternative methods of exciting the transitions have been explored [118]. Lab-based investigation into alternative antenna designs, ranging from PCB-based loops and spirals to coax loops with a variety of grounding configurations to three dimensional resonant cavities have not, to date, yielded a result with significant improvement over a 4 mm loop of wire. As such, the demonstrations of pulsed protocols in Section 5.4.2 are limited by the non-uniform RF field amplitude across the sample.

One method to overcome the nonuniformity without engineering a custom antenna is to use dynamical decoupling [119] and optimal control techniques [120], such as those designed using the DYNAMO package [121, 122]. We estimate that these techniques are most helpful if the RF inhomogeneity is limited to a few percent across the NV volume; otherwise, the Rabi oscillation signal from one part of the sample can directly cancel that from another part which experiences a 180 degree phase shifted pulse.

5.4.2 Demonstration of Rabi oscillations, Hahn Echo

Given the known limitations due to the RF-inhomogeneity of a 4 mm loop antenna used to apply RF to the 3 mm square LTDW sample, it is not surprising that the resulting Rabi oscillations from the ensemble begin to cancel each other rapidly. Figure 5-5 shows Rabi oscillations as the microwave pulse is increased from 10 ns to 3000 ns. This is the first step towards determining the correct duration for π pulses and other pulses as the basis for more complex sensing applications.

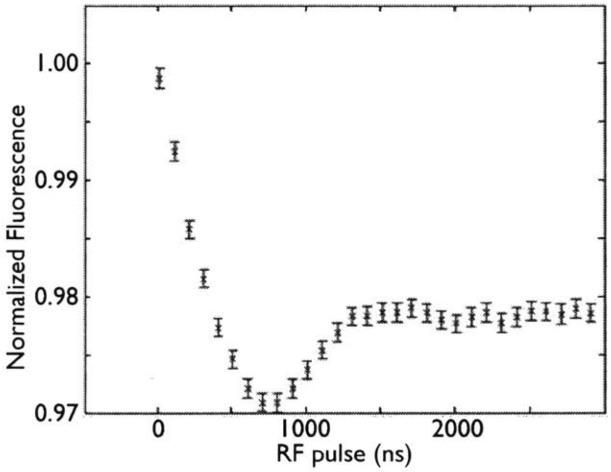

Figure 5-5: **LTDW Rabi oscillation** Rabi sequence performed on the LTDW platform shows slow, attenuated oscillation with low contrast.

Next, a pulsed ODMR experiment is performed. Taking the π rotation time from the Rabi oscillation plot to achieve maximum contrast ($\sim$ 710 ns) we sweep the microwave excitation at zero applied field. Imperfect RF uniformity results in visible sidebands.

Figure 5-6 shows a Hahn Echo sequence ($\pi/2$ τ π τ $\pi/2$) with revivals out to $\tau \sim 200$ μs using the LTDW sample. The spacing of the revivals corresponds to the

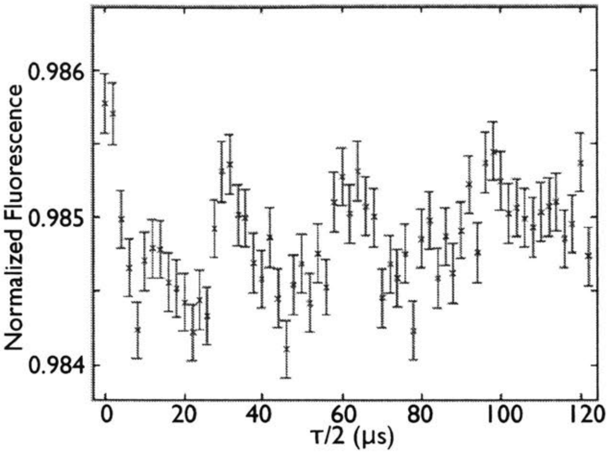

Figure 5-6: **LTDW Hahn echo** Hahn echo sequence performed on LTDW platform is characterized by low contrast and poor SNR. Revivals are noted out to $\tau \sim 200$ μs.

total applied magnetic field of roughly 35 G. The coherence time measured here is of the same order of magnitude as coherence times measured on single nitrogen-vacancy defect centers in a comparable sample on a confocal microscope setup previously. However, the SNR seen in this result is low, indicating that likely only a small percentage of NVs are being addressed in this scan.

5.5 Decoupling from temperature effects

5.5.1 Theoretical improvement

By engineering two ensembles of NV centers where each zero field splitting frequency has a different different dependence on temperature $\left(\frac{dD_{gs}}{dT}_n = \beta_n\right)$, we can obtain a fractional frequency deviation that is a factor of $\xi \equiv \sqrt{1 + 2(\frac{\beta_1}{\beta_2 - \beta_1})^2}$ worse than that of the ideal (zero temperature fluctuation) case. Even in the single NV clock, this stability limit is an improvement over the temperature-limited stability. To get as close as possible to the ideal result, the difference between β_1 and β_2 should be maximized.

The tetrahedral lattice of the diamond provides four convenient sub-ensembles of NVs that experience identical temperature fluctuations, due to the excellent thermal conductivity of diamond. Two methods of altering dD_{gs}/dT will be explored in this section.

5.5.2 Changing dD_{gs}/dT using transverse magnetic fields

By solving for the energy eigenvalues of the Hamiltonian detailed in Section 1.1.2 and applying second order energy corrections, we find that the zero field splitting can be described by $\omega_{ZFS} \simeq D_{gs} + \frac{3\mu_0^2 g^2 B_\perp^2}{2h^2 D_{gs}}$.

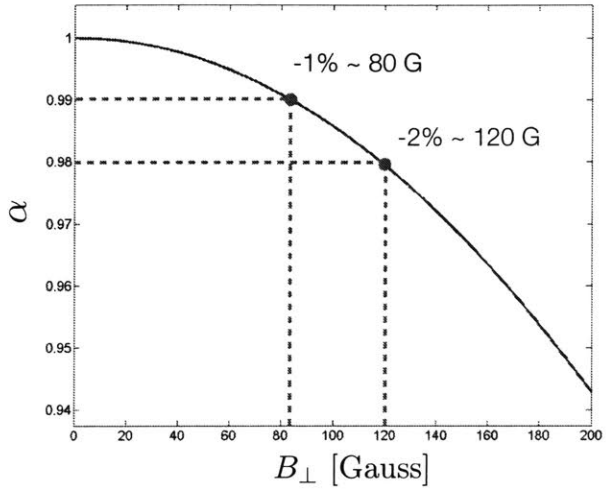

Figure 5-7: **Change in temperature dependence with the application of transverse magnetic field** With an applied field of ~ 80 G,the temperature dependence of the zero field splitting frequency is reduced by approximately 1%. This is increased to approximately 2% at ~120 G and continues to fall off quadratically.

The temperature dependence of one sub-ensemble of NV centers' zero field splitting frequency, $\beta \approx -74$ kHz/K, can be altered with the application of a strong magnetic field perpendicular to the NV ensemble axis as described in Eqn. 5.3 and plotted in Fig. 5-7.

$$\beta_{B_\perp} = \frac{dD_{gs}}{dT}\left(1 - \frac{3{\mu_0}^2 g^2}{2h^2 {D_{gs}}^2}{B_\perp}^2\right) \equiv \alpha\frac{dD_{gs}}{dT} \tag{5.3}$$

This temperature dependence falls off quadratically with increased applied transverse magnetic field. A 1% difference between $\beta_{B_\perp,1}$ and $\beta_{B_\perp,2}$ is expected with the application of an 80 G transverse magnetic field, while a 2% difference is expected with the application of a 120 G transverse magnetic field.

Transverse magnetic field can be applied uniformly with a combination of Helmholtz coils and a Halbach array of permanent magnets. Resolving a 10 Kelvin temperature shift will require resolution of the zero-field splitting to $\sim$ 750 Hz to adequately differentiate between the sub-ensemble that is most affected by $B_\perp$ and the ones that are minimally affected. Once a sample has been characterized, measuring the difference between the zero field splitting dependence over a temperature range will yield an absolute temperature measurement, immune to drift. However, since the strain profile of different diamond samples vary, each device will need to be initially calibrated.

5.5.3 Changing dD_{gs}/dT using strain

Anisotropically-applied strain can also be used to change the temperature dependence of one or more of the diamond NV sub-ensembles as detailed in [22]. While the lack of necessity for a large permanent magnetic field makes this is an attractive option, particularly for a compact system for *in situ* measurements, extremely high precision machining is required to produce a clamp that could apply sufficiently uniform strain across the sample. Alternately, carefully engineered diamond growth can produce highly strained regions of the sample that could be individually probed. Strain inhomogeneity would have the effect of broadening the resonance linewidths and decreasing the stability of the clock, so large areas of uniform strain are needed. Furthermore, due to diamond's high Young's modulus [123], large forces are required to produce this change, which can break or shatter the brittle diamond samples if not applied evenly. Previous work in using diamond for pressure sensing indicates sensitivity on the MPa/$\sqrt{\text{Hz}}$ scale [82, 124].

5.6 Conclusions and outlook

5.6.1 Feasibility of a competitive diamond-based frequency standard

To date, temperature instability has been the limiting factor for a practical diamond-based frequency standard competitive with chip-scale atomic clocks. Table 5.1 summarizes temperature stability corresponding to fractional frequency deviation, given a phenomenologically derived value of dD_{gs}/dT of 75 kHz/K and $D_{gs} \sim 2.87$ GHz.

Table 5.1: Required temperature stability

Temp. Stability	Fractional Frequency Deviation
1 K	$\sim 2.6 \times 10^{-5}$
1 mK	$\sim 2.6 \times 10^{-8}$
1 μK	$\sim 2.6 \times 10^{-11}$

For GPS, fractional frequency deviation lower than $\sim 10^{-12}$ is needed, and better than $\sim 10^{-14}$ is needed for spacecraft navigation. For comparison, the fractional frequency deviations of several types of atom-based clocks are given in Table 5.2.

Table 5.2: Comparison with atom-based frequency standards

Atom type	Fractional Frequency Deviation
Cs	$\sim 10^{-13}$
Rb	$\sim 10^{-15}$
H	$\sim 10^{-15}$
St	$\sim 10^{-17}$

Two methods have been explored to improve the stability of a diamond-based frequency standard earlier in the chapter. First, by engineering two ensembles of NV centers where each zero field splitting frequency has a different different dependence on temperature $\left(\frac{dD_{gs}}{dT}_n = \beta_n\right)$, we can obtain a fractional frequency deviation that is a factor of ξ worse than that of the ideal (perfect temperature stability) case, where $\xi = \sqrt{1 + 2\left(\frac{\beta_1}{\beta_2 - \beta_1}\right)^2}$. A 1% difference between β_1 and β_2 is expected with the application of an 80 G transverse magnetic field, while a 2% difference is expected with the application of a 120 G transverse magnetic field.

Table 5.3: Factor away from ideal fractional frequency deviation

$\frac{\beta_2-\beta_1}{\beta_1}$	ξ
0.01	141
0.02	70
0.03	47
0.10	14

This ideal fractional frequency deviation for an ensemble can be extrapolated from the non-temperature-limited single NV result of $\frac{\Delta\omega}{\omega} \sim 10^{-6}$. Improvement scales as $\sqrt{N}$ where N is the number of NVs. For a fractional frequency deviation of $\sim 10^{-12}$, given a 1%-2% difference in temperature dependence of the zero field splitting for two same-temperature ensembles, an ensemble of 10^{16} ensembles is required. Assuming that coherence is not affected, this corresponds to a density of 33 ppm in a 3 mm x 3 mm x 0.3 mm sample, which is not commercially available at this time. Currently available samples at densities approaching this have NVs with limited coherence times due to lattice damage and other impurities. However, at this high density, the higher absorption limits the path length in an LTDW geometry, making an even smaller, denser sample preferable. Ideal samples could be available as soon as within the next several years.

Considering the challenges in implementation of pulsed protocols on the LTDW platform due to RF uniformity, it's also worth considering the CW clock case. By studying the Zeeman-split ODMR spectra and monitoring the frequency of each of these resonances, two signals emerge, as shown in Section 3.2.2. The sum of the two frequencies gives a temperature dependent signal that, as a clock, is limited as indicated in Table 5.1. The difference of the two frequencies gives a temperature-independent signal. Given previous LTDW magnetometry results [90], temperature insensitivity corresponding to a fractional frequency deviation of $\sim 10^{-9}$ has been achieved. However this is not suitable for a frequency standard unless it can be magnetically shielded extremely well, as it is sensitive to nT level magnetic fields, unlike the clock protocol, which is insensitive to magnetic fields to first order.

In conclusion, there are three hurdles that must be overcome in order to implement a diamond-based frequency standard that is competitive with compact atomic clocks: (i) uniformly applied RF, (ii) decoupling from ambient temperature fluctuations, and (iii) production of an adequately high NV density sample with long coherence times. Several methods for combatting the first two issues have been discussed, and with the rapid advances in diamond-growth processes seen over the past several years, it is possible that a competitive diamond-based frequency standard could be available in the next several years.

Chapter 6

Summary and outlook

This thesis motivated and presented the light-trapping diamond waveguide device and demonstrated its utility for addressing large ensembles of low-density NV centers. This simple device's excitation efficiency and good signal collection enables in excess of 5% conversion efficiency of pump photons into optically detected magnetic resonance (ODMR) fluorescence, a three orders of magnitude improvement over previous single-pass geometries. This dramatic enhancement of ODMR signal enables *separable* precision broadband measurements of magnetic field and temperature in the low-frequency range inaccessible by dynamical decoupling techniques. The increased sensitivity achievable through ensemble-based magnetic field sensing lends itself to many existing, mature applications, while single-NV magnetic field sensing remains limited to the lab setting. In particular, medicine, materials science, and geoscience are application spaces where ensemble-based sensing shows great potential.

The LTDW is then used to study of the effect of weak transverse magnetic fields on the NV system. An electron-nuclear spin flip anti-crossing is predicted and experimentally verified. The previously predicted double-electron spin flip anti-crossing under transverse magnetic fields is also measured. These anti-crossings show potential for a variety of sensing applications because of (i) increased signal contrast, (ii) insensitivity to axial magnetic fields near the anti-crossing points, (iii) potential for nuclear spin polarization schemes, and (iv) selective decoupling of the NV from its environment through the use of different orientations with varying transverse fields.

This sets the stage for a large-ensemble device that could be used for a realistic diamond-based clock, pending advances in diamond material growth and processing. The proposed clock protocol is demonstrated on a single NV and on a small ensemble of NVs, followed by a discussion of the remaining challenges towards implementation using the LTDW or other large-ensemble platform. The two main challenges can be summarized as difficulties in obtaining applied field uniformity and decoupling from the environment. Beyond the simple method of removing temperature effects by monitoring both halves of the split ODMR signal, two more advanced methods for combatting ambient temperature fluctuations are detailed. Finally, the feasibility of a competitive diamond-based frequency standard is considered.

One limit to the current light-trapping diamond waveguide setup is non-optimal fluorescence collection (around 20%). By collecting light from more sides of the diamond, and closer to the diamond, this number can be improved. An improvement in sensitivity of $\sqrt{N}$ for an N-fold increase in the number of photons collected (due to an improvement in number of NVs or in photon collection) is expected due to an improvement in the photon shot noise limit. Future iterations of the LTDW device might incorporate fiber optic bundles and light pipes that can be placed near the diamond to collect the signal. These will also serve to reduce electrical and magnetic noise by further removing the photodetector from the setup. In addition, strategically deposited mirrors could also increase the fluorescence collection and device sensitivity.

The LTDW device geometry enables sensing using large NV ensembles while the material development processes mature. The size of the device makes it particularly susceptible to inhomogeneities in the applied RF excitation, laser excitation, and magnetic bias field. The comparatively large volume limits the spatial resolution of the device as a sensor. An ideal large-NV-ensemble sensor platform would be based on a high density sample with excellent defect quality. Diamond growth using isotopically pure ^{12}C as well as improvements in growth speed and crystal quality could make such a sample a reality. For the diamond clock, a 33 ppm sample is needed based on the current size of sample. An ideal clock sample would be smaller with higher NV density to achieve the same number of defects, or, similar NV density with improved NV coherence times.

While the LTDW device represents an improvement in power efficiency, it is far from a low-power device. At present a $\sim$ 100 mW laser power is required to achieve a magnetic field sensitivity on the order of 1 nT. Looking to the future, with improved diamond growth, the implementation of dynamical decoupling and optimal control techniques, and improved RF and laser uniformity we can expect to improve the NV resonance linewidth by approximately four orders of magnitude. Measurement contrast could be improved by more than an order of magnitude with directional, isotropically pure diamond growth, nuclear spin polarization, decreased contribution from the NV^0 charge state and other lattice defects, and improved RF field delivery. By improving the photon collection scheme and increasing the NV density, the photon collection rate could be improved by more than two orders of magnitude. Referring to Equation 1.2, the implementation of these improvements could give an improvement of roughly six orders of magnitude with a similar input power, achieving sensitivities on the femtotesla scale. Decreasing the power limit to 1 mW, we could still expect a sensitivity on the order of 10 fT, resulting in a magnetometer rivaling atomic systems with vastly lower power requirements.

This estimate, however, only takes laser power into account. An optimized, broadband, spatially-uniform RF antenna could in theory also contribute only minimally to the power budget, as the important parameter is the magnitude of the magnetic field delivered to the diamond rather than the power. In order to have what could be considered a truly low-power device, the electronics would also need to move on chip. This includes the photodetector, as well as RF generation and signal amplification and processing, which could be handled by an FPGA board. These system improvements are well-within the range of currently available technology.

Diamond-based sensing has reached a point in the arc of its development where many are wondering whether it will be competitive commercially. In order for the multitude of lab-based experiments to gain a foothold in the market and compete with existing commercially-available sensors, diamond-based sensors need to hit sensitivity thresholds that match or exceed commercially available technologies, rather than focusing on new records compared with other diamond-based devices. There must be a focus on designing robust, reliable devices that lend themselves to mass manufacture, rather than one-off experiments.

NV centers in diamond are sensitive to many environmental parameters. This presents one of the strongest arguments against pursuing the NV over searching for other promising defect centers, as the ideal magnetometer is sensitive to magnetic fields and nothing else. However, this multi-factor sensitivity forms the basis for the possibility of a multi-purpose sensor that could be extremely compact and robust. Similar to the idea of using two sub-ensembles as co-located clocks to combat noise from thermal fluctuations presented in Chapter 5, each sub-ensemble could be used independently. Alternatively, three orientations could be used for vector magnetometry while a fourth records temperature data.

This environmental sensitivity is a major concern for the diamond electron-spin clock. A realistic implementation that is competitive with existing technologies will rely on precise, careful engineering and concerted effort toward developing a high quality, high density NV sample. If adequate density is not achieved, time will also need to be spent addressing inhomogeneities in laser, RF, and magnetic bias fields that result from the device's large volume. While it is unlikely that a hybrid diamond clock magnetometer will be in every airplane in five years, the pace of progress in diamond-based sensing over the past five years indicates that exciting advances are forthcoming.

Appendix A

Polymer Photonics

The following, tangentially related investigations were also completed over the course of my doctoral work.

Polymers have appealing optical, biochemical, and mechanical qualities, including broadband transparency, ease of functionalization, and biocompatibility. However, their low refractive indices have precluded wavelength-scale optical confinement and nanophotonic applications in polymers. Here, we propose a suspended polymer photonic crystal (SPPC) architecture that enables the implementation of nanophotonic structures typically limited to high-index materials. Filters and integrated networks, as well as trace gas, force, and displacement sensing are explored.

A.1 Nanophotonic Filters and Integrated Networks in Flexible 2D Polymer Photonic Crystals

This work appeared in the following publication:

> "Nanophotonic Filters and Integrated Networks in Flexible 2D Polymer Photonic Crystals," X. Gan, H. Clevenson, C.-C. Tsai, L. Li, and D. Englund. Scientific Reports. **3**, 2145 (2013).

A two-dimensional suspended polymer photonic crystal (SPPC) architecture is introduced, enabling the implementation of nanophotonic structures typically limited to high-index materials, such as semiconductors. Using the SPPC platform, nanophotonic band-edge filters, waveguides and nanocavities are demonstrated, featuring quality factors exceeding 2,300 and ultrasmall mode volumes below $1.7(\lambda/n)^3$ (Fig. A-1). The SPPC architecture allows straightforward integration of planar nanophotonic devices into networks, demonstrated here by the implementation of a waveguide-coupled cavity drop filter with sub-nanometer spectral resolution. The nanoscale optical confinement in polymer opens the door to new applications ranging from optical communications to organic opto-electronics, organic photovoltaics, and nanophotonic polymer sensors.

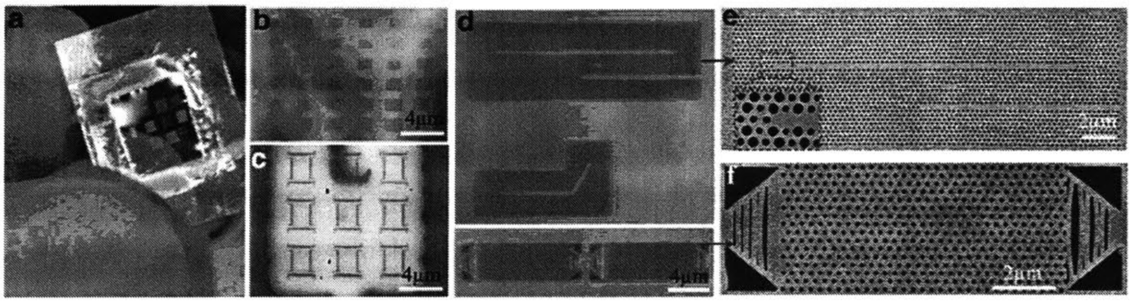

Figure A-1: (a) Photograph of the cm^2-sized PMMA film with SPPC devices mounted on a flexible polyester carrier. (b,c) Optical microscope images of the SPPC devices transferred onto fiber tissue and photoresist polymer (MICROPOSIT S1811) substrate after wet undercutting. (d) Optical microscope image of the tested SPPC devices, where from top to bottom show SPPC drop-filter, bent waveguide, and band-edge filters along ΓX and ΓJ directions. (e,f) Scanning electron microscope images of the SPPC drop-filter and band-edge filter.

A.2 High sensitivity gas sensor based on high-Q suspended polymer photonic crystal nanocavity

This work appeared in the following publication:

> "High sensitivity gas sensor based on high-Q suspended polymer photonic crystal nanocavity," H. Clevenson, P. Desjardins, X. Gan, and D. Englund. Appl. Phys, Lett. **104**, 241108 (2014).

A.2.1 Introduction

We present high-sensitivity, multi-use optical gas sensors based on a one-dimensional photonic crystal cavity. These devices are implemented in versatile, flexible polymer materials which swell when in contact with a target gas, causing a measurable cavity length change. This change causes a shift in the cavity resonance, allowing precision measurements of gas concentration. We demonstrate suspended polymer nanocavity sensors and the recovery of sensors after the removal of stimulant gas from the system. With a measured quality factor exceeding 10^4, we show measurements of gas concentration as low as 600 parts per million (ppm) and an experimental sensitivity of 10 ppm; furthermore, we predict detection levels in the parts-per-billion range for a variety of gases.

Sensing dilute gases is of interest in a variety of fields [127]. Much research has been directed at developing optical sensors for this task, as they enable a high signal-to-noise ratio, can operate in ambient conditions over a wide dynamic range, are immune to electromagnetic interference, and can be compact and lightweight [128, 129]. In particular, optical resonators can dramatically enhance the light-matter interaction time, which can lead to improved sensitivity to dilute gas concentrations [130, 131]. Previous work has employed optical fields confined in inorganic materials, interacting evanescently with gas-sensitive coatings, such as polymers [132, 133, 134, 135, 136], or directly with the gas [137] as a result of refractive index change. In this work, we use optical modes confined in polymer photonic crystals which swell in response to gas exposure, as illustrated in Figure 1. Since the mode is fully in the polymer, even minute length or refractive index changes of the cavity resulting from interaction with a gas cause strong and measurable changes in the cavity resonance frequency (see Fig. A-2).

A.2.2 Device design

The device is based on a one dimensional (1D) photonic crystal fabricated in poly(methyl methacrylate) (PMMA), which is an inexpensive, flexible, and resilient long-chain

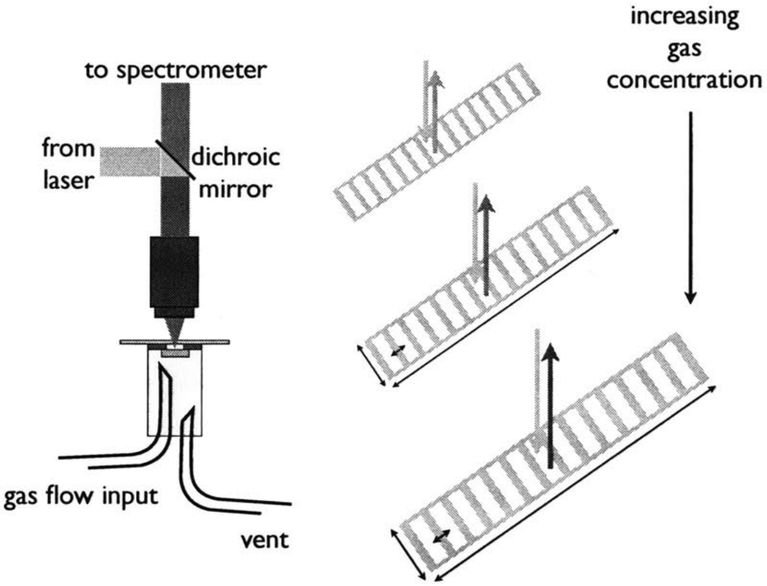

Figure A-2: The measurement setup and a conceptual schematic of the operation of this gas sensor. As the polymer photonic crystal cavity swells, its resonance peak shifts. Various surface treatments will enhance sensitivity to particular reagents.

polymer [125]. The swelling of the material is caused by the interaction of the PMMA ester pendant groups via hydrogen bonding with organic solvents such as alcohols. To interact with other gas molecules, PMMA can be functionalized appropriately [138]. Conveniently, PMMA is also an electron beam lithography (EBL) resist, making the device very straightforward to fabricate; it requires no mask transfers or extra wet or dry etching steps to process, unlike semiconductor materials that are traditionally used for nanophotonics. However, due to the low refractive index of PMMA (measured to be ~ 1.52), transverse confinement of light by total internal reflection (TIR) is difficult to achieve when clad in another material. The suspended one-dimensional photonic crystal resonators described here overcome this problem by surrounding the region of interest with air on all sides. This also allows the material to distend without obstruction when the analyte is present. Periodic rectangular holes in the structure form a distributed-Bragg reflector (DBR). Light is confined transversely through TIR and longitudinally via a photonic bandgap. Similar suspended architectures have been described for various materials including high-index semiconductors [139, 140, 141] and silicon dioxide [142]. Fig. A-3a shows the polymer photonic crystal lattice, which exhibits a bandgap when $0.4 \leq \omega \leq 0.45$, where ω is the normalized frequency, as obtained from finite difference time domain (FDTD) simulations [125]. A defect region creates a high-Q photonic cavity. The field intensities inside the structure are shown in Fig. A-3b. The first five holes next to the cavity are quadratically tapered to ameliorate the mode mismatch between the cavity mode and the Bragg mode and to increase the quality factor (Fig. A-3c). The cavity designs are optimized numerically using the open-source FDTD package MEEP [143], with a grid spacing of $a/20$ and a time step of a/c. We normally run over 1,000 time steps until the mode fully decays. The resonance frequencies and quality factors are obtained through a filter diagonalization method HARMINV [144] (error $\delta\omega/\omega < 10^{-3}$). For a lattice constant of a, the optimized cavity design has a width $w = 2.8a$, height $d = 1.4a$, air hole length $h_x = 0.52a$ and air hole width $h_y = 0.84w$. We obtain a cavity with a resonance at $\omega = a/\lambda = 0.447$, a quality factor ($Q$) of more than 107,000 and an ultra-small mode volume of $1.36(\lambda/n)^3$, where n is the refractive index of the polymer.

A.2.3 Theory

To determine the minimum concentration that can be sensed with this device, we begin by considering the relationship between the concentration of the gas and the change in the cavity resonance: $\frac{\Delta\lambda}{\lambda} \propto \frac{\Delta V}{V} \propto C$ [136], where $\Delta\lambda$ is the wavelength shift, λ is the cavity resonance wavelength, ΔV is the change in volume, V is the total volume of the structure, and C is the concentration of the analyte. Filling in proportionality constants, this can be written as $\frac{\Delta\lambda}{\lambda} = c_1\frac{\Delta V}{V} = c_1 c_0 C$, where c_1 quantifies the relationship between volume change and wavelength shift and c_0 gives the relationship between concentration and swelling. The minimum detectable resonance shift gives the minimum detectable concentration. A shift in the resonance wavelength can be measured either by internal luminescence of the polymer (using embedded emitters) or by a passive transmission or reflection measurement. Assuming shot-noise limited detection,

$$C_{min} = \frac{\xi}{Q\sqrt{\Gamma\tau}} \tag{A.1}$$

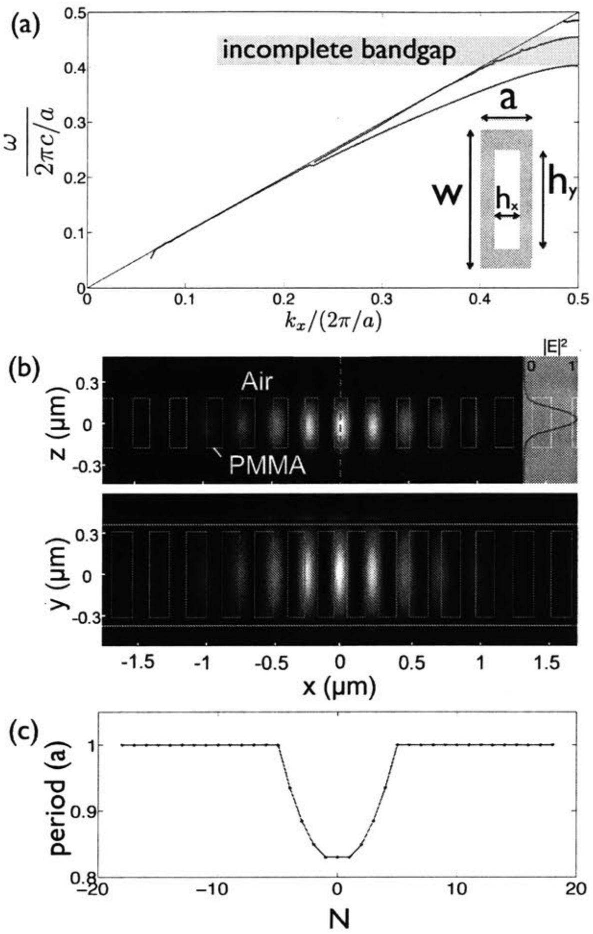

Figure A-3: (a) Band diagram showing four distinct modes of a one-dimensional infinite periodic waveguide comprised of a unit cell with a period of a. The width of the polymer beam is w and the air hole has dimension $h_x \times h_y$. (b) The electric field intensity ($|E|^2$) of the fundamental mode in the 1D nanobeam cavity in the $z = 0$ and $y = 0$ planes. A cross section of the Gaussian intensity profile is also shown. (c) Detail of the lattice constant taper used to create a high Q cavity.

where $\xi = 1/c_0c_1$, Q is the quality factor, Γ is the detected photon flux (counts/s), and τ is the integration time of the measurement.

From similar work with polymer coatings, we estimate $c_0 \approx 5 \times 10^2$ [136]. For volumetric expansion, $c_1 = \frac{1}{3}$; however we expect that at low concentrations, the surface of the structure will expand more than the interior, causing some amount of non-uniform swelling and local strain. We performed FDTD simulations and obtained $c_1 = 0.11$ for our device. Simulations of our device design result in Q values above 10^5. For this calculation we use $\Gamma \approx 1000$ counts/s on a single photon detector, which was typical in our measurements. This yields a theoretical concentration sensitivity:

$$S_{th} = \frac{\xi}{Q\sqrt{\Gamma}} = 6 \text{ ppb}/\sqrt{\text{Hz}}. \tag{A.2}$$

A.2.4 Device fabrication

To construct the devices, we spin-coat a 10 nm thick layer of water-soluble polyvinyl alcohol onto a silicon substrate, followed by 400 nm of PMMA. The patterns were defined using EBL, then immersed in water, allowing the PMMA film to float to the surface, where it could be transferred to any rough or patterned carrier. Figure A-4 shows two examples of structures onto which these polymer film devices can be transferred, including tissue consisting of minimally absorbent organic fibers with large air gaps (Figs. A-4a and A-4b). These were used to lift the films out of the water. Arrays of devices were spaced such that $\sim 80\%$ were suspended over air gaps when the film is randomly oriented on the tissue. It is also possible to suspend the film across a gap formed by two pieces of silicon secured to a glass slide (Fig. A-4c). This design was ideal for gas sensing experiments, as a lens-corrected objective could be used to image through the glass slide. Figure A-4d shows an SEM micrograph of a fabricated device, showing the smooth edges of the structure. Additionally, wire hoops, plastic transparency paper with cut holes, rough dense paper materials, and tapered fiber optic lines were successfully used to suspend these structures.

A.2.5 Experimental setup

We tested the devices on a confocal microscope setup with independent pump and collection paths. To facilitate the optical characterization of the cavity resonances, we doped the PMMA with Coumarin 6 dye, 5% by weight. The dye molecules were excited with a 405 nm laser and emit from 450 nm to 650 nm. Figure A-5a presents a cavity Q factor in excess of 10^4. Initial tests analyzed IPA vapor, though any gas or vapor that interacts with the polymer film can be used. The IPA vapor concentration in the system was controlled by a dilution gas flow setup. The sample was imaged

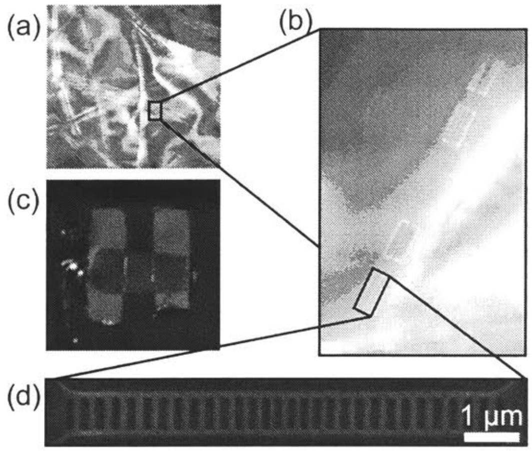

Figure A-4: (a) PMMA film on spun tissue paper (10× mag.) (b) Detail of structure in PMMA film on spun tissue paper (100× mag.) (c) Test structure using two pieces of silicon to form air gap. (d) SEM micrograph of fabricated structure.

through a glass cover-slip, using a lens-corrected objective. The volume containing the gas and sample was roughly 10 mL. A gas delivery line and a vent line allowed precise control over the gas pressure. Once mounted in the gas cell, the polymer cavity was exposed to 15 sccm dilute gas flow for 5 minutes, then exposed to air flow for 20 minutes for recovery.

A.2.6 Discussion

Four gas concentrations were tested, and the resulting shifts are detailed in Fig. A-5b. The three lowest concentrations seem to follow a linear trend, while the highest concentration appears to have saturated the device. When a gas infiltrates the polymer cavity, two effects occur: the refractive index changes and the material swells. PMMA can absorb up to 2wt% of its mass [145, 146]. The refractive index of the tested gas ($n_{\mathrm{IPA}} = 1.38$) at this full saturation concentration would cause a ~ 1 nm blue-shift in a cavity with a resonance around 630 nm, which is much smaller than the ~ 22 nm redshift caused by the swelling of the material under the same conditions, making the polymer deformation the dominant effect [136]. We show full recovery of the sensor after the IPA vapor has been removed from the system (Fig. A-5c). Additionally, we anticipate that low concentrations of vapors that corrode the polymer can also be

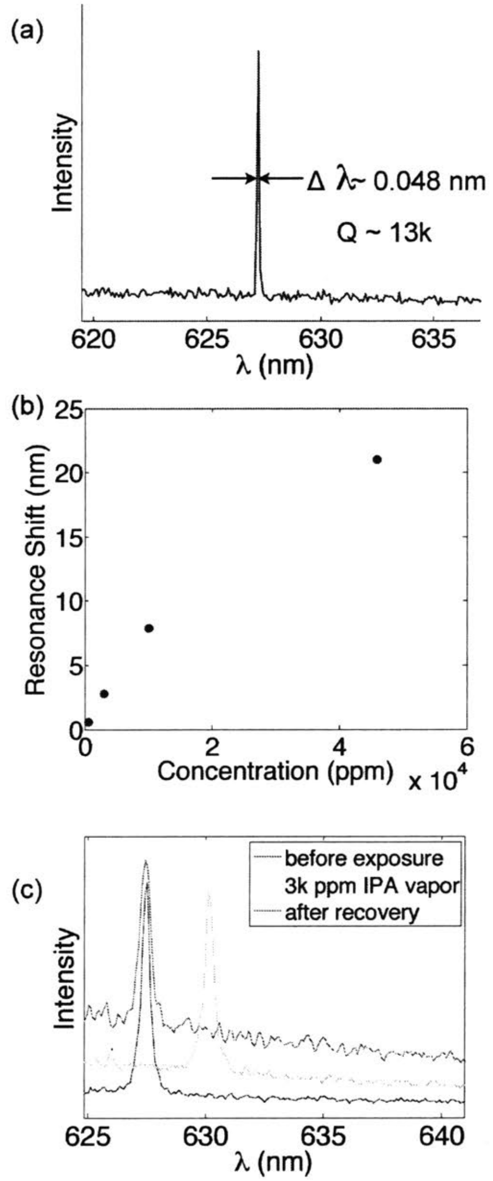

Figure A-5: (a) Photoluminescence spectrum of a high-Q cavity. The resonance is at 627 nm and the quality factor is around 13, 000. (b) Resonance shifts plotted against gas concentration. The point with the highest concentration seems to show saturation behavior. (c) After the stimulant gas is removed from the system, the resonance returns to it's original position. The baseline signal decreases as time progresses as a result of bleaching of the dye in the PMMA.

detected, such as ozone and acetone vapor.

When the cavity is exposed to the minimum concentration tested (600 ppm), we measure a 0.6 nm wavelength redshift from 631.9 nm to 632.5 nm. The quality factor of this cavity was 2×10^3. The Q may be improved by using a higher resolution e-beam lithography tool with image-stitching capabilities. These values correspond to an experimental sensitivity of $S_{exp} = 10$ ppm/$\sqrt{\text{Hz}}$. From Eq. A.2, we expect a cavity with this Q factor to have a sensitivity of $S_{th} = 287$ ppb/$\sqrt{\text{Hz}}$, which is over an order of magnitude better than the performance we observed. There are several possible explanations for this discrepancy: first, our value for c_1 is based on simulation and assumes an even expansion of the surface of the structure. In reality, while every effort was made to ensure a smooth, even gas flow, some parts of the structure may have been oriented such that the top surface may have swelled more than the bottom. Second, the swelling coefficient c_0 cannot be experimentally measured using our setup and our polymer cavity might have a slightly different swelling coefficient than in [136]. Given the precision of the gas delivery and vent hoses, extremely low gas concentrations are not possible to verify using our current testbed. Finally, we expect that sources of noise exist in our experimental setup beyond shot-noise, such as vibrational and thermal effects. We also see a decrease in our cavity Q when the gas is introduced into the system. This can be accounted for by the increased swelling of the surface of the material; surface swelling changes the relationship between a and h_x and between w and h_y, as detailed in the inset of Figure A-3a.

In conclusion, compact, low-cost, high-Q 1D polymer photonic crystals with high sensitivity provide the opportunity for state-of-the-art gas sensing on almost any rough or patterned surface imaginable. We have demonstrated the implementation of these sensors and their recovery after stimulant gases are removed from the system. We expect that experimental sensitivity will increase with improved fabrication processes and with improved readout techniques, such as doping with an agent that will provide stronger fluorescence or with the implementation of cavity transmission measurements. This platform could be useful in a variety of industrial, environmental, and even biological settings. These devices have the potential to be applied to a variety of sensing applications, especially with surface functionalization for specific stimulants.

A.3 High-Q suspended polymer nanocavities for precision force and displacement sensing

This work appeared in the following publication:

> "A Polymer Photonic Crystal Nanocavity for Precision Strain Sensing," X. Gan, H. Clevenson, and D. Englund. *Under review.*

Flexible one-dimensional polymer photonic crystal nanocavities (Fig.A-6) with quality factors exceeding 10^4 are demonstrated for precision sensing of strain, displacement, and force at experimentally measured values of 10^{-4}, 0.94 nm, and 55 nN, respectively. This flexible-nanocavity microsensor shows high linearity and repeatability. The microsensor concept is also compatible with liquid environments. The ease of fabrication, flexibility, and biocompatibility of the polymer microsensor promise applications in strain and force measurements at the micro-scale in the physical, material, and life sciences.

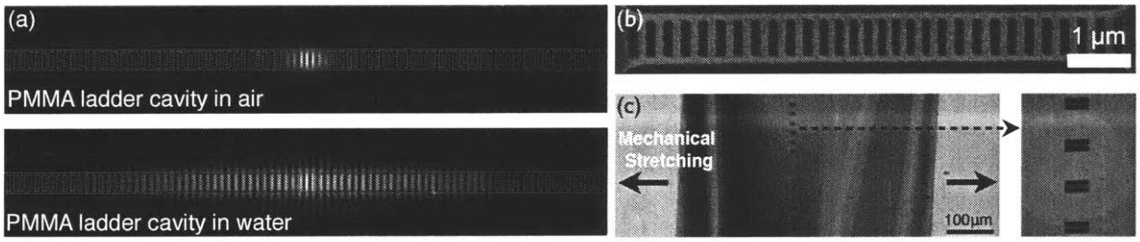

Figure A-6: (a) Energy field distributions of the simulated resonant modes of the designed SPPC cavity in air (top) and water (bottom) environments, respectively. (b) Scanning electron microscope image of the suspended ladder nanocavity. (c) Optical microscope image of the nanocavity-based displacement sensor. The PMMA film with ladder cavities is suspended on a mechanical carrier, which is connected to a piezo-actuated stage to stretch the flexible cavities.

Bibliography

[1] Matushita, S. & Campbell, W. H. (eds.) Physics of Geomagnetic Phenomena (Academic Press, 1967).

[2] Fagaly, R. L. Superconducting quantum interference device instruments and applications. Review of Scientific Instruments **77** (2006).

[3] Edelstein, A. Advances in magnetometry. J. Phys. Condens. Matter **19**, 165217 (2007).

[4] Balasubramanian, G. et al. Ultralong spin coherence time in isotopically engineered diamond. Nat. Mater. **8**, 383–387 (2009).

[5] Stanwix, P. L. et al. Coherence of nitrogen-vacancy electronic spin ensembles in diamond. Physical Review B **82**, 201201 (2010).

[6] Bar-Gill, N., Pham, L. M., Jarmola, A., Budker, D. & Walsworth, R. L. Solid-state electronic spin coherence time approaching one second. Nat Commun **4** (2013).

[7] Budker, D. & Romalis, M. Optical magnetometry. Nature Physics **3**, 227–234 (2007).

[8] Taylor, J. M. et al. High-sensitivity diamond magnetometer with nanoscale resolution. Nature Physics **4**, 810–816 (2008).

[9] Maze, J. R. et al. Nanoscale magnetic sensing with an individual electronic spin in diamond. Nature **455**, 644–7 (2008).

[10] Balasubramanian, G. et al. Nanoscale imaging magnetometry with diamond spins under ambient conditions. Nature **455**, 648–651 (2008).

[11] Fang, K. et al. High-sensitivity magnetometry based on quantum beats in diamond nitrogen-vacancy centers. Phys. Rev. Lett. **110**, 130802 (2013).

[12] Rondin, L. et al. Magnetometry with nitrogen-vacancy defects in diamond. Reports on Progress in Physics **77**, 056503 (2014).

[13] Wolf, T. et al. A subpicotesla diamond magnetometer. Phys. Rev. X **5** (2015).

[14] Le Sage, D. et al. Efficient photon detection from color centers in a diamond optical waveguide. Phys. Rev. B **85**, 121202 (2012).

[15] Jensen, K. et al. Cavity-enhanced room-temperature magnetometry using absorption by nitrogen-vacancy centers in diamond. PRL **112**, 160802 (2014).

[16] Dolde, F. et al. Electric-field sensing using single diamond spins. Nat Phys **7**, 459–463 (2011).

[17] Teissier, J., Barfuss, A., Appel, P., Neu, E. & Maletinsky, P. Strain coupling of a nitrogen-vacancy center spin to a diamond mechanical oscillator. Phys. Rev. Lett. **113**, 020503 (2014).

[18] Kucsko, G. et al. Nanometre-scale thermometry in a living cell. Nature **500**, 54–58 (2013).

[19] Toyli, D. M., Charles, F., Christle, D. J., Dobrovitski, V. V. & Awschalom, D. D. Fluorescence thermometry enhanced by the quantum coherence of single spins in diamond. Proceedings of the National Academy of Sciences **110**, 8417–8421 (2013).

[20] Neumann, P. et al. High-precision nanoscale temperature sensing using single defects in diamond. Nano Letters **13**, 2738–2742 (2013).

[21] Pham, L. M. et al. Magnetic field imaging with nitrogen-vacancy ensembles. New Journal of Physics **13**, 045021 (2011).

[22] Hodges, J. S. et al. Timekeeping with electron spin states in diamond. Phys. Rev. A **87**, 032118 (2013).

[23] Esnault, F.-X. et al. Cold-atom double-Λ coherent population trapping clock. Phys. Rev. A **88**, 042120 (2013).

[24] Manson, N. B., Harrison, J. P. & Sellars, M. J. Nitrogen-vacancy center in diamond: Model of the electronic structure and associated dynamics. Phys. Rev. B **74**, 104303 (2006).

[25] Loubser, J. H. N. & van Wyk, J. A. Electron spin resonance in the study of diamond. Reports on Progress in Physics **41**, 1201 (1978).

[26] Shigley, J. E. & Breeding, C. M. Optical defects in diamond: A quick reference chart. Gems & Gemology **49** (2013).

[27] Doherty, M. W. et al. Theory of the ground-state spin of the nv$^-$ center in diamond. Phys. Rev. B **85**, 205203 (2012).

[28] Bernieri, A., Ferrigno, L., Laracca, M. & Tamburrino, A. Improving gmr magnetometer sensor uncertainty by implementing an automatic procedure for calibration and adjustment. In

Instrumentation and Measurement Technology Conference Proceedings, 1–6 (IEEE, 2007).

[29] Nishio, Y., Tohyama, F. & Onishi, N. The sensor temperature characteristics of a fluxgate magnetometer by a wide-range temperature test for a mercury exploration satellite. Measurement Science and Technology **18**, 2721 (2007).

[30] Wolf, T. et al. Subpicotesla diamond magnetometry. Phys. Rev. X **5**, 041001 (2015).

[31] Barry, J. F. et al. Optical magnetic detection of single-neuron action potentials using quantum defects in diamond. Proceedings of the National Academy of Sciences **113**, 14133–14138 (2016).

[32] Niethammer, M. et al. Vector magnetometry using silicon vacancies in $4h$-sic under ambient conditions. Phys. Rev. Applied **6**, 034001 (2016).

[33] Calusine, G., Politi, A. & Awschalom, D. D. Cavity-enhanced measurements of defect spins in silicon carbide. Phys. Rev. Applied **6**, 014019 (2016).

[34] Simin, D. et al. All-optical dc nanotesla magnetometry using silicon vacancy fine structure in isotopically purified silicon carbide. Phys. Rev. X **6**, 031014 (2016).

[35] Acosta, V. M. et al. Temperature dependence of the nitrogen-vacancy magnetic resonance in diamond. Phys. Rev. Lett. **104**, 070801 (2010).

[36] Chen, X.-D. et al. Temperature dependent energy level shifts of nitrogen-vacancy centers in diamond. Applied Physics Letters **99**, 161903 (2011).

[37] Doherty, M. W. et al. Temperature shifts of the resonances of the nv$^-$ center in diamond. Phys. Rev. B **90**, 041201 (2014).

[38] Dréau, A. et al. Avoiding power broadening in optically detected magnetic resonance of single nv defects for enhanced dc magnetic field sensitivity. Phys. Rev. B **84**, 195204 (2011).

[39] Schröder, T., Gädeke, F., Banholzer, M. J. & Benson, O. Ultrabright and efficient single-photon generation based on nitrogen-vacancy centres in nanodiamonds on a solid immersion lens. New Journal of Physics **13**, 055017 (2011).

[40] Dmitriev, A. K. & Vershovskii, A. K. Concept of a microscale vector magnetic field sensor based on nitrogen-vacancy centers in diamond. J. Opt. Soc. Am. B **33**, B1–B4 (2016).

[41] Ajoy, A. & Cappellaro, P. Stable three-axis nuclear-spin gyroscope in diamond. Phys. Rev. A **86**, 062104 (2012).

[42] Lin, C.-K., Wang, Y.-H., Chang, H.-C., Hayashi, M. & Lin, S. H. One- and two-photon absorption properties of diamond nitrogen-vacancy defect centers: A theoretical study. The Journal of Chemical Physics **129** (2008).

[43] Wang, Z.-H. & Takahashi, S. Spin decoherence and electron spin bath noise of a nitrogen-vacancy center in diamond. Phys. Rev. B **87**, 115122 (2013).

[44] Bar-Gill, N. et al. Suppression of spin-bath dynamics for improved coherence of multi-spin-qubit systems. Nat Commun **3** (2012).

[45] Saleh, B. & Teich, M. Fundamentals of Photonics (Wiley-Interscience, Hoboken, N.J, 2007).

[46] Wrachtrup, J. & Jelezko, F. Processing quantum information in diamond. Journal of Physics: Condensed Matter **18**, S807 (2006).

[47] Narimanov, E., Fan, J. & Gmachl, C. Compact quasi-chaotic optical cavity. In Quantum Electronics and Laser Science Conference, QWA7 (Optical Society of America, 2005).

[48] Ilchenko, V. S. et al. Whispering gallery mode diamond resonator. Opt. Lett. **38**, 4320–4323 (2013).

[49] Fang, K. et al. High-sensitivity magnetometry based on quantum beats in diamond nitrogen-vacancy centers. Phys. Rev. Lett. **110**, 130802 (2013).

[50] Poem, E., Kaczmarek, K., Weinzetl, C., Nunn, J. & Walmsley, I. Proposed ultrafast optical control and broadband optical quantum memory with neutral nitrogen-vacancy centers in diamond. arXiv preprint arXiv:1408.7045 (2014).

[51] Shin, C. S. et al. Room-temperature operation of a radiofrequency diamond magnetometer near the shot-noise limit. Journal of Applied Physics **112** (2012).

[52] Clevenson, H. et al. Broadband magnetometry and temperature sensing with a light-trapping diamond waveguide. Nature Physics **11**, 393–397 (2015).

[53] Barry, J. et al. Optical magnetic detection of single-neuron action potentials using quantum defects in diamond. arXiv preprint arXiv:1602.01056 (2016).

[54] Alexandrov, E. B. Optically pumped atomic magnetometers after three decades. Optical Engineering **31**, 711 (1992).

[55] Cui, Y., An, R. & Ariyur, K. B. Cellphone geolocation via magnetic mapping. Automatica **51**, 70 – 79 (2015).

[56] Shockley, J. A. & Raquet, J. F. Navigation of ground vehicles using magnetic field variations. Navigation **61**, 237–252 (2014).

[57] Foote, R. S. Relationship of near-surface magnetic anomalies to oil-and gas-producing areas (1996).

[58] Kvamme, K. L. Magnetometry: Nature's gift to archaeology. Remote sensing in archaeology: An explicitly North American perspective 205–233 (2006).

[59] Espy, M. et al. Ultra-low-field mri for the detection of liquid explosives. Superconductor Science and Technology **23**, 034023 (2010).

[60] Sudac, D., Matika, D. & Valkovic, V. Detection of explosives in objects on the bottom of the sea. In Application of Accelerators in Research and Industry, vol. 1099, 574–577 (AIP Publishing, 2009).

[61] McFee, J. E., Ellingson, R. O. & Das, Y. A total-field magnetometer system for location and identification of compact ferrous objects. IEEE transactions on instrumentation and measurement **43**, 613–619 (1994).

[62] Sharma, S., Hovde, C. & Beck, D. H. Diamond-based field sensor for nEDM experiment. vol. 9755, 97552U–97552U–10 (2016).

[63] Merceret, F. J., Ward, J. G., Mach, D. M., Bateman, M. G. & Dye, J. E. On the magnitude of the electric field near thunderstorm-associated clouds. Journal of Applied Meteorology and Climatology **47**, 240–248 (2008).

[64] Simoes, F., Pfaff, R., Berthelier, J.-J. & Klenzing, J. A Review of Low Frequency Electromagnetic Wave Phenomena Related to Tropospheric-Ionospheric Coupling Mechanisms. Space Science Reviews **168**, 551–593 (2012).

[65] Mezuman, K., Price, C. & Galanti, E. On the spatial and temporal distribution of global thunderstorm cells. Environmental Research Letters **9**, 124023 (2014).

[66] Fort, A. et al. Design, Modeling, and Test of a System for Atmospheric Electric Field Measurement. Ieee Transactions on Instrumentation and Measurement **60**, 2778–2785 (2011).

[67] Harrington, R. F. Effect of antenna size on gain, bandwidth, and efficiency. J. Res. Nat. Bur. Stand **64**, 1–12 (1960).

[68] Chu, L. J. Physical Limitations of Omni-Directional Antennas. Journal of Applied Physics **19**, 1163–1175 (1948).

[69] Chubb, J. Limitations on the performance of 'field mill' fieldmeters with alternating electric fields. Journal of Electrostatics **78**, 1–3 (2015).

[70] Barr, R., Jones, D. L. & Rodger, C. J. ELF and VLF radio waves. Journal of Atmospheric and Solar-Terrestrial Physics **62**, 1689–1718 (NOV-DEC 2000).

[71] Savchenkov, A. A. et al. Photonic E-field sensor. AIP Advances **4**, 122901 (2014).

[72] Toney, J. E. *Lithium Niobate Photonics* (Artech House, 2015).

[73] Vohra, S. T., Bucholtz, F. & Kersey, A. D. Fiber-optic dc and low-frequency electric-field sensor. *Optics Letters* **16**, 1445 (1991).

[74] Bruzewicz, C. D., Sage, J. M. & Chiaverini, J. Measurement of ion motional heating rates over a range of trap frequencies and temperatures. *Physical Review A* **91**, 041402 (2015).

[75] Osterwalder, A. & Merkt, F. Using High Rydberg States as Electric Field Sensors. *Physical Review Letters* **82**, 1831–1834 (1999).

[76] Sedlacek, J. A. *et al.* Microwave electrometry with Rydberg atoms in a vapour cell using bright atomic resonances. *Nature Physics* **8**, 819–824 (2012).

[77] Dolde, F. *et al.* Nanoscale detection of a single fundamental charge in ambient conditions using the NV^- center in diamond. *Phys. Rev. Lett.* **112**, 097603 (2014).

[78] Doherty, M. W. *et al.* Measuring the defect structure orientation of a single nv âĹŠ centre in diamond. *New Journal of Physics* **16**, 063067 (2014).

[79] Oort, E. V. & Glasbeek, M. Electric-field-induced modulation of spin echoes of n-v centers in diamond. *Chemical Physics Letters* **168**, 529 – 532 (1990).

[80] Rondin, L. *et al.* Magnetometry with nitrogen-vacancy defects in diamond. *Reports on Progress in Physics* **77**, 056503 (2014).

[81] Ovartchaiyapong, P., Lee, K. W., Myers, B. A. & Jayich, A. C. B. Dynamic strain-mediated coupling of a single diamond spin to a mechanical resonator. *Nat Commun* **5** (2014).

[82] Doherty, M. W. *et al.* Electronic properties and metrology applications of the diamond nv^- center under pressure. *Phys. Rev. Lett.* **112**, 047601 (2014).

[83] Epstein, R. J., Mendoza, F. M., Kato, Y. K. & Awschalom, D. D. Anisotropic interactions of a single spin and dark-spin spectroscopy in diamond. *Nat Phys* **1**, 94–98 (2005).

[84] Neumann, P. *et al.* Excited-state spectroscopy of single nv defects in diamond using optically detected magnetic resonance. *New Journal of Physics* **11**, 013017 (2009).

[85] Fuchs, G. D. *et al.* Excited-state spectroscopy using single spin manipulation in diamond. *Phys. Rev. Lett.* **101**, 117601 (2008).

[86] Fischer, R., Jarmola, A., Kehayias, P. & Budker, D. Optical polarization of nuclear ensembles in diamond. *Phys. Rev. B* **87**, 125207 (2013).

[87] Jacques, V. et al. Dynamic polarization of single nuclear spins by optical pumping of nitrogen-vacancy color centers in diamond at room temperature. Phys. Rev. Lett. **102**, 057403 (2009).

[88] Steiner, M., Neumann, P., Beck, J., Jelezko, F. & Wrachtrup, J. Universal enhancement of the optical readout fidelity of single electron spins at nitrogen-vacancy centers in diamond. Phys. Rev. B **81**, 035205 (2010).

[89] Smeltzer, B., McIntyre, J. & Childress, L. Robust control of individual nuclear spins in diamond. Phys. Rev. A **80**, 050302 (2009).

[90] Clevenson, H. et al. Broadband magnetometry and temperature sensing with a light-trapping diamond waveguide. Nat Phys **11**, 393–397 (2015).

[91] Fischer, R. et al. Bulk nuclear polarization enhanced at room temperature by optical pumping. Phys. Rev. Lett. **111**, 057601 (2013).

[92] Wang, H.-J. et al. Sensitive magnetic control of ensemble nuclear spin hyperpolarization in diamond. Nat Commun **4** (2013).

[93] Scheuer, J. et al. Optically induced dynamic nuclear spin polarisation in diamond. New Journal of Physics **18**, 013040 (2016).

[94] Fuchs, G. D., Burkard, G., Klimov, P. V. & Awschalom, D. D. A quantum memory intrinsic to single nitrogen-vacancy centres in diamond. Nat Phys **7**, 789–793 (2011).

[95] Nichol, J. M. et al. Quenching of dynamic nuclear polarization by spin-orbit coupling in gaas quantum dots. Nat Commun **6** (2015).

[96] Ribeiro, H. & Burkard, G. Nuclear state preparation via landau-zener-stückelberg transitions in double quantum dots. Phys. Rev. Lett. **102**, 216802 (2009).

[97] Nalbach, P., Knörzer, J. & Ludwig, S. Nonequilibrium landau-zener-stueckelberg spectroscopy in a double quantum dot. Phys. Rev. B **87**, 165425 (2013).

[98] Pagliero, D., Laraoui, A., Henshaw, J. D. & Meriles, C. A. Recursive polarization of nuclear spins in diamond at arbitrary magnetic fields. Applied Physics Letters **105** (2014).

[99] Landau, L. Phys. Z. Sowjetunion **2**, 46 (1932).

[100] Zener, C. Non-adiabatic crossing of energy levels. Proc. R. Soc. A **137**, 696–702 (1932).

[101] Stuckelberg, E. Helv. Phys. Acta **5**, 36 (1932).

[102] Neumann, P. et al. Single-shot readout of a single nuclear spin. Science **329**, 542–544 (2010).

[103] Ledbetter, M. P., Jensen, K., Fischer, R., Jarmola, A. & Budker, D. Gyroscopes based on nitrogen-vacancy centers in diamond. Phys. Rev. A **86**, 052116 (2012).

[104] Maurer, P. C. et al. Room-temperature quantum bit memory exceeding one second. Science **336**, 1283–1286 (2012).

[105] Shim, J. H., Niemeyer, I., Zhang, J. & Suter, D. Room-temperature high-speed nuclear-spin quantum memory in diamond. Phys. Rev. A **87**, 012301 (2013).

[106] Straessle, R. et al. Low-temperature indium-bonded alkali vapor cell for chip-scale atomic clocks. Journal of Applied Physics **113**, 064501–064501–8 (2013).

[107] Nshii, C. C. et al. A surface-patterned chip as a strong source of ultracold atoms for quantum technologies. Nat Nano (2013).

[108] Miah, M. J. et al. Fabrication and characterization of low-threshold polarization-stable vcsels for cs-based miniaturized atomic clocks. IEEE JOURNAL OF SELECTED TOPICS IN QUANTUM ELECTRONICS **19**, 1701410 (2013).

[109] Lutwak, R. The sa. 45s chip-scale atomic clock–early production statistics. Precise Time and Time Interval (2011).

[110] Knappe, S. et al. Microfabricated atomic clocks and magnetometers. In Optical MEMS and Their Applications Conference, 193 –194 (2005).

[111] Shah, V., Knappe, S., Schwindt, P. D. D. & Kitching, J. Subpicotesla atomic magnetometry with a microfabricated vapour cell. Nature Photonics **1**, 649–652 (2007).

[112] Lee, D. Analysis of jitter in phase-locked loops. IEEE Transactions on Circuits and Systems II **49**, 704–711 (2002).

[113] Lewandowski, W., Azoubib, J. & Klepczynski, W. Gps: primary tool for time transfer. Proceedings of the IEEE **87**, 163 –172 (1999).

[114] Hodges, J. S. et al. Timekeeping with electron spin states in diamond. Phys. Rev. A **87**, 032118 (2013).

[115] Bayat, K., Choy, J., Farrokh Baroughi, M., Meesala, S. & Loncar, M. Efficient, uniform, and large area microwave magnetic coupling to nv centers in diamond using double split-ring resonators. Nano letters **14**, 1208–1213 (2014).

[116] Zhang, N. et al. Microwave magnetic field coupling with nitrogen-vacancy center ensembles in diamond with high homogeneity. Applied Magnetic Resonance **47**, 589–599 (2016).

[117] Sasaki, K. et al. Broadband, large-area microwave antenna for optically detected magnetic resonance of nitrogen-vacancy centers in diamond. Review of Scientific Instruments **87**, 053904 (2016).

[118] MacQuarrie, E. R. et al. Coherent control of a nitrogen-vacancy center spin ensemble with a diamond mechanical resonator. Optica **2**, 233–238 (2015).

[119] Farfurnik, D. et al. Optimizing a dynamical decoupling protocol for solid-state electronic spin ensembles in diamond. Physical Review B **92**, 060301 (2015).

[120] Nöbauer, T. et al. Smooth optimal quantum control for robust solid-state spin magnetometry. Physical review letters **115**, 190801 (2015).

[121] Schulte-Herbrüggen, T., Spörl, A., Khaneja, N. & Glaser, S. Optimal control for generating quantum gates in open dissipative systems. Journal of Physics B: Atomic, Molecular and Optical Physics **44**, 154013 (2011).

[122] Dolde, F. et al. High-fidelity spin entanglement using optimal control. Nature communications **5** (2014).

[123] Spear, K. E. & Dismukes, J. P. Synthetic Diamond, vol. 25 (John Wiley & Sons, 1994).

[124] Cai, J., Jelezko, F. & Plenio, M. B. Hybrid sensors based on colour centres in diamond and piezoactive layers. Nature communications **5** (2014).

[125] Gan, X., Clevenson, H., Tsai, C.-C., Li, L. & Englund, D. Nanophotonic filters and integrated networks in flexible 2d polymer photonic crystals. Sci. Rep. **3** (2013).

[126] Clevenson, H., Desjardins, P., Gan, X. & Englund, D. High sensitivity gas sensor based on high-q suspended polymer photonic crystal nanocavity. Applied Physics Letters **104** (2014).

[127] Liu, X. et al. A survey on gas sensing technology. Sensors **12**, 9635–9665 (2012).

[128] Some, S. et al. Highly sensitive and selective gas sensor using hydrophilic and hydrophobic graphenes. Sci. Rep. **3** (2013).

[129] Eguchi, K. Optical Gas Sensors, 307–328 (Springer Netherlands, 1992).

[130] Hodgkinson, J. & Tatam, R. P. Optical gas sensing: a review. Measurement Science and Technology **24**, 012004 (2013).

[131] Bae, M.-K., Lim, J. A., Kim, S. & Song, Y.-W. Ultra-highly sensitive optical gas sensors based on chemomechanical polymer-incorporated fiber interferometer. Optics express **21**, 2018–2023 (2013).

[132] Mehrabani, S., Kwong, P., Gupta, M. & Armani, A. M. Hybrid microcavity humidity sensor. Applied Physics Letters **102**, 241101 (2013).

[133] Rosenberger, A. T. & Rezac, J. P. Whispering-gallery-mode evanescent-wave microsensor for trace-gas detection. Proc. SPIE **4265**, 102–112 (2001).

[134] Zee, F. & Judy, J. W. Micromachined polymer-based chemical gas sensor array. Sensors and Actuators B: Chemical **72**, 120–128 (2001).

[135] El-Sherif, M., Bansal, L. & Yuan, J. Fiber Optic Sensors For Detection of Toxic and Biological Threats. Sensors **7**, 3100–3118 (2007).

[136] Smith, C. L. C. et al. Enhanced transduction of photonic crystal dye lasers for gas sensing via swelling polymer film. Optics letters **36**, 1392–4 (2011).

[137] Lončar, M., Scherer, A. & Qiu, Y. Photonic crystal laser sources for chemical detection. Applied Physics Letters **82**, 4648 (2003).

[138] Sarantopoulou, E. et al. Surface nano/micro functionalization of {PMMA} thin films by 157 nm irradiation for sensing applications. Applied Surface Science **254**, 1710 - 1719 (2008).

[139] Notomi, M., Kuramochi, E. & Taniyama, H. Ultrahigh-Q nanocavity with 1D photonic gap. Optics express **16**, 11095–102 (2008).

[140] Gong, Y. et al. Nanobeam photonic crystal cavity quantum dot laser. Opt. Express **18**, 8781–8789 (2010).

[141] Quan, Q. & Loncar, M. Deterministic design of wavelength scale, ultra-high q photonic crystal nanobeam cavities. Opt. Express **19**, 18529–18542 (2011).

[142] Gong, Y. & Vučković, J. Photonic crystal cavities in silicon dioxide. Applied Physics Letters **96**, 031107 (2010).

[143] Oskooi, A. F. et al. Meep: A flexible free-software package for electromagnetic simulations by the fdtd method. Computer Physics Communications **181**, 687–702 (2010).

[144] Mandelshtam, V. A. & Taylor, H. S. Harmonic inversion of time signals and its applications. The Journal of chemical physics **107**, 6756–6769 (1997).

[145] Bueche, F. Diffusion of water in polymethyl methacrylate. Journal of Polymer Science **14**, 414–416 (1954).

[146] Smith, L. & Schmitz, V. The effect of water on the glass transition temperature of poly(methyl methacrylate). Polymer **29**, 1871 - 1878 (1988).